Transfermatrix-DMRG
for dynamics of stochastic models and thermodynamics of fermionic models

vorgelegt von
ANDREAS KEMPER
aus Neuss

Köln 2003

Contents

Preface

Strongly correlated systems with a huge number of degrees of freedom appear in many physical research fields, that reach from quantum models, statistical systems to non-equilibrium phenomena. Typically, microscopic strong interactions can lead to highly non-trivial collective macroscopic behavior, which provides a fascinating field for theoretical studies.

The present thesis focus on two different types of *one-dimensional* strongly correlated systems that seemingly belong to opposed research fields. In the first part we study the thermodynamics of a fermionic model and thereby face typical questions of equilibrium physics. The second part of the thesis turns to investigations of stochastic systems, a quite modern research field of non-equilibrium physics.

On a theoretical level, strongly correlated systems are – even though they concern such different physics mentioned above – tractable by similar techniques. Particularly interesting is the case of one dimension. On the one hand, the restricted topology alludes to a number of powerful analytical and highly precise numerical methods. On the other hand, fluctuations and collective effects are generically strong. Therefore principle correlation effects are often studied in one dimension first, even if the original physical model necessitates a richer topology.

Since a couple of years, the rapid evolution of computer technology affected great progress in the development of complex numerical algorithms. One of the most important ones is the density-matrix renormalization-group (DMRG), which was developed by WHITE in 1992 [1, 2] to study the low-energy physics of one-dimensional quantum systems. The DMRG is based on a surprisingly simple, but effective concept. The aim of the algorithm is to successively enlarge a Hamilton operator and store the respective matrix by a computer. The problem of an exponentially increasing matrix dimension is countered by a renormalization procedure, that integrates out physically "unimportant" degrees of freedom.

The discovery of the DMRG also initiated wide activity on various considerable variants of the method in other physical fields. For the numerical studies of the present thesis we use the so-called transfer-matrix DMRG (TMRG), that was originally introduced by NISHINO in 1996 [3] to study *two-dimensional* classical statistical models.

In our case such a "second" additional dimension occurs in natural manner by the (reciprocal) temperature. It was indeed shown by SUZUKI [4], that the thermodynamics of a one-dimensional quantum system with short-range interactions can be mapped onto a two-dimensional classical statistical model. As he used a mathematical decomposition formula tracing back to TROTTER

[5], the mapping is known as Trotter-Suzuki decomposition. After all, XIANG
et. al [6, 7] noticed, that the TMRG algorithm thereby is suited to analyze also
thermodynamic properties.

We will use the TMRG to study the thermodynamics of strongly correlated
interacting fermion systems. Since the discovery of high-temperature super-
conductivity by BEDNORZ and MÜLLER [8], the research in that field regained
a great interest in solid state physics. A kind of minimal discrete model, that
describes electrons moving in a narrow band and interacting by a strong (repuls-
ive) Coulomb interaction, is the Hubbard model [9, 10, 11]. Here, the Coulomb
coupling is reduced to an on-site repulsion term U, which is physically justifiable
due to screening effects in a solid.

But recently models, that involve additional "longer ranging" two site terms
of the Coulomb repulsion, have been intensively discussed, since the Hubbard
model seems to be not a minimal model for some physical materials, e.g. poly-
acetylene [12] or the Bechgaard salts [13]. Generally, these models are called
extended Hubbard models. An interesting one has been proposed by HIRSCH
in 1989 [14], consisting of a *bond-charge interaction* term, which is also called
correlated hopping. Based on a BCS-type theory he and MARSIGLIO showed
[15, 16, 17, 18] that his model can lead to an effective attraction of holes in a
nearly filled band and thus to (hole) superconductivity.

In a first part of the thesis we present a detailed thermodynamic study of the
one-dimensional Hirsch model, using the TMRG algorithm. Even though some
research was already done here for vanishing temperature $T = 0$, finite tem-
perature $T > 0$ properties are almost unknown. We especially focus on the nu-
merical calculation of thermal correlations, which is a fairly new field of TMRG
research. The aim is to elucidate the model's tendency to superconductivity for
finite temperatures.

Our work with the TMRG algorithm also leads to intensive contentions with the
method inherently. A completely different application field came into consid-
eration: stochastic models which describe physics "far away" from the thermal
equilibrium. Such non-equilibrium processes are found in several pure physical,
but also many interdisciplinary fields, e.g. chemical reactions [19], traffic on a
highway [20], etc. Generically, stochastic models stand to reason, if the micro-
scopic dynamics are not exactly known, but empirical transition probabilities
are available.

Strong correlation effects are also of central interest here, especially in low
dimensions. But the theoretical framework of non-equilibrium collective phe-
nomena is less elaborated than in the equilibrium counterpart. The typical
numerical way to investigate stochastic models are (Monte-Carlo) simulations.
This means nothing else than randomly generating and averaging over possible
configurations of the model. Even though this is a nicely simple and powerful
numerical technique, a number of problems are known particularly at criticality
(e.g. critical slowing down).

Considerable theoretical progress was made, as ALEXANDER and HOLSTEIN
[21] found out, that the master equation of (certain) stochastic models can be
mapped onto a Schrödinger equation in "imaginary time". The close analogy
facilitates – at least formally – the adaption of quantum mechanical theories to

the stochastic case, e.g. the definition of a stochastic Hamiltonian or concepts like criticality, universality, conformal invariance, scaling, etc.

Inspired by the close relationship between quantum and stochastic models, the idea came up to apply the TMRG to non-equilibrium physics. Instead of the (reciprocal) temperature, the *time* represents the second dimension of the Trotter-Suzuki decomposition, if it is applied to the time evolution operator. At first glance, this analogy seems to be rather close. But the contrast of the physics manifest itself in astonishingly exceptional properties of the so-called "stochastic TMRG". The non-equilibrium, time-dependent nature of stochastic models leads to a kind of causal structure, that considerably influences the algorithm and unfortunately leads to inherent numerical problems.

The second part of the thesis therefore proposes a new TMRG based algorithm for stochastic models, which we call – due to the causal structure – stochastic light-cone corner-transfer matrix DMRG (LCTMRG). This method is based on a corner-transfer-matrix approach, similary as introduced by NISHINO and OKUNISHI in the context of classical two-dimensional systems [22, 23]. By means of feasibility studies of two well-known reaction-diffusion models we will judge about the numerical precision of the LCTMRG. Additionally we clarify the advantages arising from an approach, which is not a simulation technique and speculate about its future prospects.

Layout of the Thesis

Chapter 1 starts with a detailed overview of White's density-matrix renormalization-group (DMRG) algorithm in its historical context (section 1.1). We then discuss how the DMRG concept is transfered onto the thermodynamic case and elucidate the TMRG algorithm (section 1.2). Two variants are presented, the "traditional algorithm" following works XIANG et al. [6, 7] and a novel one proposed by SIRKER and KLÜMPER [24, 25].

Chapter 2 first reviews Hubbard's *tight-binding* approximation of fermions in a Coulomb potential (section 2.1), that provides the theoretical basis for the extended Hubbard models. Due to the restricted topology, one-dimensional fermion systems are usually described by TOMONAGA-LUTTINGER and LUTHER-EMERY liquid theory, whose basic properties are summarized (section 2.2) and build the theoretic framework for the interpretation of our numerical results as well. Then we focus on the special extended Hubbard model concerned in this thesis, namely the Hirsch model (section 2.3), and review its current state of research.

Chapter 3 presents our numerical computations for the Hirsch model. First, we mention some important details, how the "standard" TMRG algorithm is correctly applied to fermion systems (section 3.1). Then, TMRG data for the thermodynamics are shown and discussed in comparison with previous works (section 3.2), including also a precision check of the method. The chapter closes with an analysis of thermal correlation functions (section 3.3).

In **Chapter 4** we turn to the world of non-equilibrium physics (section 4.1), which represents the second part of the present thesis. We focus on stochastic

processes in continuous time, but also sketch the discrete time case (section 4.2). Then, we review some conceptual facts about non-equilibrium criticality and universality classes (section 4.3). The chapter closes with an introduction of a particular class of stochastic models, namely reaction-diffusion processes (section 4.4), since they will be studied numerically later on.

Chapter 5 outlines the stochastic TMRG algorithm, that is an almost one-to-one adaption of the quantum TMRG method onto the stochastic case. After displaying the specialties of the algorithm (section 5.1), important properties of the stochastic transfer-matrix (section 5.2) and the density-matrix projection (section 5.3) are discussed. Finally we point out principal numerical instabilities that restrict the method's capability (section 5.4).

Chapter 6 introduces the newly proposed stochastic light-cone CTMRG algorithm. On the basis of corner-transfer-matrices (section 6.2) we outline the concept of the LCTMRG method (section 6.3), focusing on the most crucial part of choosing the correct density-matrix projection (section 6.4) and alluding to some additional technical details (section 6.5). Finally we exemplary investigate two well-known reaction diffusion models using the LCTMRG (section 6.6). Hereby, our aim is to judge the quality of the numerical results.

Chapter 7 draws the conclusion of this thesis and proposes perspectives for further research on the presented topics.

1. The TMRG Algorithm

1.1. Introduction

The density-matrix renormalization group (DMRG), which was developed by
WHITE in 1992 [1, 2], is one of the most precise numerical methods to study
low-dimensional strongly correlated systems. Originally, it was introduced to
compute the ground state and low-energy spectrum of a quantum Hamiltonian
with short-range interactions. But meanwhile, there is a large number of vari-
ants using the basic DMRG idea of numerical renormalization in other physical
fields, see e.g. [26] as a general reference. One of these variants is the transfer-
matrix DMRG (TMRG) which can be used to study the thermodynamics of
(quasi) one-dimensional quantum systems.

In this section we give an overview of the DMRG and TMRG algorithms in
a historical context. The DMRG is an advancement of WILSON's numerical
renormalization group method (NRG), that is outlined in section 1.1.1. WHITE
augmented the NRG by the density-matrix projection (section 1.1.2) that is
the basic idea of each DMRG-style method. Thereupon, in section 1.1.3 the
"standard" DMRG algorithm is presented. The TMRG algorithm, which we
review in section 1.2, is an adaption of the DMRG concept to the so-called
transfer-matrix. A detailed overview about the algorithmic realization is given,
following works of XIANG et al. [6, 7] and SIRKER and KLÜMPER [24, 25].

1.1.1. Numerical Renormalization Group

The RG was first proposed by WILSON in 1971 to study critical phenomena
of quantum systems [27]. This original RG was based on the idea, that large
length scales dominate the physics at criticality and thus microscopic lengths are
renormalized. WILSON also first applied a pure numerical RG variant (NRG)
to the KONDO model and computed the ground state [28].

Figure 1.1 outlines Wilson's NRG approach. The algorithm starts with a
quantum chain (also called "block") of length L, that is sufficiently small to
be numerically represented on a computer. Then, the Hamiltonian H_L is en-
larged sequentially by one site to increase the system size. In order to reduce
the exponentially growing dimension of the Hilbert space, H_L is renormalized
after each enlargement step by retaining only a *fixed* number m of Hilbert space
states. All remaining states are cut off and neglected for the next iteration step.
Obviously the crucial question arises which states are in that sense "relevant"
to find an optimal truncation procedure. In Wilson's NRG the Hamiltonian is
diagonalized to keep only the m states of lowest-energy. Alternating the renor-
malization and enlargement step, the "effective" block size thereby is increased,
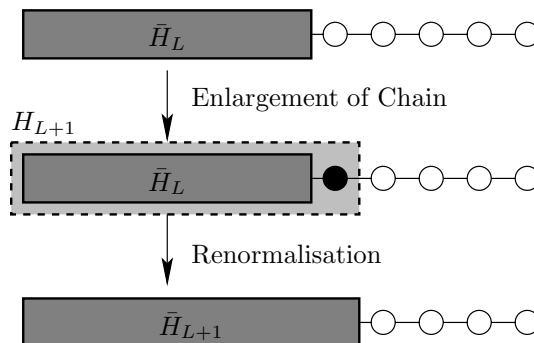
Figure 1.1.: Schematic plot of Wilson NRG method.

while the Hamilton operator of dimension $m \times m$ is kept representable by the computer algorithm.

The key problem of this RG method is, that the energetically lowest eigenstates are assumed to be an optimal renormalization basis for the ground state. In the Kondo problem this situation is indeed realized. But applications of the NRG to e.g. the Heisenberg or Hubbard model do not provide this feature. Here, the NRG provides only poor numerical results for the ground state [29, 30].

1.1.2. Density-Matrix Projection

The problem, which states are relevant in a RG step to represent the ground state, was solved by White's density-matrix (DM) projection. This section presents a detailed mathematical formulation of the DM projection [31], which is the basis of all "DMRG-like" algorithms.

We start with the block Hamiltonian

$$H_L = \sum_{i=1}^{L-1} h_{i,i+1} \tag{1.1}$$

of chain length L and next-neighbor interactions $h_{i,i+1}$, operating on a Hilbert space $\mathfrak{H}_s$. The idea of the DM projection is to embed H_L into a larger quantum chain. This is typically done by mirroring H_L to construct the so-called superblock

$$H_{\text{super}} = H_L \otimes \text{id}_L + h_{L,L+1} + \text{id}_L \otimes H_L . \tag{1.2}$$

Figure 1.2 depicts the superblock, which is split up into the so-called system block $\mathfrak{H}_s$ and environment block $\mathfrak{H}_e$. The DM projection is designed to compute a small set of $m < k := \dim \mathfrak{H}_s$ states $|u_i\rangle \in \mathfrak{H}_s$ $(i = 1 \ldots m)$ which are important to represent the ground state (also called *target state*) of the superblock

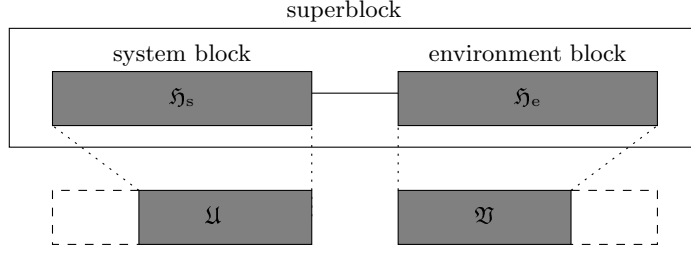$$|\psi\rangle = \sum_{ij} \psi_{ij} |i\rangle_{\text{s}} \otimes |j\rangle_{\text{e}}. \tag{1.3}$$

Figure 1.2.: Schematic diagram of the superblock, that consists of a system and environment block.

Here, $\left|i\right\rangle_\mathrm{s}$ $(i = 1 \ldots k)$ and $\left|j\right\rangle_e$ $(j = 1 \ldots k)$ label an orthonormal basis of the Hilbert space $\mathfrak{H}_\mathrm{s}$ and $\mathfrak{H}_\mathrm{e}$, respectively.

The problem of finding optimal representation vectors $\left|u_i\right\rangle$ can be mathematical formulated as follows: Find an optimal m-dimensional subspace $\mathfrak{U} \in \mathfrak{H}_s$ and a vector

$$\left|\tilde\psi\right\rangle = \sum_{ij} \tilde\psi_{ij} \left|u_i\right\rangle_\mathrm{s} \otimes \left|j\right\rangle_\mathrm{e} \in \mathfrak{U} \otimes \mathfrak{H}_e, \tag{1.4}$$

that minimize the functional

$$S\big(\left|\tilde\psi\right\rangle\big) := \big\| \left|\psi\right\rangle - \left|\tilde\psi\right\rangle \big\|^2 . \tag{1.5}$$

We show, that the optimal $\left|u_i\right\rangle$ are given by the eigenvectors of the leading eigenvalues of the reduced DM

$$\rho := \mathrm{tr}' \left|\psi\right\rangle\!\left\langle\psi\right| , \tag{1.6}$$

where $\mathrm{tr}' := \mathrm{id}_\mathrm{s} \otimes \mathrm{tr}_\mathrm{e}$ labels the partial trace over the environment block. We interpret the coefficients ψ_{ij} and $\tilde\psi_{ij}$ as $k \times k$ matrices $\psi = (\psi_{ij})_{ij}$ and $\tilde\psi = (\psi_{ij})_{ij}$ (where $\mathrm{rank}(\tilde\psi) \le m$) respectively. Then, the DM ρ can be written as $\rho = \psi\psi^\dagger$ and the functional $S(\left|\tilde\psi\right\rangle)$ turns to

$$S(\tilde\psi) = \mathrm{tr}\,(\psi - \tilde\psi)^\dagger(\psi - \tilde\psi) . \tag{1.7}$$

Using the *singular value decomposition* theorem (SVD) [32] one can simplify equation (1.7). According to the SVD there exist two orthogonal $k \times k$ matrices U and V such that

$$\psi = UDV^\dagger , \quad \text{whereby} \quad D = \mathrm{diag}(\sigma_1, \ldots, \sigma_k, 0, \ldots, 0). \tag{1.8}$$

The so-called *singular values* σ_i are the square roots of the eigenvalues ρ_i of ρ, because

$$\rho = UDD^\dagger U^\dagger = UD^2 U^\dagger . \tag{1.9}$$

Without loss of generality the σ_i are sorted: $\sigma_1 \ge \sigma_2 \ge \cdots \ge \sigma_k$. Inserting (1.8) into (1.7) we obtain

$$S(\tilde\psi) = \mathrm{tr}\,(D - \tilde D)^\dagger(D - \tilde D) . \tag{1.10}$$

whereby $\tilde{D} := U^\dagger \tilde{\psi} V$. Obviously, S is minimized by a diagonal matrix $\tilde{D}$ of rank m, whose diagonal elements are given by the leading singular values, i.e.

$$\tilde{D} = \mathrm{diag}(\sigma_1, \ldots, \sigma_m, 0, \ldots, 0) \ . \tag{1.11}$$

Hence, we can explicitly construct $\big|\tilde{\psi}\big\rangle$ which minimizes S:

$$
\begin{aligned}
\big|\tilde{\psi}\big\rangle &= \sum_{ij} (U\tilde{D}V^\dagger)_{ij} \big|i\big\rangle_{\mathrm{s}} \otimes \big|j\big\rangle_{\mathrm{e}} = \sum_{ij} \tilde{D}_{ij} \big(\underbrace{U\big|i\big\rangle_{\mathrm{s}}}_{\big|u_i\big\rangle} \big) \otimes \big(\underbrace{V\big|j\big\rangle_{\mathrm{e}}}_{\big|v_j\big\rangle} \big) \\
&= \sum_{i=1}^{m} \sigma_i \big|u_i\big\rangle_{\mathrm{s}} \otimes \big|v_i\big\rangle_{\mathrm{e}} \tag{1.12}
\end{aligned}
$$

The vectors $\big|u_i\big\rangle_{\mathrm{e}}$ $(i = 1 \ldots m)$ are the leading eigenvectors of ρ, cf. eq. (1.9). We have proved that the relevant states of the system block to represent the ground state of a larger quantum chain are optimally given by the leading eigenvectors of the reduced DM. Note, that also the environment block has been automatically projected to a subspace $\mathfrak{V} = \mathrm{span}\{\big|v_i\big\rangle_e\}$, cf. figure 1.2. The truncation error made by cutting off the subspace $\mathfrak{U}^\perp$ can be measured by the so-called *discarded weight*

$$P := 1 - \sum_{i=1}^{m} \rho_i. \tag{1.13}$$

The faster the ρ_i decrease, the better normally the renormalization step performs. Thus, the DM spectrum is a good indicator for the quality of the DM projection. For some integrable models the DM spectrum can be obtained exactly [33], typically showing a fast exponential decay.

Without going into the details we also mention that other types of DM are possible depending on which states have to be targeted. E.g. in order to compute the excitation spectrum's gap of a quantum system, not only the ground state $\big|\psi_0\big\rangle$, but also the first exited state $\big|\psi_1\big\rangle$ should be involved in the reduced DM, namely

$$\rho = \frac{1}{2} \mathrm{tr}' \left(\big|\psi_0\big\rangle\big\langle\psi_0\big| + \big|\psi_1\big\rangle\big\langle\psi_1\big| \right) \ . \tag{1.14}$$

1.1.3. The DMRG Algorithm

We focus here on the so-called *infinite size* DMRG algorithm. As a counterpart we mention the *finite size* algorithm [34], which is not used in this work. Often, both algorithms are combined to obtain an increased accuracy of the numerical results.

The infinite size algorithm is designed for computing the ground state (or low-energy spectrum) of a quantum chain in the thermodynamic limit $L \to \infty$. It contains the following iterative steps:

1. Construct and store the system block of size L

$$H_{\mathrm{s}} = \sum_{i=1}^{L-1} h_{i,i+1} = \boxed{\ \bullet\!\!-\!\!\bullet\!\!-\!\!\bullet\!\!-\!\!\bullet\ } \quad . \tag{1.15}$$

If any (local) expectation value is desired to be measured, store the matrix

$$A = \sum_{i=1}^{L} a_i \qquad (1.16)$$

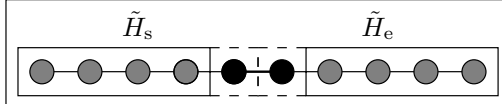with a_i being an arbitrary local operator of site i.

2. Enlarge the system block by one site

$$\tilde{H}_{\mathrm{s}} = H_{\mathrm{s}} \otimes \mathrm{id} + h_{L,L+1} = \qquad (1.17)$$

and similarly the expectation value operator

$$\tilde{A} = A \otimes \mathrm{id} + a_{L+1} \ . \qquad (1.18)$$

3. Construct the superblock

$$H_{\mathrm{super}} = \tilde{H}_{\mathrm{s}} + h_{L+1,L+2} + \tilde{H}_{\mathrm{e}}$$

$$\tilde{H}_{\mathrm{s}} \qquad \tilde{H}_{\mathrm{e}}$$

where the environment block $\tilde{H}_{\mathrm{e}}$ is obtained by mirroring the system block $\tilde{H}_{\mathrm{s}}$. Compute the ground state $|\psi\rangle$ (and excitations where required) numerically.

4. Compute the reduced density-matrix ρ and its complete eigenspectrum $\{\rho_i, |u_i\rangle\}$. Write the orthonormal eigenstates of the m leading eigenvalues into a matrix U.

5. Compute all local expectation values

$$\langle A \rangle = \mathrm{tr}\ \rho \tilde{A} \ . \qquad (1.19)$$

6. Project all operators onto the reduced basis using the operator U, i.e.

$$H_{\mathrm{s}} = U^{\dagger} \tilde{H}_{\mathrm{s}} U, \quad A = U^{\dagger} \tilde{A} U \qquad (1.20)$$

$$\longrightarrow \quad \boxed{H_{\mathrm{s}}}$$
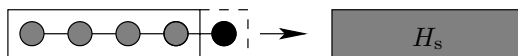
and continue from step 2.

Obviously, the chain length grows successively by each iteration step, whereas the effective size of the system's Hamiltonian stays constant. By finite size analysis, highly precise estimates of various properties of the infinitely large quantum chain are possible.

The scheme given above is only a rough sketch of the DMRG algorithm. An implementation of a DMRG program facilitates various numerical know-how to increase the performance and to save computer memory. Typically, quantum numbers reduce operators to a block structure, such that vanishing matrix elements do not have to be stored. The most time consuming part of the algorithm is found in the computation of the ground state. Here, the DAVIDSON [35] or LANCZOS [36] algorithm are typically used due to their high performance.

1.2. The TMRG Algorithm

In general, all thermodynamic quantities of a d dimensional quantum system can be derived analytically from the partition function

$$Z = \text{tr}\left(e^{-\beta H}\right) = \sum_i e^{-\beta E_i} . \tag{1.21}$$

Hence, in principle one has to diagonalize the Hamiltonian to obtain the whole spectrum E_i, which is analytically impossible in most cases. It is also a hopeless way to compute the whole spectrum numerically due to the large dimension of the Hilbert space.

A promising alternative approach is given by the TROTTER-SUZUKI decomposition [5, 4, 37], where the quantum system is first mapped onto a *classical* two-dimensional lattice, cf. fig. 1.3. The classical system is then solved in terms of a transfer-matrix formulation, which we describe in detail in section 1.2.1. As a crucial result it is found, that the thermodynamics of the quantum chain are determined by the *leading* eigenvalue Λ_0 of the so-called quantum transfer-matrix (QTM).
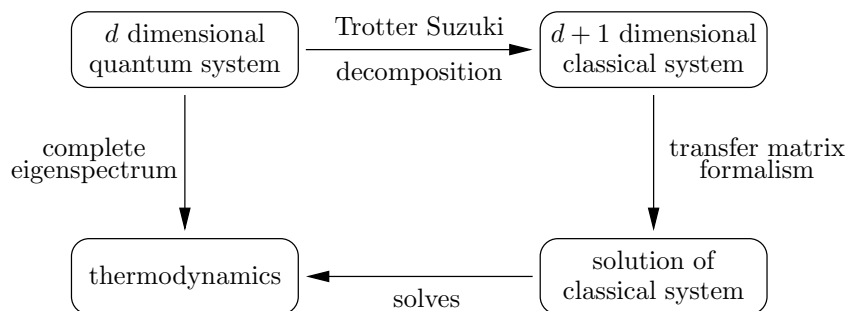
Figure 1.3.: Schematic plot of the Trotter-Suzuki decomposition.

For some integrable models (such as the Hubbard model [38] or the supersymmetric tJ model [38, 39]) Λ_0 can even be calculated analytically. For arbitrary models the TMRG algorithm introduced by XIANG et al. provides a precise numerical technique to obtain Λ_0, which is nothing else than the consequent adaption of the DMRG onto the QTM. The concepts of the algorithm are summarized in section 1.2.2. Finally, we focus on some details of the numerical implementation in section 1.2.3, which are important for a successful realization of a TMRG computer program.

1.2.1. The Transfer-Matrix Formalism

Our starting point is an arbitrary one dimensional Hamiltonian

$$H = \sum_{i=1}^{L} h_{i,i+1} \tag{1.22}$$

of length L with periodic boundary conditions $h_{L,L+1} = h_{L,1}$. H acts on a Hilbert space $\mathfrak{H} = \mathfrak{h}^{\otimes i}$ of a one-dimensional quantum chain. With $\mathfrak{h}$ we label the local Hilbert space of site i with dimension $n = \dim \mathfrak{h}$. We further assume that the local interaction $h_{i,i+1}$ conserves parity, i.e. $h_{i,i+1} = h_{i+1,i}$.

In this section, we present two different Trotter-Suzuki mappings. The first one is the basis of the "traditional" quantum TMRG algorithm introduced by XIANG et al. [6, 7]. The second one was first used for TMRG by SIRKER and KLÜMPER [24, 25] and has some advantages and disadvantages, which we describe later on.

In the traditional mapping the interactions of the Hamiltonian are split up into an odd and an even part

$$H_{\mathrm{o}} = \sum_{i \ \mathrm{odd}} h_{i,i+1}, \quad H_{\mathrm{e}} = \sum_{i \ \mathrm{even}} h_{i,i+1}, \quad H = H_{\mathrm{o}} + H_{\mathrm{e}} \ . \tag{1.23}$$

The partition function is then expressed by the TROTTER formula [5]

$$Z = \mathrm{tr}\left(\mathrm{e}^{-\beta H}\right) = \lim_{M \to \infty} \left(\mathrm{e}^{-\epsilon H_{\mathrm{o}}} \mathrm{e}^{-\epsilon H_{\mathrm{e}}}\right)^{M} , \tag{1.24}$$

where $\epsilon = \beta/M$. If we omit the limit $M \to \infty$ and fix ϵ, the Trotter formula approximates the partition function

$$Z = \mathrm{tr}\left(\mathrm{e}^{-\epsilon H_{\mathrm{o}}} \mathrm{e}^{-\epsilon H_{\mathrm{e}}}\right)^{M} + \mathcal{O}(\epsilon^2) , \tag{1.25}$$

whereby one can show, that the error is of the order $\mathcal{O}(\epsilon^2)$ [25].

A fixed ϵ thereby discretizes the temperature

$$T = \frac{1}{\epsilon M} \ . \tag{1.26}$$

Inserting $2M$ identity operators into the partition function yields

$$\begin{aligned} Z \ &= \ \sum_{\{\alpha\}} \left\langle \alpha_1 \big| \mathrm{e}^{-\epsilon H_{\mathrm{o}}} \big| \alpha_2 \right\rangle \left\langle \alpha_2 \big| \mathrm{e}^{-\epsilon H_{\mathrm{e}}} \big| \alpha_3 \right\rangle \cdots \\ &\quad \times \left\langle \alpha_{2M-1} \big| \mathrm{e}^{-\epsilon H_{\mathrm{o}}} \big| \alpha_{2M} \right\rangle \left\langle \alpha_{2M} \big| \mathrm{e}^{-\epsilon H_{\mathrm{e}}} \big| \alpha_1 \right\rangle \ . \end{aligned} \tag{1.27}$$

Here, the vectors

$$\big| \alpha_j \big\rangle = \bigotimes_{i=1}^{L} \big| s_j^i \big\rangle \in \mathfrak{H}, \quad j = 1 \dots 2M \tag{1.28}$$

are tensor products of $s_j^i = 1 \dots n$, which denote a local orthonormal basis of $\mathfrak{h}$. As H_{o} and H_{e} consist of commuting local interactions $h_{i,i+1}$ only, they resolve into a product

$$\mathrm{e}^{-\epsilon H_{\mathrm{e/o}}} = \prod_{i \ \mathrm{even/odd}} \mathrm{e}^{-\epsilon h_{i,i+1}} \ . \tag{1.29}$$

Therefore, the partition function can be written as

$$Z = \sum_{\{s\}} \left(\tau_{1,2}^{1,2}\tau_{1,2}^{3,4}\cdots\tau_{1,2}^{L-1,L}\right)\left(\tau_{2,3}^{2,3}\tau_{2,3}^{4,5}\cdots\tau_{2,3}^{L,1}\right)\cdots \tag{1.30}$$

$$\times \left(\tau_{2M-1,2M}^{1,2}\cdots\tau_{2M-1,2M}^{L-1,L}\right)\left(\tau_{2M,1}^{2,3}\cdots\tau_{2M,1}^{L-1,L}\right) \,,$$

where we used $\tau_{j,j+1}^{i,i+1}$ as an abbreviation of the tensor elements

$$\tau_{j,j+1}^{i,i+1} := \left\langle s_j^i s_j^{i+1}\big|\mathrm{e}^{-\epsilon h_{i,i+1}}\big|s_{j+1}^i s_{j+1}^{i+1}\right\rangle \,. \tag{1.31}$$

The expression (1.30) is a kind of *lattice path integral* representation of the partition function Z. This is visualized in figure 1.4, which shows a checkerboard style lattice.
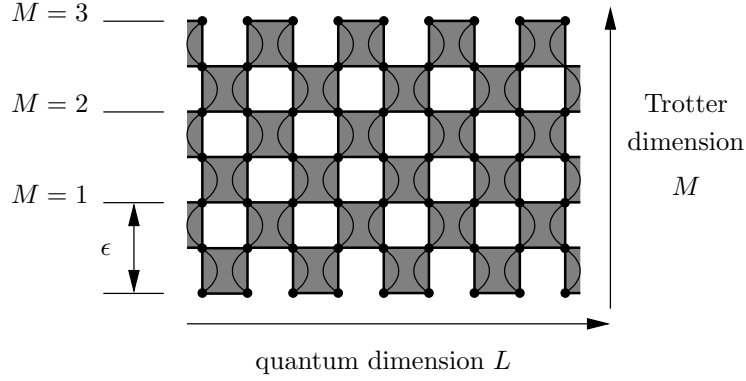

Figure 1.4.: Schematic plot of the two-dimensional classical lattice of the Trotter-Suzuki decomposition. The figure shows the special case of Trotter dimension $M = 3$.

The sites of the lattice, given by the basis states s_j^i, interact by local plaquettes

$$\tau_{j,j+1}^{i,i+1} \quad = \quad \begin{matrix} s_{j+1}^i \quad s_{j+1}^{i+1} \\ \fbox{} \\ s_j^i \quad s_j^{i+1} \end{matrix} \quad . \tag{1.32}$$

Here we used a special pictorial representation of the plaquettes to allude particularly to the symmetries:

$$\tau_{j,j+1}^{i,i+1} = \tau_{j+1,j}^{i,i+1} \quad \text{(hermicity)} \tag{1.33}$$

$$\tau_{j,j+1}^{i,i+1} = \tau_{j,j+1}^{i+1,i} \quad \text{(parity conservation)} \,. \tag{1.34}$$

One can now easily conclude by equation (1.30), that Z corresponds to the partition function of the shown two dimensional model with *classical* spins s_i^j. Hence, the quantum dimension L has been expanded by a virtual Trotter dimension M, taking the role of the imaginary time of the lattice path integral.

Note, that the Trotter-Suzuki decomposition also leads to periodic boundary conditions in Trotter direction M.

The key point of the TMRG is that the classical model provides the thermodynamics of the quantum model. Consequently, we rather solve the two-dimensional classical models, which is done in terms of a transfer-matrix formalism.

We define the so-called *quantum transfer-matrix* (QTM) T_M with matrix elements

$$
\langle \{s^i\} | T_M | \{s^{i+2}\} \rangle = \sum_{\{s^{i+1}\}} \left(\tau_{1,2}^{i,i+1} \tau_{3,4}^{i,i+1} \cdots \tau_{2M-1,2M}^{i,i+1} \right)
$$
$$
\times \left(\tau_{2,3}^{i+1,i+2} \tau_{4,5}^{i+1,i+2} \cdots \tau_{2M,1}^{i+1,i+2} \right)
$$

$$
\tag{1.35}
$$

Here, a column of the lattice was joined for the construction of T_M (cf. figure 1.4). Due to a (two site) translational invariance in L direction, T_M does not depend on i. Hence, we abbreviate eq. (1.35) by

$$
T_M = \left(\tau_{1,2} \tau_{3,4} \cdots \tau_{2M-1,2M} \right) \cdot \left(\tau_{2,3} \tau_{4,5} \cdots \tau_{2M,1} \right) . \tag{1.36}
$$

Now equation (1.30) takes the simple form

$$
Z = \operatorname{tr} T_M^{L/2} = \sum_\mu \Lambda_\mu^{L/2} . \tag{1.37}
$$

The eigenspectrum of T_M, denoted by Λ_μ, is *not* necessarily real. As one can imagine by the shape of T_M in eq. (1.35), T_M is in general not symmetric. Moreover, left and right eigenvectors (i.e. those of T_M and $T_M^\dagger$, respectively) have to be distinguished.

The eigenvalues are now assumed to be sorted, i.e. $|\Lambda_\mu| \geq |\Lambda_{\mu+1}|$. The leading eigenvalue Λ_0 is usually not degenerate and we have a finite gap $\Lambda_0 \neq \Lambda_1$. This can be explained by considering the high temperature case $T \to \infty$, where

$$
\tau_{j,j+1}^{i,i+1} = \delta_{s_j^i, s_{j+1}^i} \delta_{s_j^{i+1}, s_{j+1}^{i+1}} = \quad \text{} \tag{1.38}
$$

becomes unity.

Giving a pictorial proof in fig. 1.5 we can show

$$
T_M^2 = n^2 T_M \quad \text{and} \tag{1.39}
$$
$$
\operatorname{tr} T_M = n^2 . \tag{1.40}
$$

$$\mathrm{tr}\, T_M \qquad\qquad n^2 \qquad\qquad\qquad T_M^2 \qquad\qquad n^2 \quad\cdot\quad T_M$$
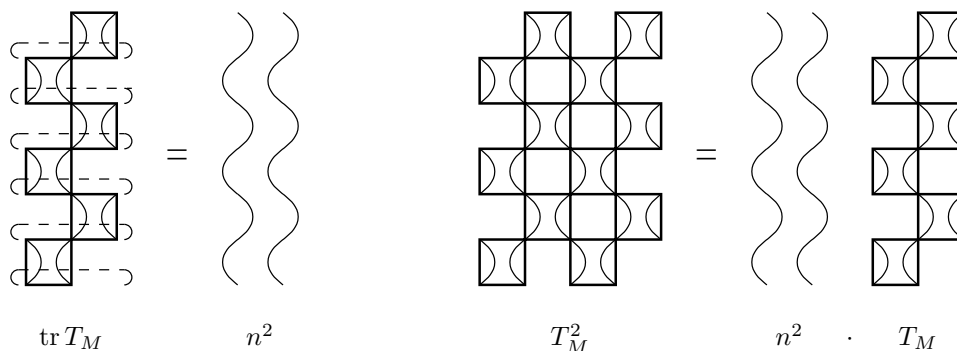
Figure 1.5.: Pictorial proof of eq. (1.39) and (1.40). The figure shows the trace of T_M and its second power T_M^2. Since the local plaquettes are unity, the "connected" indices have to be equal. The summation over a "column" of such indices, depicted by curved lines, contributes by a factor n due to n local spin configurations.

From eq. (1.39) it is evident that $\Lambda_\mu = n^2$ or $\Lambda_\mu = 0$. Then, eq. (1.40) determines the spectrum

$$\mathrm{spec}\, T_M = \left\{ n^2, 0, \ldots, 0 \right\} \tag{1.41}$$

and verifies a gapped transfer-matrix at infinite temperatures. Since a phase transition is not possible for one-dimensional quantum systems with short range interactions, the gap is expected to persist for any finite temperature $T > 0$. Equation (1.37) is nicely suited to perform the thermodynamic limit $L \to \infty$ of the quantum dimension exactly. For large L we find

$$T_M^{L/2} = \sum_\mu \Lambda_\mu^{L/2} |\Lambda_\mu^R\rangle\langle\Lambda_\mu^L| \xrightarrow{L\to\infty} \Lambda_0^{L/2} |\Lambda_0^R\rangle\langle\Lambda_0^L| \tag{1.42}$$

and

$$Z \xrightarrow{L\to\infty} \Lambda_0^{L/2} . \tag{1.43}$$

Consequently, the free energy per site in the thermodynamic limit reduces to depend only on the leading eigenvalue Λ_0

$$f_{\infty,M} = -T \lim_{L\to\infty} \frac{1}{L} \ln Z = -\frac{T}{2} \ln \Lambda_0 . \tag{1.44}$$

Note, that $f_{\infty,M}$ is still an approximation and does not represent the bulk limit $f_{\infty,\infty}$ of the quantum chain. The "finite size" corrections due to M are (cf. eq. (1.25))

$$f_{\infty,M} = f_{\infty,\infty} + \mathcal{O}(\epsilon^2) . \tag{1.45}$$

It is well known, that the complete thermodynamics can be analytically derived from the free energy. But in the face of the later numerical algorithm based on the QTM approach, it is convenient to compute local observables in a different manner. We consider an arbitrary operator $O_{i,i+1}$, which acts on two neighboring sites i and $i+1$, and express $\langle O_{i,i+1} \rangle$ in the transfer-matrix formalism by

$$\langle O_{i,i+1} \rangle = \frac{1}{Z} \mathrm{tr}\left(O_{i,i+1} e^{-\beta H} \right) = \frac{1}{Z} \mathrm{tr}\left(T_M(O) T_M^{L/2-1} \right) . \tag{1.46}$$

Here, $T_M(O)$ denotes a modified QTM

$$T_M(O) = \big(\tau_{1,2}(O)\tau_{3,4}\cdots\tau_{2M-1,2M}\big)\big(\tau_{2,3}\tau_{4,5}\cdots\tau_{2M,1}\big) \qquad (1.47)$$

where one plaquette $\tau_{1,2}(O)$ embeds O

$$\tau(O)^{i,i+1}_{j,j+1} := \big\langle s^i_j s^{i+1}_j \big| O_{i,i+1} \mathrm{e}^{-\epsilon h_{i,i+1}} \big| s^i_{j+1} s^{i+1}_{j+1} \big\rangle \ . \qquad (1.48)$$

Note that in eq. (1.47) the indices of O are omitted, because O can be measured at an arbitrary site due to translational invariance. For the thermodynamic limit $L \to \infty$, eq. (1.46) reduces to

$$\langle O_{i,i+1}\rangle = \frac{1}{Z}\,\mathrm{tr}\big(T_M(O)T_M^{L/2-1}\big) \xrightarrow{L\to\infty} \frac{\Lambda_0^{L/2-1}}{\Lambda_0^{L/2}}\,\mathrm{tr}\big(T_M(O)|\Lambda_0^R\rangle\langle\Lambda_0^L|\big)$$

$$= \frac{\langle\Lambda_0^L|T_M(O)|\Lambda_0^R\rangle}{\Lambda_0} \ . \qquad (1.49)$$

In this thesis we also regard thermal two-point correlation functions $G_O(r) = \langle\delta O_1\delta O_r\rangle$, where $\delta O_r = O_r - \langle O_r\rangle$ and O_r is a one or two site operator. In a similar way to eq. (1.49) one obtains

$$G_O(r) = \mathrm{tr}\big(\delta O_1\delta O_r\mathrm{e}^{-\beta H}\big) \xrightarrow{L\to\infty} \frac{\langle\Lambda_0^L|T_M(\delta O)T_M^{r/2-1}T_M(\delta O)|\Lambda_0^R\rangle}{\Lambda_0^{r/2+1}}$$

$$= \sum_{\alpha\neq 0}\underbrace{\frac{\langle\Lambda_0^L|T_M(\delta O)|\Lambda_\alpha^R\rangle\langle\Lambda_\alpha^L|T_M(\delta O)|\Lambda_0^R\rangle}{\Lambda_0\Lambda_\alpha}}_{M_\alpha}\left(\frac{\Lambda_\alpha}{\Lambda_0}\right)^{r/2}$$

$$=: \sum_\alpha M_\alpha\mathrm{e}^{-r/\xi_\alpha}\mathrm{e}^{\mathrm{i}k_\alpha r} \qquad (1.50)$$

where we have introduced *thermal correlation lengths* (CL) ξ_α and *wave vectors* k_α

$$\xi_\alpha^{-1} = \frac{1}{2}\ln\frac{\Lambda_0}{|\Lambda_\alpha|} \quad\text{and}\quad k_\alpha = \frac{1}{2}\arg\left(\frac{\Lambda_0}{\Lambda_\alpha}\right) \mod \pi \ . \qquad (1.51)$$

The asymptotic behavior $G_O(r \to \infty)$ is dominated by the largest CL ξ_α, for which the matrix element M_α does not vanish. Note, that due to the gap in T_M the CLs ξ_α are well defined. Moreover we conclude that all correlation functions G_O decay exponentially.

The checkerboard lattice is translational invariant in space direction L, but only with a double unit cell. This complicates the calculation of k_α, since one can not distinguish between k_α and $k_\alpha + \pi$. This problem was solved in the context of TMRG by SIRKER and KLÜMPER, who used a different QTM [25, 24]. Instead of eq. (1.25) we write

$$Z = \mathrm{tr}\big(\mathcal{T}_1\mathcal{T}_2\big)^{M/2} \quad\text{with}\quad \mathcal{T}_{1/2} = \mathcal{T}_{L/R}\left(\mathrm{e}^{-\epsilon H + \mathcal{O}(\epsilon^2)}\right) \qquad (1.52)$$

where $\mathcal{T}_{L/R}$ is the shift left and right operator, respectively. The corresponding lattice is shown in fig. 1.6 (a). In contrast to the checkerboard lattice, the
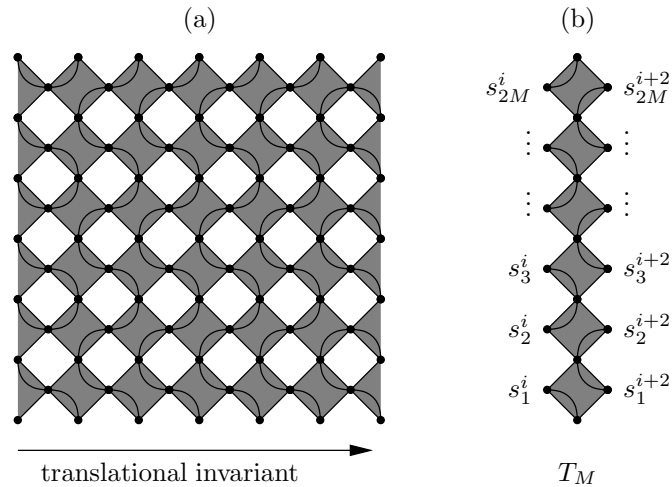
Figure 1.6.: Alternative Trotter-Suzuki decomposition of the thermodynamics. Figure (a) depicts the classical lattice, (b) the corresponding quantum transfer-matrix.

number of lattice sites per Trotter step M has doubled. Consequently, we have to exchange ϵ by $\epsilon/2$ to make both decompositions comparable. As another important difference, the lattice of fig. 1.6 (a) is obviously fully translationally invariant in quantum direction L. The corresponding QTM T_M is shown in fig. 1.6 (b). As a consequence, the wave vectors k_α in eq. (1.51) are unique. Note, that additionally a factor $1/2$ has to be omitted, e.g. in eq. (1.44) and (1.51).

We have shown in the current section, that the calculation of the thermodynamics reduces to finding the leading eigenvalues Λ_α of the quantum transfer-matrix. In order to cover the whole temperature region it is necessary to increase M to lower the temperature (cf. eq. (1.26)). But the exponential dimension $n^{2M} \times n^{2M}$ of the QTM T_M generically prevents an exact treatment. Only in a few special case, the algebraic Bethe ansatz provides analytical solutions for Λ_0 for arbitrary M.

A promising numeric tool was proposed by XIANG et al. in 1996 [6, 7], which applies the DMRG algorithm onto the QTM and therefore is called (quantum) transfer-matrix DMRG (TMRG).

1.2.2. Implementation of the Algorithm

In principle, the TMRG algorithm is nothing else but the application of the DMRG method (cf. sec. 1.1) onto the quantum transfer matrix T_M. Whereas the DMRG is basically designed for computing the *ground state* and *low excitations*, respectively, the TMRG computes the leading part of the spectrum.

Historically, a numerical TMRG algorithm was first introduced by NISHINO in 1995 [3] in the framework of classical two-dimensional systems. XIANG et al. transfered their ideas to the thermodynamic case [6, 7]. Even if the basics of

the TMRG are closely related to its DMRG predecessor, the rich structure of the transfer-matrices turns the algorithm to be slightly more sophisticated.

Traditional TMRG Algorithm

First, we discuss the "traditional" TMRG method of XIANG et al. In order to exemplify the renormalization process we consider two special cases $M = 3$ and $M = 4$ (because odd and even Trotter numbers are handled slightly different). Schematically, the (infinite) TMRG algorithm proceeds by the following iterations steps:

1. Construct the system block

$$S = \begin{cases} (\tau_{1,2}\tau_{3,4}\cdots\tau_{M,M+1})(\tau_{2,3}\tau_{4,5}\cdots\tau_{M-1,M}) & \text{if } M \text{ odd} \\ (\tau_{1,2}\tau_{3,4}\cdots\tau_{M-1,M})(\tau_{2,3}\tau_{4,5}\cdots\tau_{M,M+1}) & \text{if } M \text{ even} \end{cases} \quad (1.53)$$

   and environment block

$$E = \begin{cases} (\tau_{M+2,M+3}\cdots\tau_{2M-1,2M})(\tau_{M+1,M+2}\cdots\tau_{2M,1}) & \text{if } M \text{ odd} \\ (\tau_{M+1,M+2}\cdots\tau_{2M-1,2M})(\tau_{M+2,M+3}\cdots\tau_{2M,1}) & \text{if } M \text{ even} \end{cases} \quad (1.54)$$

   respectively, which are depicted in fig. 1.7. We write the tensors S and E
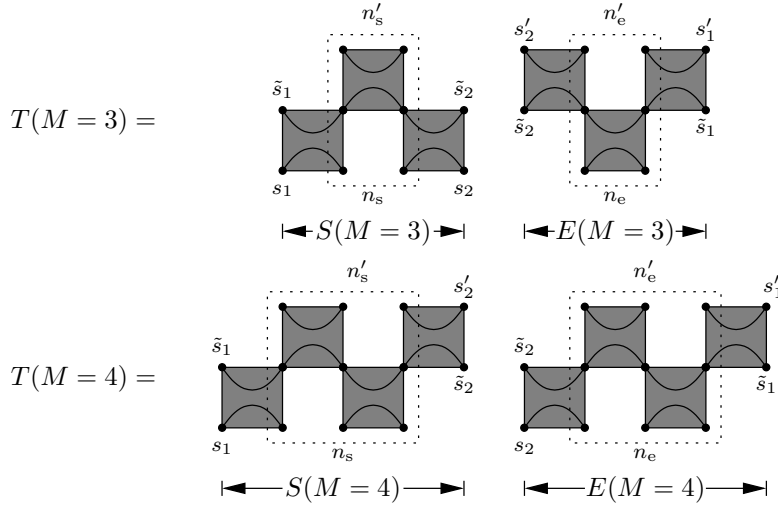
Figure 1.7.: System and environment block in the TMRG algorithm for the special cases $M = 3$ and $M = 4$.

   in a basis representation

$$\left(S^{s_1' n_s' s_2'}_{s_1 n_s s_2}\right) \quad \text{and} \quad \left(E^{s_1' n_e' s_2'}_{s_1 n_e s_2}\right) \ . \quad (1.55)$$

   Here, the s-indices label single spin sites, whereas the n-indices join $M-1$ spins to a block spin. Thus, the dimension of S and E is $n^4 \cdot \tilde{m}^2$ with $\tilde{m} = n^{2(M-1)}$.

As shown by fig. 1.7 the QTM is assembled by

$$T_M{}_{s_1 n_{\mathrm{s}} s_2 n_{\mathrm{e}}}^{s_1' n_{\mathrm{s}}' s_2' n_{\mathrm{e}}'} = \begin{cases} S_{s_1 n_{\mathrm{s}} s_2}^{\tilde{s}_1 n_{\mathrm{s}}' \tilde{s}_2} \cdot E_{\tilde{s}_2 n_{\mathrm{e}} \tilde{s}_1}^{s_2' n_{\mathrm{e}}' s_1'} & \text{if } M \text{ odd} \\[2mm] S_{s_1 n_{\mathrm{s}} \tilde{s}_2}^{\tilde{s}_1 n_{\mathrm{s}}' s_2'} \cdot E_{s_2 n_{\mathrm{e}} \tilde{s}_1}^{\tilde{s}_2 n_{\mathrm{e}}' s_1'} & \text{if } M \text{ even} \end{cases} \tag{1.56}$$

where we used the convention, that equal upper and lower indices are summed out. The dimension of the T_M is given by $n^4 \cdot \tilde{m}^4$.

To save computer memory, the environment block E has *not* to be stored explicitly. Due to the symmetry of the local plaquettes τ, E can be constructed from S by a "180 degree rotation"

$$E_{s_2 n_{\mathrm{e}} s_1}^{s_1' n_{\mathrm{s}}' s_2'} = S_{s_1' n_{\mathrm{e}}' s_2'}^{s_1 n_{\mathrm{e}} s_2}, \quad . \tag{1.57}$$

2. Compute the leading left and right eigenvector

$$\left| \Lambda_0^{L/R} \right\rangle = \left(\Lambda_{s_1 n_{\mathrm{s}} s_2 n_{\mathrm{e}}}^{L/R} \right) \tag{1.58}$$

of the QTM T_M. Calculate the required thermodynamic properties (e.g. the free energy), which are determined by Λ_0 only. Local expectation values $\langle O \rangle$ are obtained by constructing the modified QTM $T_M(O)$ (cf. eq. (1.47)). This is realized by manipulating the system block in the following way:

$$S_O{}_{s_1 n_{\mathrm{s}} s_2}^{\tilde{s}_1 n_{\mathrm{s}}' \tilde{s}_2'} = \begin{cases} S_{\tilde{s} n_{\mathrm{s}} s_2}^{\tilde{s}' n_{\mathrm{s}}' \tilde{s}_2} \cdot O_{\tilde{s}' \tilde{s}_1}^{\tilde{s} s_1} & \text{if } M \text{ odd} \\[2mm] S_{\tilde{s} n_{\mathrm{s}} \tilde{s}_2}^{\tilde{s}' n_{\mathrm{s}}' \tilde{s}_2'} \cdot O_{\tilde{s}' \tilde{s}_1}^{\tilde{s} s_1} & \text{if } M \text{ even} \end{cases} \tag{1.59}$$
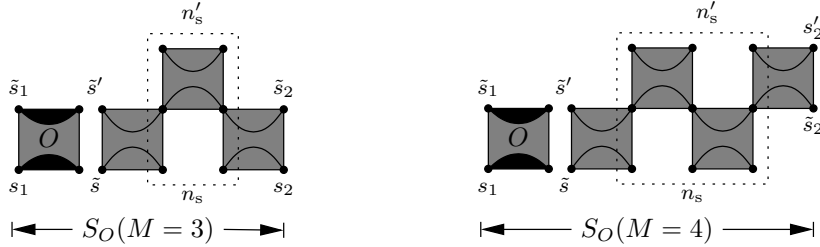

Figure 1.8.: Modified system block S_O.

If correlation lengths are of interest, not only the leading, but also the next leading eigenvalues have to be computed.

3. Construct the reduced density-matrix $\rho = \mathrm{tr}' \left| \Lambda_0^R \right\rangle \left\langle \Lambda_0^L \right|$, i.e.

$$\rho_{\tilde{n}_{\mathrm{s}}}^{\tilde{n}_{\mathrm{s}}'} = \sum_{s_2 n_{\mathrm{e}}} \Lambda_{s_1' n_{\mathrm{s}}' s_2 n_{\mathrm{e}}}^{R} \Lambda_{s_1 n_{\mathrm{s}} s_2 n_{\mathrm{e}}}^{L} , \tag{1.60}$$

where $\tilde{n}_s = n_s \otimes s$ and $\tilde{n}_s' = n_s' \otimes s'$. Thus, ρ has the dimension $n^2 \cdot \tilde{m}^2$.

Note, that in contrast to the "standard" DMRG algorithm of sec. 1.1, the density-matrix is *not* symmetric. However, the matrix is semi-positive, which can be rigorously proved only in a few special cases. BURSILL et al. [6] have also tested symmetric versions of the density-matrix. But other variants do not provide a correct projection onto the ground state $\left| \Lambda_0^{L/R} \right\rangle$. Thus, the algorithm only works properly in the asymmetric case.

4. Diagonalize ρ. Use the m leading eigenvectors of the spectrum to construct left and right projectors V and U, respectively. The variable $m < \tilde{m} \cdot n$ labels the number of retained states of the DMRG algorithm, cf. sec. 1.1. Note, that the leading right eigenvectors of ρ appear as columns of U, whereas the left ones are the rows of V. U and V therefore have the dimension $m \cdot \tilde{m} \cdot n$.

5. Enlarge the system $\tilde{S} = S \cdot \tau_{M+1,M+2}$ by one plaquette τ, which reads

$$
\tilde{S}^{s'_1 \tilde{n}'_\mathrm{s} s'_2}_{s_1 \tilde{n}_\mathrm{s} s_2} =
\begin{cases}
S^{s'_1 n'_\mathrm{s} \tilde{s}}_{s_1 n_\mathrm{s} s} \tau^{s' s'_2}_{\tilde{s} s_2} & \text{if } M \text{ odd} \\
S^{s'_1 n'_\mathrm{s} s'}_{s_1 n_\mathrm{s} \tilde{s}} \tau^{\tilde{s} s'_2}_{s s_2} & \text{if } M \text{ even}
\end{cases}
\tag{1.61}
$$

where again $\tilde{n}_s = n_s \otimes s$ and $\tilde{n}'_s = n'_s \otimes s'$. The tensor $\tilde{S}$ exhibits the large dimension $n^6 \cdot \tilde{m}^2$.
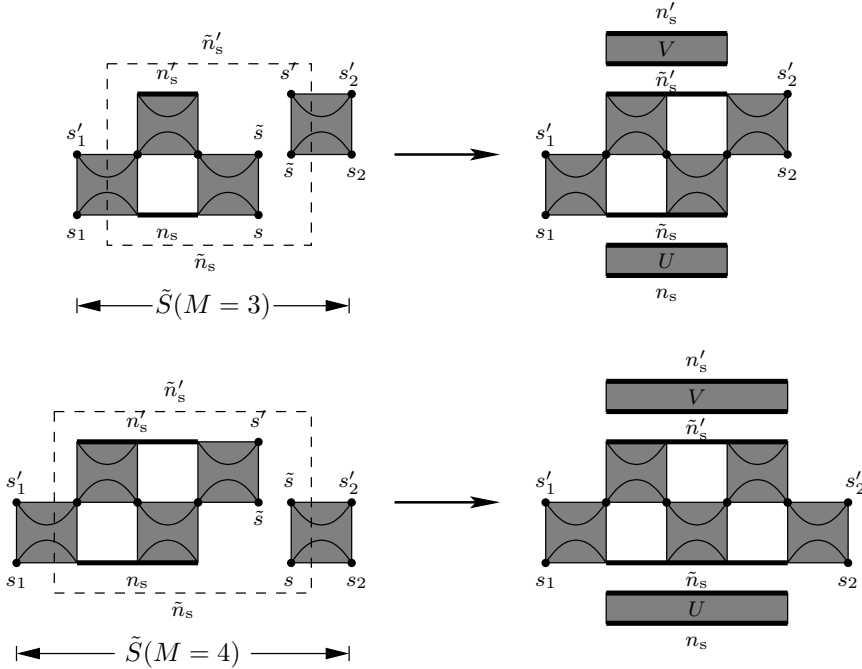

Figure 1.9.: Enlargement of $S \to \tilde{S}$ and renormalization of the system block.

Use the projectors U and V to renormalize $\tilde{S}$

$$
S^{s'_1 n_\mathrm{s} s'_2}_{s_1 n_\mathrm{s} s_2} = U^{n_\mathrm{s}}_{\tilde{n}'_\mathrm{s}} \cdot \tilde{S}^{s'_1 \tilde{n}'_\mathrm{s} s'_2}_{s_1 \tilde{n}_\mathrm{s} s_2} \cdot V^{\tilde{n}_\mathrm{s}}_{n_\mathrm{s}}
\tag{1.62}
$$

which is pictorially shown in fig. 1.9. The dimension of S thereby shrinks to $n^4 \cdot m^2$.

6. Continue from step 2, replacing $\tilde{m}$ by m.

New TMRG Algorithm

Alternatively, one can implement a TMRG algorithm using the new QTM shown in fig. 1.6. Similarly, odd and even renormalization steps have also to be distinguished. We do not present the algorithm in full detail, but rather focus on the main differences, exemplified by the case $M = 3$:

1. System and environment block

$$\left(S_{sn_s}^{s'n'_s}\right) \quad \text{and} \quad \left(E_{sn_e}^{s'n'_e}\right) , \qquad (1.63)$$

which are shown in fig. 1.10, each have the dimension $n^2 \cdot \tilde{m}^2$. The environment block E is obtained by simply *mirroring* S

$$S_{sn_s}^{s'n'_s} = E_{s'n_s}^{sn'_s} \qquad (1.64)$$

Whereas the "180 degree rotation" of the traditional algorithm necessitates parity conservation of $h_{i,i+1}$, the symmetry of E and S given here persist even for $h_{i,i+1} \neq h_{i+1,i}$.
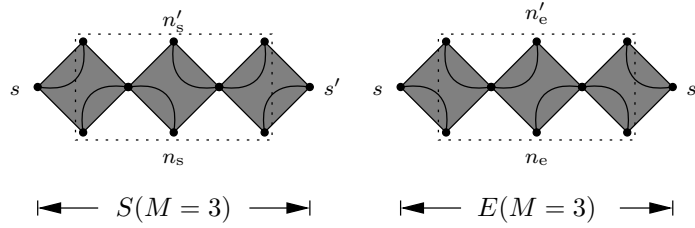

Figure 1.10.: System and environment block of the new TMRG algorithm

2. Calculate the QTM and the leading eigenvalue(s) Λ_0 ($\Lambda_1, \Lambda_2, \dots$), which determine the thermodynamics.

3. In contrast to the traditional TMRG algorithm, the system (and environment) block have *first* to be enlarged

$$\tilde{S}_{sn_s s_1}^{s's'_1 n'_s} = S_{sn_s}^{\tilde{s}n'_s} \cdot \tau_{\tilde{s}s_1}^{s's'_1} , \qquad (1.65)$$

which is depicted in fig. 1.11. The dimension of $\tilde{S}$ is $n^2 \cdot \tilde{m}^2$, which is n^2 times smaller than in the traditional algorithm.

4. After having enlarged the system block, calculate the reduced density matrix, construct the projectors U and V and renormalize $\tilde{S} \rightarrow S$. These steps are completely analogous to the traditional algorithm. Then continue from step 2.
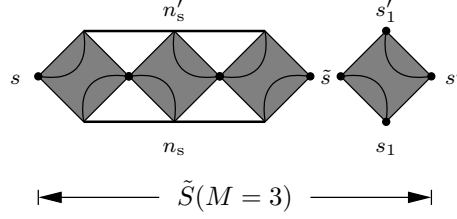
Figure 1.11.: Enlargement of the system block $S \to \tilde{S}$.

The principle structure of both TMRG methods presented here looks rather simple. But the concrete realization of an algorithm on a computer necessitates some technical knowledge to save the demands of memory and increase the algorithm's performance. Some of these technical details are briefly sketched in the following section.

1.2.3. Technical Remarks

The TMRG program principally needs *two types* of functionality. First, it has to deal with vectors, matrices and tensors in a very efficient manner, so that sufficiently fast routines for their storage, access and multiplication have to be programmed. Secondly, we need stable *asymmetric* diagonalization methods for the density-matrix and the QTM, which is the numerically sophisticated part. The most important way to save computer performance in both matters is to take advantage of locally *conserved quantities*. Assume an arbitrary additive local quantum number s, e.g. the spin. Then, the matrix elements $\langle s'_i s'_{i+1} | h_{i,i+1} | s_i s_{i+1} \rangle$ are non-vanishing only for $s_i + s_{i+1} = s'_i + s'_{i+1}$ The conservation law for $h_{i,i+1}$ corresponds to the following counter part for the local plaquette

$$
\tau_{s_1 s_2}^{s'_1 s'_2} = \quad \begin{matrix} s'_2 & s_2 \\ & \\ s'_1 & s_1 \end{matrix} \quad : \quad s'_1 + s_1 = s'_2 + s_2 \implies s'_1 - s'_2 = s_2 - s_1 \; . \qquad (1.66)
$$

Using the notation of eq. (1.35) for T_M eq. (1.66) leads the conservation number

$$
\mathcal{C} = \sum_{j=1}^{2M} (-1)^i s_j^i = \sum_{j=1}^{2M} (-1)^i s_j^{i+2} \qquad (1.67)
$$

of the QTM. All other tensors (e.g. the system block S, $\tilde{S}$) used in the algorithm similarly decompose into blocks. A large number of tensor elements therefore vanish and do not have to be taken into account in the algorithm. Thus, the consumption of storage memory and computing time is *drastically* reduced.

Moreover, we can explicitly locate the T_M-block of the largest eigenvector $\left| \Lambda_0^{L/R} \right\rangle$. The argument for that starts from the high temperature limit $T \to \infty$, where the local plaquettes τ become unity (cf. eq. (1.38))

$$
\tau_{s_2 s'_2}^{s_1 s'_1} = \delta_{s_1, s'_1} \delta_{s_2, s'_2} \; . \qquad (1.68)
$$

Therefore, the only non-vanishing (right) block of T_M obeys

$$s_{2k}^{i+2} = s_{2k+1}^{i+2} \quad k = 1, \ldots, M \ . \tag{1.69}$$

and hence $\mathcal{C} = 0$. As no "level crossing" of Λ_0 with other parts of the spectrum is possible (cf. the arguments given in sec. 1.2.1), $\mathcal{C} = 0$ for $\left|\Lambda_0^{L/R}\right\rangle$ persists at *any* temperatures $T > 0$. As a performance effect for the TMRG program, we consequently have to consider only *one* subspace of T_M. However, other blocks get relevant, if correlation lengths are of interest.

Even if the utilization of conserved numbers reduces the computational efforts considerably, a highly time consuming part of the algorithm is found in the computation of $\left|\Lambda_0^R\right\rangle$ and $\left\langle\Lambda_0^L\right|$. Fortunately, the left eigenvector $\left|\Lambda_0^L\right\rangle$ can be constructed from $\left|\Lambda_0^R\right\rangle$ by

$$\Lambda_0^L{}_{s_1 n_s s_2 n_e} = \Lambda_0^R{}_{s_1 n_e s_2 n_s} \ , \tag{1.70}$$

which is already suggestive from the high temperature limit in fig. 1.5.

Note, that a complete diagonalization of T_M is senseless, as we are only interested in one (some) leading eigenvalues. A typical strategy to calculate the *largest* eigenvector is the *power method*, which uses the property that multiple powers of T_M acting on a random vector $\left|\psi\right\rangle$ yields

$$(T_M)^k\left|\psi\right\rangle = \sum_\mu a_\mu \Lambda_\mu^k\left|\Lambda_\mu^R\right\rangle \xrightarrow{k\to\infty} \Lambda_0^k a_0\left|\Lambda_0^R\right\rangle \ , \tag{1.71}$$

where $a_\mu = \left\langle\psi|\Lambda_\mu^R\right\rangle$. The power method is not a good choice if one is interested in the next leading eigenvalues as well. Fortunately, smart algorithms have been developed to calculate the leading eigenspectrum of a matrix. We used a combination of the Lanczos [36] and Arnoldi [40] method, which is available by the ARPACK package [41] also for non-symmetric matrices. The procedure of finding $\left|\Lambda_0^{L/R}\right\rangle$ is by far the most time consuming part in the TMRG program. It is important to notice, that the quantum transfer-matrix T_M does not have to be constructed and stored explicitly. Since T_M has a dimension of the order $m^4 \cdot n^4$ (in the traditional TMRG), this induces a noticeable consumption of computer memory. Fortunately, the only information which is necessary for the ARPACK (or power method) is the action of T_M onto a vector. This can be realized by first acting with the system block S onto the vector, storing the intermediate result, and then acting with the environment block E on it.

Another crucial point is the *complete* diagonalization of the DM ρ, which is not a question of computational efforts in time, but of *precision*. It is well known, that the high precision numerical diagonalization of non-symmetric matrices is a difficult matter and still a field of intense research. We used the DGEMV routine available by the LAPACK [42] package. Note, that right and left eigenbasis have to satisfy the orthonormality relation

$$\left\langle\Lambda_\alpha^L|\Lambda_\beta^R\right\rangle = \delta_{\alpha\beta} \ . \tag{1.72}$$

The list of numerical details is by far not exhaustive, but contains only a brief summary of the basic concepts of saving computational efforts in the TMRG algorithm.

The "new" TMRG algorithm shown in fig. 1.6 produces results of a slightly worse accuracy. The crucial difference is that the construction of $\left|\Lambda_0^L\right\rangle$ from $\left|\Lambda_0^R\right\rangle$ in eq. (1.70) fails here and thus $\left|\Lambda_0^L\right\rangle$ has to be calculated explicitly. Therefore, the computational time consumption is nearly doubled and also the orthonormalization procedure in eq. (1.72) is less accurate. Research of improving the numerical accuracy of the "new" algorithm is in progress [43]. We basically used the new algorithm to calculate the precise value of k_α.

2. Extended Hubbard Models

2.1. Introduction

When do strongly correlated electrons play a role in solid state physics?
It is well known that the physics of magnetism and conductivity of a solid
are determined by the electrons of the outer orbitals. In the crystal structure
these orbitals overlap and build electron bands [44]. Therefore it is one of the
main topics of solid state physics to study phenomena of many-particle fermion
systems.
In good metals electrons can move almost freely in the conduction band. In
an ideal case, the physics of such a many-particle problem is described by a
three dimensional free Fermi gas. This is the most simple model for electrons,
where the eigenstates are (tensor) products of one-particle waves $|\mathbf{k}\rangle \sim \mathrm{e}^{\mathrm{i}\mathbf{k}\mathbf{r}}$
with momentum $\mathbf{k}$ and energy dispersion

$$\epsilon(\mathbf{k}) = \frac{\mathbf{k}^2}{2m} \ . \tag{2.1}$$

The Fermi gas ground state is the well known Fermi sea, where all states
$|\mathbf{k}| \leq k_F$ up to the Fermi wave vector k_F are filled, all others are empty. The
momentum distribution of states

$$n_\sigma(\mathbf{k}) = \left\langle c_{\mathbf{k}\sigma}^\dagger c_{\mathbf{k}\sigma} \right\rangle = \begin{cases} 1 & |\mathbf{k}| \leq k_F \\ 0 & |\mathbf{k}| > k_F \end{cases} \tag{2.2}$$

is plotted in fig. 2.1 (a) for the temperature $T = 0$, showing a discontinuity at
the Fermi surface ϵ_F.
If the electrons *interact*, collective effects play a role and the terminology which
is used is that of a *Fermi liquid*. For *weak* interactions the fundamental idea
of the Landau's Fermi liquid theory [45, 46, 47] is to model such interacting
systems by a "non-interacting" one. This is in fact possible, because the weak
interaction does not principally destroy the Fermi surface. The shape of $n_\sigma(\mathbf{k})$
changes as shown in fig. 2.1 (b), but in principal the discontinuity persists.
The discontinuity expresses the existence of quasi-particles excitations close
to the Fermi surface. In other words: the weakly *interacting* fermion system
resembles a *non interacting* one in the sense that the low-energy excitations
look like non-interacting fermion quasi-particles with a renormalized dispersion
energy $\tilde{\epsilon}(\mathbf{k})$. On a microscopic level this argument gets even more transparent in
terms of Green's functions, which are discussed in section 2.2.1. An important
hypothesis of Landau's theory is that the interaction does not lead to any form
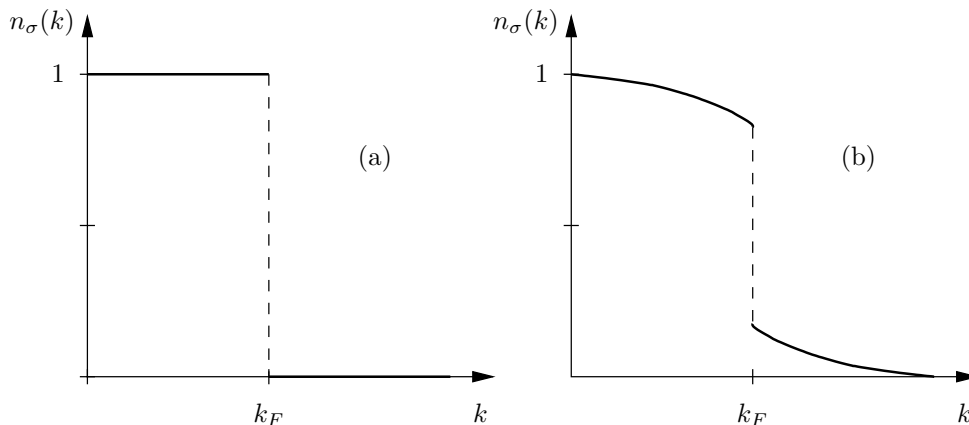
Figure 2.1.: The figure shows a qualitative plot of the density distribution $n_\sigma(\mathbf{k})$ of a (a) free and (b) weak interacting fermion system in momentum space for temperature $T = 0$. The discontinuity expresses the existence of quasi particles close to the Fermi surface.

of symmetry breaking and phase transition, which occurs i.e. in the BCS theory [48] of superconductivity.

If the interaction gets strong, the correlations between the electrons increase and highly collective effects start to dominate the physics. In such a case the Fermi liquid theory collapses. This e.g. happens if the width of the conduction band gets small (like in transition metals) and the Coulomb interactions are highly relevant.

A first step is to work out a microscopic Hamiltonian for such *strongly correlated* systems. This was proposed independently by HUBBARD [10], GUTZWILLER [9] and KANAMORI [11] in 1963 in terms of a *tight-binding* Hamiltonian, which we present now.

The starting point is a Hamiltonian $\mathcal{H}$ (in second quantization) of Coulomb interacting fermions in the crystal structure of a solid

$$
\begin{aligned}
\mathcal{H} = & \sum_\sigma \int \mathrm{d}^3r \; \psi_\sigma^\dagger(\mathbf{r}) \left(-\frac{\hbar^2}{2m}\nabla^2 + U_{\mathrm{ion}}(\mathbf{r}) \right) \psi_\sigma(\mathbf{r}) \\
& + \sum_{\sigma\sigma'} \int \mathrm{d}^3r \int \mathrm{d}^3r' \; \psi_\sigma^\dagger(\mathbf{r})\psi_{\sigma'}^\dagger(\mathbf{r}')V_{ee}(\mathbf{r}-\mathbf{r}')\psi_{\sigma'}(\mathbf{r}')\psi_\sigma(\mathbf{r}) \; .
\end{aligned}
\tag{2.3}
$$

$U_{\mathrm{ion}}(\mathbf{r})$ labels the periodical potential of the atom ions and

$$
V_{ee}(\mathbf{r}) \propto \frac{1}{|\mathbf{r}|}
\tag{2.4}
$$

is the repulsive Coulomb potential. According to BLOCH'S theorem the potential U_{ion} splits up the dispersion of electrons into infinitely many energy bands α. The electron wave functions of the bands are called Bloch functions $u_{\mathbf{k}\alpha}$ and form a complete Hilbert space basis.

As the physically relevant energy bands α were supposed to be small, the electrons can not move freely through the band, but localize according to the atom core geometry. Therefore, it is useful to transform the Hamiltonian (2.3) into a (localized) WANNIER basis,

$$\left|i\alpha\right\rangle := \phi_{i\alpha}(\mathbf{r}) = \frac{1}{\sqrt{L}} \sum_{\mathbf{k}} e^{-i\mathbf{k}\mathbf{R}_i} u_{\mathbf{k}\alpha}(\mathbf{r}) \ , \tag{2.5}$$

where $\mathbf{R}_i$ labels the sites of the atom ions. The Hamiltonian (2.3) in Wannier basis transforms to

$$\mathcal{H} = \sum_{ij\alpha\sigma} t_{ij}^{\alpha} c_{i\alpha\sigma}^{\dagger} c_{j\alpha\sigma} + \sum_{ijmn} \sum_{\alpha\beta\mu\nu} \sum_{\sigma\tau} v_{ijmn}^{\alpha\beta\sigma\tau} c_{i\alpha\sigma}^{\dagger} c_{j\beta\tau}^{\dagger} c_{n\nu\tau} c_{m\mu\sigma} \ . \tag{2.6}$$

where $c_{i\alpha\sigma}^{\dagger}$ creates an electron with spin σ in the unit cell i and respective band α. The coefficients are given by the matrix elements of the kinetic part

$$t_{ij}^{\alpha} = \left\langle i\alpha \left| \frac{-\hbar^2}{2m} \nabla^2 + U_{\text{ion}}(\mathbf{r}) \right| j\alpha \right\rangle \tag{2.7}$$

and the Coulomb potential

$$v_{ijmn}^{\alpha\beta\mu\nu} = \left\langle i\alpha, j\beta \left| V_{ee}(\mathbf{r} - \mathbf{r}') \right| m\mu, n\nu \right\rangle \ . \tag{2.8}$$

HUBBARD proposed a number of assumptions to simplify the Hamilton operator (2.6):

1. The energy bands α do not overlap and thus the physics are determined by intra band interactions only. Apart from that, it is assumed that only one band is physically relevant, thus the indices α and β are completely omitted.

2. The model is translationally invariant, therefore the coefficients $t_{ij} = t_{|i-j|}^{\alpha}$ and $v_{ijmn} = v_{|i-j||m-n|}$ only depend on the distance of unit cells.

3. The Coulomb interaction is of short range due to screening effects of the atom ions. Thus, only next-neighbor interactions $\langle ij \rangle$ are taken into account.

This approximation is also called the *tight-binding approximation* of the fermion system. Using the simplifications, the *tight-binding* Hamiltonian reads

$$\begin{aligned} \mathcal{H} &= -t \sum_{\langle ij \rangle \sigma} c_{i\sigma}^{\dagger} c_{j\sigma} + U \sum_{i} n_{i\uparrow} n_{i\downarrow} + V \sum_{\langle ij \rangle} n_i n_j + J \sum_{\langle ij \rangle} \mathbf{S}_i \mathbf{S}_j \\ &\quad + X \sum_{\langle ij \rangle \sigma} c_{i\sigma}^{\dagger} c_{j\sigma} \left(n_{i\bar{\sigma}} + n_{j\bar{\sigma}} \right) + Y \sum_{\langle ij \rangle} c_{i\uparrow}^{\dagger} c_{i\downarrow}^{\dagger} c_{j\downarrow} c_{j\uparrow} \end{aligned} \tag{2.9}$$

which is known as the *generalized Hubbard model*. In eq. (2.9) the following abbreviations

$$\begin{aligned} t &= -t_{ij}, & U &= v_{iiii}, & X &= v_{iiij} \\ V &= v_{ijij}, & J &= -2v_{ijji}, & Y &= v_{iijj} \ . \end{aligned} \tag{2.10}$$

and operators

$$n_{j\sigma} = c^\dagger_{j\sigma} c_{j\sigma}, \quad n_j = n_{j\uparrow} + n_{j\downarrow}, \quad 2\mathbf{S}_i = \sum_{\sigma\tau} c^\dagger_{i\sigma} \mathcal{S}_{\sigma\tau} c_{i\tau} \qquad (2.11)$$

are used, where $\mathcal{S} = (\mathcal{S}^x, \mathcal{S}^y, \mathcal{S}^z)$ is a vector which consists of the usual Pauli matrices $\mathcal{S}^i$.

The short-range Coulomb potential obviously leads to five different types of local interactions U, V, J, X and Y. Two of them are *diagonal*: the on-site and next-neighbor Coulomb interaction U and V. The *off-diagonal* couplings are the spin exchange J, the so-called bond-charge interaction X and the pair hopping Y.

HUBBARD roughly estimated the energies of these parameters for $3d$ transition metals [10]

$$U \approx 20\,\text{eV} > V \approx 2 - 3\,\text{eV} > t \approx 1\,\text{eV} > X \approx 0.5\,\text{eV} \gg J, Y . \qquad (2.12)$$

In a first approximation he therefore considered only the *on-site* term of the Coulomb potential, which is known as the *standard Hubbard model* or just *Hubbard model*

$$\mathcal{H}_{\text{Hub}} = -t \sum_{\langle ij\rangle\sigma} c^\dagger_{i\sigma} c_{j\sigma} + U \sum_i n_{i\uparrow} n_{i\downarrow} . \qquad (2.13)$$

The Hamilton $\mathcal{H}_{\text{Hub}}$ is obviously not trivial to solve, because the kinetic term is diagonal in momentum space, whereas the Coulomb part is diagonal in real space.

Even if in the context of high-temperature superconductivity *two-dimensional* Hubbard models are relevant, it is very constructive to consider the one dimensional counterparts. On the one hand, analytical and numerical tools are much more elaborated in one dimension, e.g. the BETHE ansatz or the numerical DMRG approach. On the other hand, the effects of strong correlations are often similar, since quantum fluctuations in 1D are even stronger than in 2D.

In *one dimension* the Hubbard model is integrable, which has been shown by LIEB and WU by means of the (nested) BETHE ansatz [49]. Various studies followed, ranging from zero temperature properties to studies of the elementary excitations [50, 51, 52, 53], magnetic properties [54], correlation functions [55] to symmetries [56, 57, 58]. Apart from zero temperature properties, also the thermodynamics of the Hubbard model has been calculated analytically [59, 38]. In the last years, extensions of the Hubbard model were intensively discussed, which add one (or more) of the neglected Coulomb terms given above to the Hubbard Hamiltonian and are therefore called *extended* Hubbard models. Even if these additional terms are smaller than U in practice, they can change the physics due to e.g. the breaking of particle-hole symmetry. As mentioned in the preface, also quasi-dimensional organic superconductors like the BECHGAARD salts [13] are known, where the standard Hubbard model does not seem to be a minimal model.

The present work concentrates on the influence of the additional bond-charge interaction X, which we refer to as the Hirsch model. As mentioned in the preface, HIRSCH showed that the model exhibits (hole) superconductivity [14, 15].

In section 2.3 we summarize the actual state of research concerning the Hirsch model. But first we step into some general details of one-dimensional quantum liquid theory, which are important to understand the physics of interacting 1D Fermi systems.

2.2. Quantum Liquids in One Dimension

2.2.1. The Collapse of Fermi Liquid Theory

In the last section we already pointed out, that an integral part of the Landau's Fermi liquid theory is the existence of quasi particle excitations close to the Fermi surface. Interactions between the electrons therefore have to be weak to prevent the destruction of the Fermi surface.

We expand the discussion to a microscopic level, following [60]. In terms of the Green's functions theory it gets even more evident when excitations have particle character and in which case the particle picture collapses. Our starting point is the thermodynamic Green's function in momentum space

$$G(\mathbf{k}, \tau) = - \left\langle \mathcal{T} c_{\mathbf{k}}(\tau) c_{\mathbf{k}}^{\dagger}(0) \right\rangle \ , \qquad (2.14)$$

where τ is the usual (MATSUBARA) imaginary time and $\mathcal{T}$ is the time ordering operator. For simplicity, we omit the spin degree of freedom.

The Green's function formalism provides a powerful tool to derive several quantities from the Green's function itself. As an example the momentum distribution $n(\mathbf{k})$ (which was shown in fig. 2.1) reads

$$n(\mathbf{k}) = G(\mathbf{k}, \tau)\big|_{\tau \to -\delta} \ . \qquad (2.15)$$

An important quantity is also the spectral density

$$A(\mathbf{k}, \omega) = -\frac{1}{\pi} \mathrm{Im}\, \tilde{G}(\mathbf{k}, \mathrm{i}\omega)\big|_{\mathrm{i}\omega \to \omega + \mathrm{i}\delta} \ . \qquad (2.16)$$

where $\tilde{G}(\mathbf{k}, z)$ is the Fourier transformed of $G(\mathbf{k}, \tau)$. $A(\mathbf{k}, \omega)$ measures the distribution of particles in the energy-momentum space. Using $A(\mathbf{k}, \omega)$ eq. (2.15) can alternatively be written as

$$n(\mathbf{k}) = \int \mathrm{d}\omega f(\omega) A(\mathbf{k}, \omega) \ , \quad \text{where} \quad f(\omega) = \frac{1}{\mathrm{e}^{\beta \omega} + 1} \ . \qquad (2.17)$$

In the three-dimensional free fermion gas we have a quasi-particle nature of excitations. The Green's function then reads

$$\tilde{G}_0(\mathbf{k}, \omega) = \frac{1}{\mathrm{i}\omega - \epsilon(\mathbf{k})} \qquad (2.18)$$

which has *a pole* on the imaginary axis. The pole expresses the fact that excitations have the character of quasi-particles. This is even more apparent by the spectral density $A(\mathbf{k}, \omega)$ which turns to a delta peak $A(\mathbf{k}, \omega) = \delta(w - \epsilon(\mathbf{k}))$ and thus identifies quasi particles with a well defined dispersion $\omega = \epsilon(\mathbf{k})$.

In the case of coupled electrons, the interactions enter the Green's function by a so-called self energy correction $\Sigma(\mathbf{k}, \omega)$:

$$\tilde{G}(\mathbf{k}, \omega) = \frac{1}{i\omega - \epsilon(\mathbf{k}) - \Sigma(\mathbf{k}, \omega)} \ . \tag{2.19}$$

The Landau assumption of quasi-particles is equivalent to a regularity of $\Sigma(k, \omega)$ close to the Fermi surface, such that a diagrammatic perturbation expansion is possible. If $\Sigma(\mathbf{k}, \omega)$ is regular, the Green's function can be written in first order perturbation as

$$\tilde{G}(\mathbf{k}, \omega) = \frac{Z}{i\omega - \tilde{\epsilon}(\mathbf{k})} \ . \tag{2.20}$$

The first order terms of $\Sigma(\mathbf{k}, \omega)$ thus lead only to a renormalization of the dispersion $\tilde{\epsilon}(\mathbf{k})$ of quasi-particles and a normalization factor Z. Collective effects appear only in higher orders of the perturbation approach, leading to an *incoherent* background of many particle excitation processes. Speaking in terms of the spectral density $A(\mathbf{k}, \omega)$ the delta peak qualitatively persists, but is broadened by the incoherent background. Due to eq.(2.17) it is obvious, that the discontinuity of the momentum distribution $n(\mathbf{k})$ also persists.

The Green's function theory facilitates now a deeper understanding to the nature of Fermi liquids and the appearance of quasi-particles. The Fermi liquid behavior collapses, if the incoherent background increases and destroys the quasi particle peak in $A(\mathbf{k}, \omega)$. In particular, this manifests itself in a continuous momentum distribution, which is exemplified in fig. 2.2. In such a case, a proper theory *must* include collective effects.
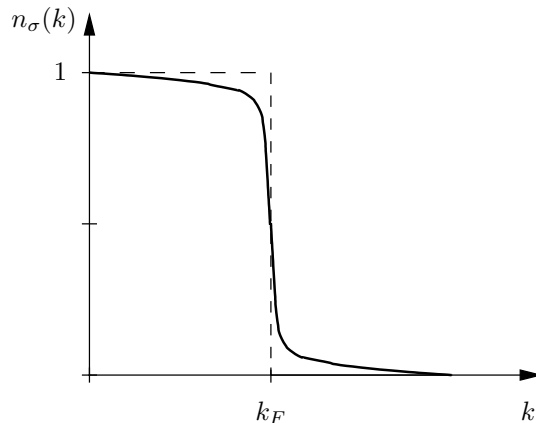

Figure 2.2.: Qualitative plot of the momentum distribution $n_\sigma(\mathbf{k})$, if no quasi-particle discontinuity is apparent at the Fermi level k_F.

Interacting fermion models in one dimension can *never* be described by Fermi liquid theory. That the physics principally differ is already suggestive due to the topology of the Fermi surface, which reduces to two *singular points* $-k_F$ and k_F. In a Fermi liquid description low-energy excitations carrying the momentum $0 < k < 2k_F$ would not be possible. Calculating the Green's functions, one would

find that the self energy part $\Sigma(\mathbf{k}, \omega)$ is indeed not regular and destroys the pole structure of G close to the Fermi surface. Thus, the low energy excitations do not have any particle nature, but are of pure collective type, namely long wave-length fluctuations of the electron density.

2.2.2. Tomonaga-Luttinger and Luther-Emery Liquids

In the late seventies, HALDANE [61, 62, 63] pointed out the relevance of the TOMONAGA-LUTTINGER model (TL) [64, 65] for the physics of strongly correlated electrons *in one dimension*. The basis of the TL theory is provided by a bosonisation approach of the low-energy excitations which we briefly outline in this section.

We start with the (tight-binding) Hamiltonian of free spinless fermions

$$H = -t \sum_{\langle ij \rangle} c_i^\dagger c_j = -2t \sum_k \cos(k) c_k^\dagger c_k \ , \tag{2.21}$$

which is diagonal in momentum space. Fermions with spin are discussed later on.

The basic idea of bosonisation is to linearize the low-energy excitation spectrum at the Fermi points $\pm k_F$, which is visualized in fig. 2.3. The intention is to
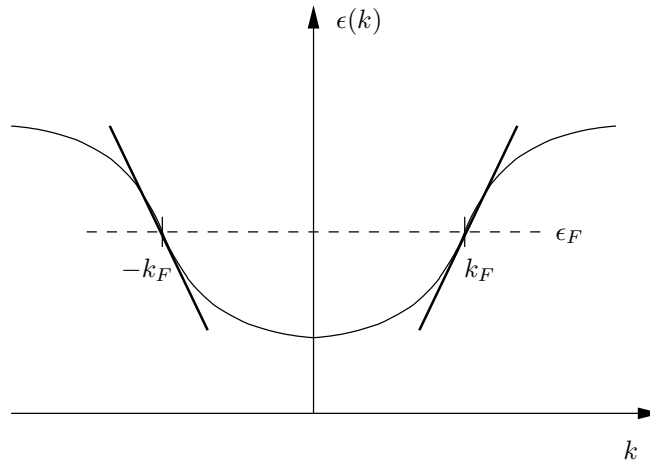

Figure 2.3.: Linearization of the free fermion dispersion $\epsilon(k) = 2t \cos(k)$ at the Fermi points $\pm k_F$.

describe the excitations as "sound waves" of *bosons* due to the linear dispersion. It is now important to differ between the left and right Fermi point excitations, which we denote by (fermion operators) $c_{k,+}$ and $c_{k,-}$, respectively.

The "linearized Hamiltonian" of excitations reads

$$H = H_0 + H_{\text{int}} \ , \tag{2.22}$$

where H_0 is the part, where excitations of right and left side $\pm k_F$ do not interact:

$$H_0 = v_F \left(\sum_k (k - k_F) c_{k,+}^\dagger c_{k,+} + (-k - k_F) c_{k,-}^\dagger c_{k,-} \right) \tag{2.23}$$

$$= \frac{2\pi v_F}{L} \sum_{q>0, \alpha=\pm} \rho_{q,\alpha} \rho_{-q,\alpha} \ . \tag{2.24}$$

Here, $v_F = 2t \sin(k_F)$ labels the Fermi velocity and we have used the Fourier components of the particle density operator

$$\rho_{q,\pm} := \sum_k c_{k+q,\pm}^\dagger c_{k,\pm} \ , \tag{2.25}$$

which obeys Bose type commutator relations

$$\left[\rho_{-q,\alpha}, \rho_{q,\alpha'} \right] = \delta_{\alpha\alpha'} \delta_{q,q'} \frac{\alpha q L}{2\pi} \ . \tag{2.26}$$

In addition, right and left side excitations *interact* and exhibit scattering processes

$$H_{\text{int}} = \frac{1}{2L} \sum_{q, \alpha=\pm} \left(g_2(q) \rho_{q,\alpha} \rho_{-q,-\alpha} + g_4(q) \rho_{q,\alpha} \rho_{-q,\alpha} \right) \ , \tag{2.27}$$

where $g_2(q)$ and $g_4(q)$ label the respective scattering amplitudes.
The Hamiltonian H is known as the Tomonaga-Luttinger (TL) model. It is exactly solvable by diagonalizing H using a BOGOLIUBOV transformation, leading to an energy spectrum

$$\epsilon(q) = |q| \sqrt{\left(v_F + \frac{g_4(q)}{2\pi} \right)^2 - \left(\frac{g_2(q)}{2\pi} \right)^2} \ . \tag{2.28}$$

It is in fact possible now to calculate various physical properties like correlation functions or the one-particle Green's function exactly. To proceed with these calculations, usually bosonic field operators are introduced

$$\phi(x) = -\frac{\mathrm{i}\pi}{L} \sum_{q \neq 0} \frac{1}{q} \mathrm{e}^{-\alpha|q|/2 - \mathrm{i}qx} \left(\rho_{q,+} + \rho_{q,-} \right) - \frac{\pi x}{L} (N_+ + N_-) \ ,$$

$$\Pi(x) = \frac{1}{L} \sum_{q \neq 0} \mathrm{e}^{-\alpha|q|/2 - \mathrm{i}qx} \left(\rho_{q,+} - \rho_{q,-} \right) + \frac{1}{L} (N_+ - N_-) \ , \tag{2.29}$$

where $N_\pm = \rho_{0,\pm}$. They obey canonical boson commutation relations

$$[\phi(x), \Pi(y)] = \mathrm{i}\delta(x - y) \ . \tag{2.30}$$

The definition shows that the bosons implicated by ϕ are created by a superposition of $\rho_{q,\pm}$ and are thus of *highly collective* character. Using eq. (2.29) the Hamiltonian transforms into

$$H = \int \mathrm{d}x \left(\frac{\pi v K}{2} \Pi(x)^2 + \frac{v}{2\pi K} (\partial_x \phi)^2 \right) \tag{2.31}$$

which is nothing else than the Hamiltonian of an *elastic string* and the ultimate result of bosonisation. The parameters v and K are given by

$$v = \sqrt{\left(v_F + \frac{g_4}{2\pi}\right)^2 + \left(\frac{g_2}{2\pi}\right)^2} \; , \quad K = \sqrt{\frac{2\pi v_F + g_4 - g_2}{2\pi v_F + g_4 + g_2}} \; , \tag{2.32}$$

where g_2 and g_4 were assumed to be q-independent. The eigenspectrum of eq. (2.31) now simply reads

$$\epsilon(q) = v \, |q| \; , \tag{2.33}$$

so that v becomes the physical meaning of a velocity of the boson waves. Note, that translational invariance of the model is expressed by $g_2 = g_4$, which yields $Kv = v_F$. Thus, the isotropic TL model is controlled by *one parameter only*.

An important result of the bosonisation approach is that the momentum distribution $n(k)$ is *continuous*

$$n(k) - n(k_F) \propto |k - k_F|^\theta \, \mathrm{sgn}(k - k_F) \quad \text{for } k \approx k_F \; , \tag{2.34}$$

and no quasi particles appear, cf. fig. 2.2.

The TL model can easily be extended, if the fermion operators also carry spin degrees of freedom. The boson fields, that have to be introduced in that case, completely separate into a spin and charge component ϕ_c and ϕ_s. In other words, spin and charge fluctuations evolve independently from each other, which is called *spin-charge separation*. Consequently, two velocities v_c and v_s appear, two spectra $\epsilon_c(q) = |q| \, v_c$ and $\epsilon_s(q) = |q| \, v_s$ of charge (holon) and spin (spinon) excitations and parameters K_c and K_s. In the case of spin rotational invariance, one can explicitly show $K_s = 1$.

The reason why the TL model has become a prototype for *interacting* fermionic models is the success of *renormalization group* techniques. Many *weak* interacting fermion systems show TL-like behavior, which can be seen by the fixed points of the renormalization flow. This led HALDANE [62, 63] to propose the general concept of a Tomonaga-Luttinger liquid (TLL) as a replacement of Fermi liquid theory. Characteristical for a TLL is the non quasi-particle nature of the excitations. Spinon and holon excitations separate and are *both gapless*. The low energy-physics are parameterized by spin and charge velocities v_s and v_c and a parameter K_c, which plays an important role in respect to correlation functions, cf. sec. 2.2.3.

An expansion of the TL model with spin, involving also backscattering processes

$$\sum_{kpq\sigma\tau} g_1 c^\dagger_{k,\sigma,+} c^\dagger_{p,\tau,-} c_{p+2k_F+q,\tau,+} c_{k-2k_F-q,\sigma,-} \tag{2.35}$$

was solved by LUTHER and EMERY [66] (σ and τ label the spins indices). The crucial difference is that here spin excitations exhibit a gap Δ_s and get massive

$$\epsilon_s(q) = \mathrm{sgn}(q)\sqrt{v_s^2 q^2 + \Delta_s} \; . \tag{2.36}$$

The Luther-Emery (LE) model is representative for models which exhibit a spin gap, which are consequently called Luther-Emery liquids (LEL). Due to the spin gap, the low energy excitations are characterized by the charge velocity v_c and K_c only.

2.2.3. Correlation Functions

Due to the gapless excitation spectrum, the TE and LE models are critical at temperature $T = 0$. Criticality means, that correlations get long-ranged in the sense that they exhibit an asymptotic *power-law decay* behavior $r^{-\alpha}$. In contrast, a gapped energy spectrum leads to exponentially decaying $\mathrm{e}^{-r/\xi}$ correlation functions, where the correlation length ξ scales with the gap $\xi \sim 1/\Delta$.

This thesis especially focuses on the following two-point correlation functions:

1. Density-density correlations $\langle n_i n_j \rangle$.

2. Longitudinal spin-spin correlations $\langle S_i^z S_j^z \rangle$, where $S_i^z = (n_{i\uparrow} - n_{i\downarrow})/2$. For SU(2) spin isotropy, the transversal spin-spin correlations are identical to the longitudinal ones.

3. Singlet pair correlations $\langle P_s^\dagger(i) P_s(j) \rangle$, where

$$P_s^\dagger(i) = \frac{1}{\sqrt{2}}(c_{i\uparrow}^\dagger c_{i+1\downarrow}^\dagger - c_{i\downarrow}^\dagger c_{i+1\uparrow}^\dagger) \tag{2.37}$$

   creates a singlet on neighboring sites.

4. Triplet pair correlations $\langle P_{tl}^\dagger(i) P_{tl}(j) \rangle$, where $P_{tl}^\dagger(i)$ creates a triplet on neighboring sites. In case of spin isotropy, the triplet space is threefold degenerate. Thus $P_{tl}^\dagger(i)$ can be one of the operators

$$\begin{aligned}
P_{t1}^\dagger(i) &= c_{i\uparrow}^\dagger c_{i+1\uparrow}^\dagger \ , \\
P_{t2}^\dagger(i) &= c_{i\downarrow}^\dagger c_{i+1\downarrow}^\dagger \ \text{or} \\
P_{t3}^\dagger(i) &= \frac{1}{\sqrt{2}}(c_{i\downarrow}^\dagger c_{i+1\uparrow}^\dagger + c_{i\uparrow}^\dagger c_{i+1\downarrow}^\dagger) \ .
\end{aligned} \tag{2.38}$$

In the research of strongly correlated systems it is a crucial question, which correlations dominate for long distances $r = |i - j|$ and characterize the essential physics. One typically distinguishes the $T = 0$ phases by the leading type of correlations, e.g. charge (spin) density wave phases CDW (SDW) or superconducting phases SP or TP for dominating singlet or triplet correlations. The later ones are not strictly superconducting in the sense that off-diagonal long-range order (ODLRO)

$$\lim_{|i-j|\to\infty} \langle P_{s/t}^\dagger(i) P_{s/t}(j) \rangle \neq 0 \tag{2.39}$$

is included. But nevertheless the pairing of electrons is strongly enhanced due to an *algebraic* decay of the correlation functions at $T = 0$.

Solving the TL model, the asymptotic shape of the correlations can be calculated exactly. One observes (with $r = |i - j|$) [67]:

1. for the density-density correlation

$$\langle n_0 n_r \rangle \sim A_0 r^{-2} + A_1 r^{-(1+K_c)} \cos(2k_F r) + A_2 r^{-4K_c} \cos(4k_F r) \ , \tag{2.40}$$

2. for the spin-spin correlation

$$\langle S_0^z S_r^z \rangle \sim B_0 r^{-2} + B_1 r^{-(1+K_c)} \cos(2k_F r) \ , \qquad (2.41)$$

3. for the singlet-pair correlation

$$\left\langle P_s^\dagger(0) P_s(r) \right\rangle \sim C_0 r^{-(1+\frac{1}{K_c})} + C_1 r^{-(K_c+\frac{1}{K_c})} \cos(2k_F r) \ , \qquad (2.42)$$

4. and for the triplet-pair correlation

$$\left\langle P_t^\dagger(0) P_t(r) \right\rangle \sim D_0 r^{-(1+\frac{1}{K_c})} + D_1 r^{-(K_c+\frac{1}{K_c}+2)} \cos(2k_F r) \ , \qquad (2.43)$$

where A_i, B_i, C_i, D_i are (model dependent) constant coefficients. The critical exponents depend on the parameter K_c only. Each correlation function has a non-oscillating and oscillating parts, which occur as multiples of $2k_F$. Those oscillating parts, which are not explicitly given, decay significantly faster. Note, that strictly speaking also logarithmic terms $\ln^\delta(r)$ additionally appear in the formulas given above. But as one is interested in the asymptotics $r \gg 1$ of the correlations, these so called logarithmic corrections are usually omitted.

The situation changes for the LE liquid. Due to the spin gap, it is found that the spin as well as the triplet correlations are *not* critical and decay exponentially. Critical behavior persist only for the density and singlet correlation, which explicitly reads (up to logarithmic corrections) [67]

1. for the density-density correlation

$$\langle n_0 n_r \rangle \sim A_0 r^{-2} + A_1 r^{-K_c} \cos(2k_F r) + A_2 r^{-4K_c} \cos(4k_F r) \ , \qquad (2.44)$$

2. and for the singlet correlation

$$\left\langle P_s^\dagger(0) P_s(r) \right\rangle \sim C_0 r^{-\frac{1}{K_c}} + C_1 r^{-\left(K_c+\frac{1}{K_c}\right)} \ . \qquad (2.45)$$

From the equations given above we conclude that a TLL as well as the LEL get superconducting for $K_c > 1$. Otherwise density (or spin) correlations dominate. Based on the theory of TLL and LEL we are now able to characterize the physics of the Hirsch model, which is done in the next section.

2.3. The Hirsch Model

2.3.1. Introduction

The Hamilton operator, which we study in this thesis, reads

$$\mathcal{H} = \underbrace{- \sum_{\langle ij \rangle \sigma} c_{i\sigma}^\dagger c_{j\sigma} + X \sum_{\langle ij \rangle \sigma} c_{i\sigma}^\dagger c_{j\sigma}(n_{i\bar\sigma} + n_{j\bar\sigma})}_{\mathcal{H}_X} + \underbrace{U \sum_i n_{i\uparrow} n_{i\downarrow}}_{\mathcal{H}_U} \ , \qquad (2.46)$$

This model was first investigated by HIRSCH [14, 15], therefore we refer to this model as the Hirsch model. (Contrary to [14, 15] we have omitted the next-neighbor Coulomb potential V and we have set $t = 1$). Additionally, we restrict ourselves to the one-dimensional case $d = 1$ and to the ground state properties at $T = 0$.

To give a feeling for the effect of the off-diagonal part $\mathcal{H}_X$, fig. 2.4 visualizes the hopping processes of neighboring lattice sites. The X term obviously contributes, if a spin of opposite site attends the hopping process. Therefore X is called *bond-charge* interaction, the complete Hamiltonian part $\mathcal{H}_X$ is also known as *correlated hopping*. The case of negative (positive) X is referred to as bond-charge attraction (repulsion).
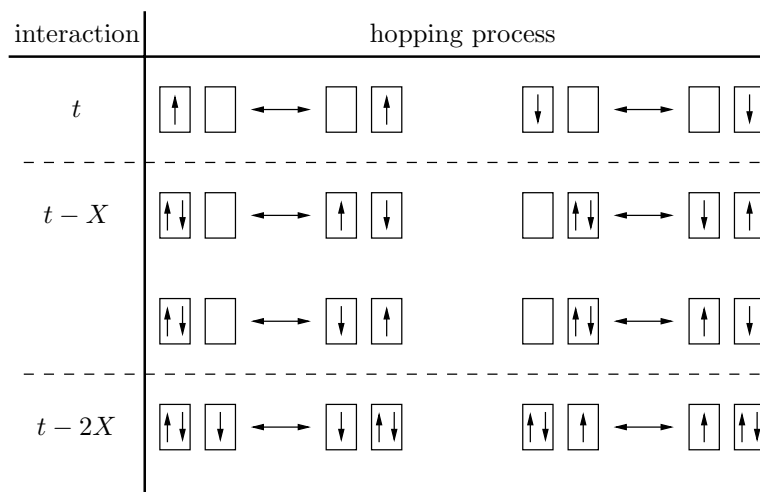
Figure 2.4.: The figure depicts the feasible hopping processes of $\mathcal{H}_X$ and demonstrates the effect of the correlated hopping term $t - X$. As one can see by the pictures, X appears in the energy, if another electron of opposite spin is participating.

The Hirsch model exhibits full $U(1) \otimes SU(2)$ symmetry due to charge and spin conservation, i.e. $\mathcal{H}$ commutes with the total charge $N = \sum_i n_i$ and spin $\mathbf{S} = \sum_i \mathbf{S}_i$. Apart from that, a very useful further symmetry is given by a (modified) particle hole transformation. Replacing particles by holes $c_{i\sigma} \to (-1)^i c_{i\sigma}$, one finds that

$$n' \to 2 - n, \quad X' \to -X/(1 - 2X) \quad \text{and} \quad U' \to U \ , \qquad (2.47)$$

where $n = \langle n_i \rangle$ labels the local density. From eq. (2.47) we conclude that the parameter region $0 \leq X/t \leq 1$ is representative for *all* parameters X: the $0 \leq X \leq 1/2$ region corresponds to $X < 0$, whereas $1/2 \leq X \leq 1$ can be mapped onto $X \geq 1$.

It was the idea of HIRSCH that a repulsive Coulomb potential ($U, X > 0$) can lead to an effective attraction of holes and therefore to hole superconductivity. For weak couplings $X < 1/2$ this can be directly seen from eq. (2.47), where

the repulsive bond-charge interaction $X > 0$ corresponds to an attractive one $X' < 0$ for holes $n' = 2 - n$.

In terms of a BCS-mean-field approach HIRSCH and MARSIGLIO [16, 17, 18] investigated the model in detail. For dimension $d \leq 2$ and a nearly filled band $n \to 2$ they found a phase transition at a critical potential

$$U_c = 4d\frac{2X}{1 - 2X} \left(\frac{2X}{1 - 2X} + 4 \right) \ , \tag{2.48}$$

which is exact for precisely two holes [68]. Beyond the critical $U < U_c$ the authors identified a LEL phase with spin gap and dominant superconducting correlations. For $U > U_c$ the model was found to fall into the universality class of a TLL.

2.3.2. Bosonisation Predictions for $X \ll 1$

An important progress for the understanding of the bond-charge interaction was made by JAPARIDZE and MÜLLER-HARTMANN, who studied the Hirsch model in the framework of bosonisation techniques and renormalization group analysis [69], cf. sec. 2.2.2. The range of applicability of their theory is in principle restricted to the weak coupling regime $X \ll 1$.

They found out that the Hirsch model coincides with the Hubbard model with an *effective* Coulomb potential U_{eff} and hopping amplitude t_{eff}, which depend on the filling

$$U_{\mathrm{eff}} = U + 8X \cos \left(\frac{n\pi}{2} \right) \ ,$$
$$t_{\mathrm{eff}} = 1 - nX \ . \tag{2.49}$$

In order to understand the physics of the Hirsch model it is thus necessary to briefly review some properties of the 1D Hubbard model.
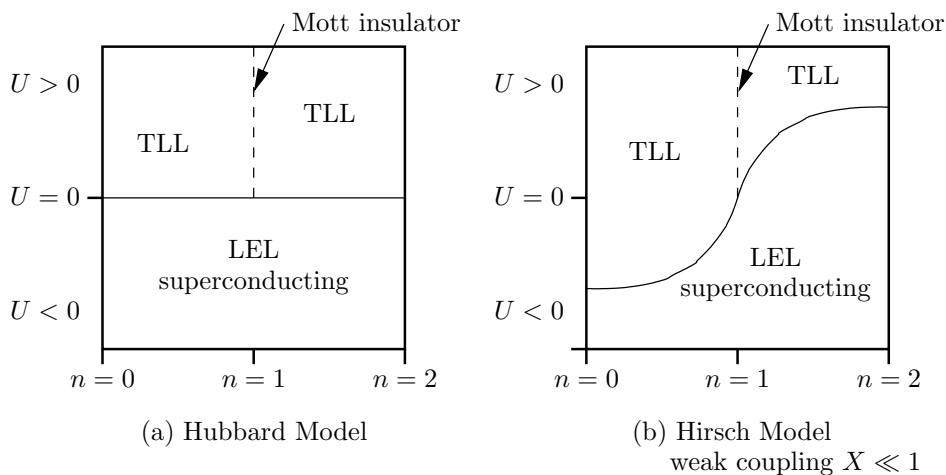

Figure 2.5.: Phase diagram of the (a) Hubbard model and the (b) Hirsch model.

The Hubbard model is exactly solvable by using the Bethe ansatz [49]. The phase diagram is shown in fig. 2.5 (a). In the repulsive regime $U/t > 0$ and away from half filling $n \neq 1$, spin and charge excitations are gapless and the Hubbard model falls into the TLL universality class. An exception is the case of half filling. Here a charge gap opens and the Hubbard model is a MOTT insulator. The attractive regime $U/t < 0$ contrarily falls into the universality class of the LEL, showing a spin gap for arbitrary U.

For attractive $U/t < 0$ it is also found [70] that $K_c > 1$. As a consequence, the attractive Hubbard model is a singlet superconductor in the sense that the singlet pair correlations dominate, cf. sec. 2.2.3. Conversely, $K_c < 1$ holds for the repulsive case $U/t > 0$ [71], so that here density/spin correlations asymptotically dominate.

From the weak coupling correspondence of Hirsch and Hubbard model, the phase diagram of the Hirsch model can be constructed. For $U_{\text{eff}} = 0$ we obtain a phase transition from a TLL to a (superconducting) LEL, in analogy to the Hubbard model. Thus, the phase boundary is given by

$$U_c(n) = -8X \cos\left(\frac{n\pi}{2}\right) \ , \tag{2.50}$$

cf. fig. 2.5, which is consistent with eq. (2.48) for $n \rightarrow 2$ and $X \ll 1$.

As a matter of fact, bosonisation theory is only valid, if the band width t is sufficiently large compared to any other interactions, such that a linearization close to the Fermi surface holds, cf. sec. 2.2.2. In case of the Hirsch model it is a crucial question, where the bosonisation results collapse.

2.3.3. The Exactly Solvable Case $X = 1$

The Hirsch model is exactly solvable for $X = 1$. This is possible due to a number of additional symmetries. SCHADSCHNEIDER et al. [72, 73, 74] and ARRACHEA and ALIGIA [75] were able to calculate various ground state properties and determined the complete phase diagram. DOLCINI and MONTORSI [76] studied the complete eigenspectrum and the thermodynamics of the Hirsch model. Here, we briefly summarize some of their results.

Important additional symmetries at $X = 1$ are given by

1. a full particle-hole symmetry, which is evident from eq. (2.47).

2. The total number of of doubly occupied sites

$$N_{\uparrow\downarrow} = \sum_i n_{i\uparrow} n_{i\downarrow} \tag{2.51}$$

   is conserved.

3. The Hamiltonian exhibits an SU(2) pseudo-spin symmetry, which is induced by the so-called η-pair operators

$$\eta = \sum_i c_{i\uparrow} c_{i\downarrow} \ , \qquad \eta^\dagger = \sum_i c_{i\downarrow}^\dagger c_{i\uparrow}^\dagger \quad \text{and}$$

$$\eta^z = \frac{1}{2} \sum_i \left(1 - c_{i\uparrow}^\dagger c_{i\uparrow} - c_{i\downarrow}^\dagger c_{i\downarrow} \right) \ . \tag{2.52}$$

We analyze the spectrum of $\mathcal{H}_X$ in detail. As $N_{\uparrow\downarrow}$ is conserved, the eigenbasis of $\mathcal{H}_X$ is also an eigenbasis of the complete Hamiltonian $\mathcal{H}$. The key idea to solve the $X = 1$ case is to separate the local states $\{|0\rangle, |\uparrow\rangle, |\downarrow\rangle, |\uparrow\downarrow\rangle\}$ into two groups of particles, which are called SUTHERLAND species [77, 78]

$$A = \{|\uparrow\rangle, |\downarrow\rangle\} \quad \text{and} \quad B = \{|\uparrow\downarrow\rangle, |0\rangle\} \ . \tag{2.53}$$

Placing two particles of the A species on neighboring sites (or B species respectively) it appears from fig. 2.4, that the hopping process is not possible due to $1 - X = 0$. Conversely, hopping processes of different species simply *permute* A and B species, i.e. $AB \leftrightarrow BA$. This property can be used to rearrange the FOCK space

$$\mathcal{F} = \bigoplus_{N_A = 0}^{L} \mathfrak{H}_{N_A} \tag{2.54}$$

in sub-Hilbert spaces $\mathfrak{H}_{N_A}$ of constant number of A species $N_A = N - 2N_{\uparrow\downarrow}$. The hopping process of $\mathcal{H}|\mathfrak{H}_{N_A}$ then simply looks like free spinless fermions

$$\mathcal{H}_X|\mathfrak{H}_{N_A} = -\sum_{\langle ij \rangle} a_i^\dagger a_j = -\sum_k \epsilon_k n_k^A \ . \tag{2.55}$$

Here, species A are interpreted as fermion particles whereas species B as empty sites. The operator $n_k^A \in \{0, 1\}$ counts A species with momentum

$$k = \pi j/(L + 1), \quad k = 1 \dots L \tag{2.56}$$

and free fermion energy $\epsilon_k = 2\cos(k)$, where $\sum_k n_k^A = N_A$.
Now it is easy to observe the complete spectrum of $\mathcal{H} = \mathcal{H}_X + \mathcal{H}_U$ in the subspace $\mathfrak{H}_{N_A}$

$$E(\{n_k^A\}, N_{\uparrow\downarrow}) = \sum_k \epsilon_k n_k^A + U N_{\uparrow\downarrow} \ . \tag{2.57}$$

The degeneracy of each energy level reads

$$g(\{n_k^A\}, N_{\uparrow\downarrow}) = 2^{N_A} \cdot \binom{L - N_A}{N_{\uparrow\downarrow}} \ , \tag{2.58}$$

which results from simple combinatory arguments. Consider, that we have N_A particles of species A, where each one is either an $|\uparrow\rangle$ or $|\downarrow\rangle$ particle. Thus, there are 2^{N_A} configurations. From the rest of $L - N_A$ particles there should be $N_{\uparrow\downarrow}$ doubly occupied sites, which leads to the binomial coefficient $\binom{L-N_A}{N_{\uparrow\downarrow}}$. As there are $\binom{L}{N_A}$ variations to build a sequence $\{n_k^A\}$ of N_A A-species, the dimension of $\mathfrak{H}_{N_A}$ yields

$$\dim \mathfrak{H}_{N_A} = \binom{L}{N_A} \sum_{N_{\uparrow\downarrow}=0}^{L-N_A} g(\{n_k^A\}, N_{\uparrow\downarrow}) = \binom{L}{N_A} 2^L \ . \tag{2.59}$$

Therefore, the constructed Fock space indeed covers the complete Hilbert space

$$\dim \mathcal{F} = \sum_{N_A = 0}^{L} \dim \mathfrak{H}_{N_A} = 4^L \ . \tag{2.60}$$

The ground state energy (per site) in each subspace N_A is obtained by the ground state energy of N_A free fermions and the Coulomb term

$$e_0 = E_0/L = -\frac{2}{\pi}\sin(n_A\pi) + Un_{\uparrow\downarrow} \ , \tag{2.61}$$

where $n_A = N_A/L$ and $n_{\uparrow\downarrow} = N_{\uparrow\downarrow}/L$. Minimizing eq. (2.57) for all n_A yields the ground state in the complete Fock space. The minimal $\mathfrak{H}_{N_A}$ subspace is found for

$$n_A = \begin{cases} 0 & \text{for } U \leq -4 \\ \frac{1}{\pi}\arccos(-U/4) & \text{for } -4 \leq U \leq U_c = -4\cos(\pi n) \\ n & \text{for } U \geq U_c \end{cases} \tag{2.62}$$

which leads to the ground state phase diagram shown in fig. 2.6.
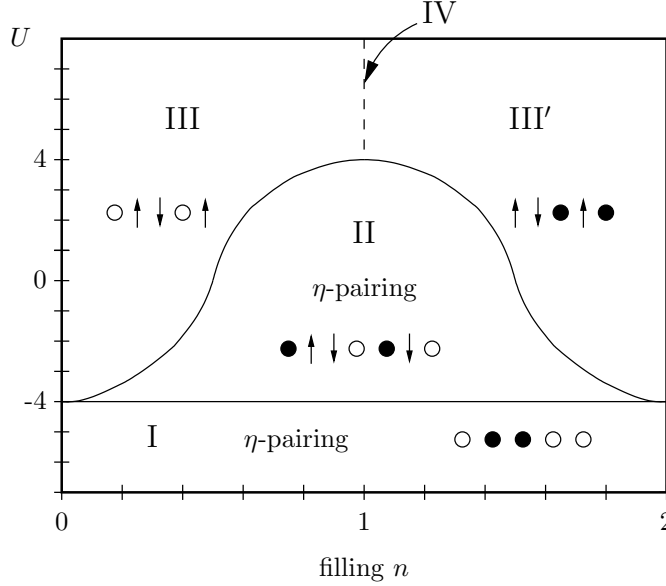
Figure 2.6.: Phase diagram of the Hirsch model at $X = 1$. The structure of the ground states is roughly visualized in each phase, where circles (○) represent empty, ↑ and ↓ single occupied and bullets (●) doubly occupied sites.

One finds five phases (I, II, III, III',IV), whose ground states structure is also schematized in the figure. One can show that the ground states of III are those of the $U = \infty$ Hubbard model, where no doubly occupied sites occur. Phase III' is the particle-hole symmetric pendant of III. The ground states of phase I consist of pairs and empty sites only, whereas in II each local configuration is possible. An astonishing property of phase I and II is that among the ground states one finds η-pairing states [74, 56] which exhibit ODLRO

$$\lim_{|i-j|\to\infty} \left\langle P_s^\dagger(i)P_s(j)\right\rangle \neq 0 \ . \tag{2.63}$$

The phases I,II,III and III′ fall into the TLL universality class. Contrarily, in IV a charge gap opens and the model is insulating. A more detailed analysis of the thermodynamics is given in chapter 3 in the framework of our numerical studies. We already notice here a specialty of the model, namely the vanishing of the spin velocity $v_s = 0$ [76]. Therefore spin excitations are completely degenerate.

2.3.4. The Non-Integrable Regime $0 < X < 1$

As we have seen in the last two sections, the physics of weak $X \ll 1$ and $X = 1$ are quite different. For the intermediate regime $0 < X < 1$ intensive numerical studies have been performed by QUAISSER et al. [79, 80] and ARRACHEA et al. [81] , using the LANCZOS method to diagonalize sufficiently small systems exactly.
QUAISSER et al. were able to compute the energy spectrum and ground state correlation functions for chain lengths $L \leq 16$ with high precision. Using finite-size scaling, they interpolated the data to obtain the thermodynamic limit $L \rightarrow \infty$. We briefly summarize the most important results, which characterize the Hirsch model for intermediate $0 < X < 1$.
It was shown that for sufficiently large fillings, a spin gap opens for $0 < X \lesssim 0.75$ (cf. fig. 2.8 (a)) and the Hirsch model falls into the universality class of a LEL. The numerical computation of K_c yields $K_c > 1$ for the spin gap phase, cf. fig. 2.8 (b). Thus, superconducting singlet pair correlations are strongly enhanced. The spin gap as well as K_c was found to be *maximal* for $X \approx 0.5$.
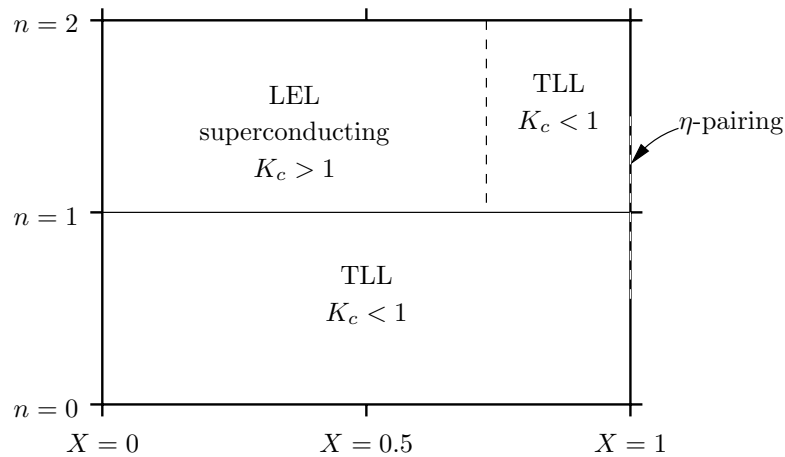

Figure 2.7.: Schematic plot of the Hirsch model's phase diagram for $U = 0$, which has been derived from numerical and analytic studies.

For that reason, QUAISSER investigated this particular point in more detail. An analysis of the $X = 0.5$ case shows that the gap opens for approximately half filling, cf. 2.8 (c). This is at least on a qualitative level in accordance with the findings of bosonisation, cf. sec. 2.8.
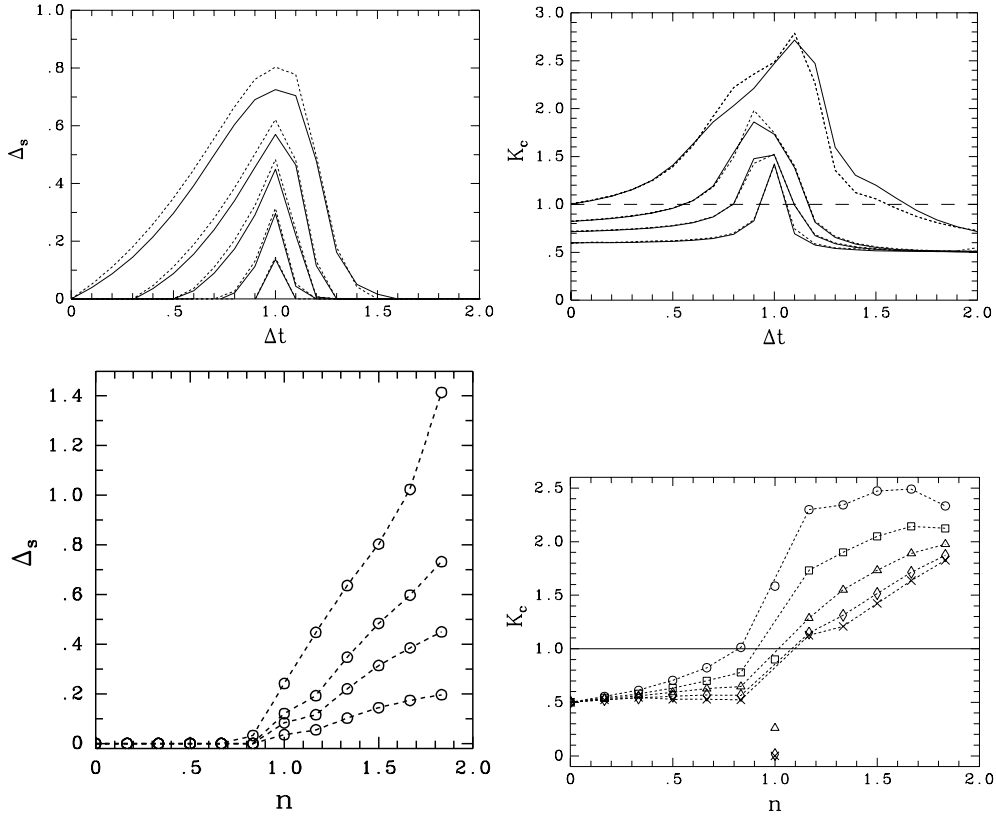
Figure 2.8.: The figures are taken from numerical calculations of QUAISSER [79].
(a) The upper left figure plots the spin gap Δ_s as a function of
$\Delta t = X/2$ for a fixed density $n = 3/2$. The respective curves belong
to different Coulomb potentials $U = 0, 1, 2, 4, 10$ (top to bottom).
Dotted and solid curves depict computations of $L = 12$ and $L = 16$
lattice sites. (b) The upper right figure plots the corresponding
calculations of K_c for $U = 0, 2, 4, 10$ (top to bottom), where dotted
and solid curves again show $L = 12$ and $L = 16$. (c) The lower
left figure plots for fixed $X = 0.5$ the spin gap as a function of the
filling n, where the respective curves belong to $U = 0, 2, 4, 10$ (top
to bottom). (d) The corresponding computations of K_c are plotted
in the lower right figure for $U = 0, 1, 2, 4, 10$ (top to bottom).

If the Coulomb potential is switched on, the LEL phase is repressed, which is shown in fig. 2.8 (d). This can be explained by the fact that a repulsive U destroys the pair building. Fig. 2.8 (d) additionally gives evidence that bosonisation quantitatively fails for large $X = 0.5$. The spin gap should vanish for $U = 10$, because $U_{\text{eff}}(n = 3/2) \approx -2.82 < 0$, cf. eq. (2.49).

For $U = 0$ the numerical studies qualitatively suggest the phase diagram, which is shown in fig. 2.7. Note, that the η-pairing phase at $X = 1$ is a specialty of the high symmetries at this singular point.

The present thesis expands the $T = 0$ studies to *finite* temperatures by using the TMRG method. The $T = 0$ properties summarized above are essential for the understanding of the low temperature behavior. E.g. the occurrence of a spin gap Δ_s is also visible in the thermodynamics for temperatures $T \sim \Delta_s$. We will discuss these matters in detail in chapter 3.

3. TMRG Results for the Hirsch Model

3.1. Introduction

In chapter 1 we have discussed the TMRG algorithm in a quite general context of an arbitrary quantum system. In this section the TMRG is now applied to the Hirsch model. Before we present the numerical data in section 3.2 to 3.3, we point out some important details about the practical realization of the TMRG.

3.1.1. The Problem of Fermion Statistics

From the conventional DMRG it is well known that the fermion statistics have to be taken into account, in particular if one is interested in correlation functions [82]. However, the Trotter-Suzuki decomposition does *not* care about fermionic commutator relations between different plaquettes.
In case of the Hirsch model we discovered, that particularly the singlet correlations were completely wrong without considering fermion statistics. But triplet, density and spin correlations as well as all other thermodynamic properties suit fine. This may be a reason why the relevance of the fermion statistics never have been considered before.
In the conventional DMRG one usually stores the renormalized Hamiltonian in a Fock space manner [82]. The representation of $c_i^{(\dagger)}$ in Fock space turns to a "sign problem": if $\left|N; n_1 \cdots n_L\right\rangle$ is a N-particle state (here for simplicity spinless fermions are considered) with

$$N = \sum_{k=1}^{L} n_k \quad \text{and} \quad n_k \in \{0, 1\} \ , \tag{3.1}$$

we have

$$
\begin{aligned}
c_j^\dagger \left|N; \cdots n_j \cdots\right\rangle &= (-1)^{N_j} \left|N+1; \cdots n_j + 1 \cdots\right\rangle \\
c_j \left|N; \cdots n_j \cdots\right\rangle &= (-1)^{N_j} \left|N-1; \cdots n_j - 1 \cdots\right\rangle
\end{aligned} \tag{3.2}
$$

where

$$N_j = \sum_{k=1}^{j-1} n_k \ . \tag{3.3}$$

Unfortunately, it is not possible to follow this strategy in the TMRG algorithm. The QTM has something like a local structure, involving only two sites of the quantum chain. Therefore, we choose an alternative approach, using a Jordan-Wigner transformation (JWT) [83]. The JWT maps a fermion model onto a

conventional spin system. The details of the JWT can be found in the appendix A. The basic idea is to express the fermion operators $c_j^{(\dagger)}$ with *anti-commutator* relations by spin operators, which *commute* for different lattice sites.

This is possible by the identification

$$c_{j\sigma} = K_{j\sigma} S_{j\sigma}^- \quad \text{and} \quad c_{j\sigma}^\dagger = S_{j\sigma}^+ K_{j\sigma} \;, \tag{3.4}$$

where the unitary operators $K_{j\sigma}$ are defined by

$$K_{j\uparrow} = \mathrm{e}^{\mathrm{i}\pi \sum_{i,\sigma}^{j-1} S_{i\sigma}^+ S_{i\sigma}^-} \quad \text{and} \quad K_{j\downarrow} = \mathrm{e}^{\mathrm{i}\pi \sum_{i,\sigma}^{j} S_{i\sigma}^+ S_{i\sigma}^-} \;. \tag{3.5}$$

$S_{i\sigma}^\pm$ are conventional spin-1/2 matrices, where two different "types" of spins are distinguished by σ. That eq. (3.4) really induces fermion operators is proved in the appendix A.

Inserting the JWT into the Hamiltonian (2.46), the hopping terms $c_i^\dagger c_j$ modify, whereas the diagonal charge operators $n_{i\sigma}$ transform canonically:

$$
\begin{aligned}
c_{i+1\uparrow}^\dagger c_{i\uparrow} \quad &\rightarrow \quad (-1)^{n_{i\downarrow}} S_{i+1\uparrow}^+ S_{i\uparrow}^- \\
c_{i+1\downarrow}^\dagger c_{i\downarrow} \quad &\rightarrow \quad (-1)^{n_{i+1\uparrow}} S_{i+1\downarrow}^+ S_{i\downarrow}^- \\
n_{i\sigma} \quad &\rightarrow \quad S_{i\sigma}^+ S_{i\sigma}^-
\end{aligned}
\tag{3.6}
$$
$$\tag{3.7}$$

Note, that periodic boundary conditions may transform to twisted ones, but this is irrelevant for our studies of the thermodynamic limit. Obviously, the "sign problem", which we mentioned before, is reflected intrinsically by the modified interaction (3.6). It is important to notice, that $h_{i,i+1}$ in terms of spins is no longer parity invariant, which has to be taken into accound in the TMRG algorithm.

3.1.2. Quantum Numbers and Correlation Lengths

In section 1.2.3 we have already discussed the relevance of quantum numbers for the computational performance. The Hirsch Hamiltonian commutes with the total (Pauli) spin $S = \sum_i n_{i\uparrow} - n_{i\downarrow}$ and total charge $N = \sum_i n_{i\uparrow} + n_{i\downarrow}$, cf. sec. 2.3. But alternatively, we consider the quantum number of up- and down-spins $N_\sigma = \sum_i n_{i\sigma}$ in the TMRG algorithm. The corresponding quantum number of QTM T_M consequently reads $\Delta N_\sigma = \sum_j (-1)^j n_{j\sigma}$. Hence, the QTM blocks are characterized by the tuple $(\Delta N_\uparrow, \Delta N_\downarrow)$. The leading eigenvalue Λ_0 is located in the $(0,0)$ block, using the arguments of section 1.2.3.

The quantum numbers $(\Delta N_\uparrow, \Delta N_\downarrow)$ play an important role with respect to correlation lengths. They can be used to assign the eigenvalues Λ_α to the respective type of correlation. To which correlation function an eigenvalue of the QTM belongs to, is controlled by M_α given in eq. (1.51).

M_α is not vanishing, if $T_M(O)|\Lambda_0^R\rangle$ and $\langle\Lambda_\alpha^L|$ have the same quantum numbers $(\Delta N_\uparrow, \Delta N_\downarrow)$. If spin or density correlations (cf. sec. 2.2.3) are considered, O is diagonal in real space and $T_M(O)$ maps $|\Lambda_0^R\rangle$ onto the $(0,0)$ block. Therefore, density and spin correlation lengths are situated in the *same* block $(0,0)$ and have to be distinguished by calculating M_α explicitly.
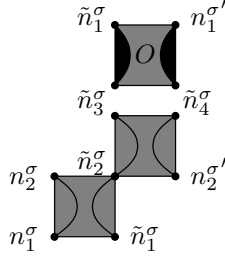
Figure 3.1.: Modified QTM $T_{M=1}(O)$ where the indices are quantum numbers $(n_i^\uparrow, n_i^\downarrow)$ of each local lattice site

The singlet and triplet pair operators (cf. sec. 2.2.3), leading to superconducting correlations, are off-diagonal and *change* the quantum number. For demonstration purpose we consider the modified QTM $T_{M=1}(c_{i\uparrow}^\dagger c_{i+1\downarrow}^\dagger)$. The indices n_j^σ, $n_j^{\sigma\prime}$ and $\tilde{n}_j^\sigma$ label the quantum numbers of each local lattice site, where $\sigma = \uparrow, \downarrow$. We obtain the equations

$$n_1^\sigma + \tilde{n}_1^\sigma = n_2^\sigma + \tilde{n}_2^\sigma, \quad \tilde{n}_2^\sigma + n_2^{\sigma\prime} = \tilde{n}_3^\sigma + \tilde{n}_4^\sigma,$$

$$\tilde{n}_1^\uparrow = \tilde{n}_3^\uparrow + 1, \quad \tilde{n}_1^\downarrow = \tilde{n}_3^\downarrow, \quad n_1^{\downarrow\prime} = \tilde{n}_4^\downarrow + 1, \quad n_1^{\uparrow\prime} = \tilde{n}_4^\uparrow \tag{3.8}$$

which resolves to

$$n_1^\sigma - n_2^\sigma = n_1^{\sigma\prime} - n_2^{\sigma\prime} - 1 \implies \Delta N_\sigma = \Delta N_\sigma' - 1 . \tag{3.9}$$

Hence, $T_M(c_{i\uparrow}^\dagger c_{i+1\downarrow}^\dagger)$ changes the quantum number ΔN_σ by one. As a consequence, the singlet pair correlation lengths of $P_s^{(\dagger)}(i)$ are found in the $(\pm 1, \pm 1)$ block. Similarly, one can show that the triplet pair correlation lengths are situated in the $(\pm 1, \pm 1)$, $(\pm 2, 0)$ and $(0, \pm 2)$, depending on the operator $P_{tl}^{(\dagger)}(i)$. In order to uniquely distinguish d-d, s-s, sp and tp correlations we thus calculate the leading QTM eigenvalues of the $(0, 0)$, $(1, 1)$ and $(2, 0)$ block and additionally M_α in $(0, 0)$ block.

The JWT described above gets important particularly for the $(1, 1)$ block eigenvalues. Numerically we found out, that the eigenvalues of this block change without JWT. However, the $(0, 0)$ and $(2, 0)$ blocks are not affected.

3.2. Thermodynamics of the Hirsch model

We now present numerical TMRG results for the parameter region $0 \leq X \leq 1$, which is representative for all X, cf. sec. 2.3.1. We use a *grand canonical* description, since in the fermion model particles can be added or removed. Thus, a chemical potential μ controls the density n of particles. It is not possible to design a TMRG algorithm for a fixed density of particles due to the "local structure" of the quantum transfer-matrix (cf. eq. (1.35)). Additionally, we

include a magnetic field h, such that the Hamiltonian reads

$$\mathcal{H} = \mathcal{H}_X + \mathcal{H}_U \underbrace{-h\sum_i m_i - \mu \sum_i n_i}_{\mathcal{H}_{\text{ext}}} \tag{3.10}$$

where $n_i = n_{i\uparrow} + n_{i\downarrow}$ is the local density and $m_i = n_{i\uparrow} - n_{i\downarrow}$ the local Pauli magnetization.

We are able to calculate the following thermodynamic quantities: the grand canonical potential φ, local thermal expectation values (e.g. local density n), charge and spin susceptibilities χ_c and χ_s and the specific heat c_μ.

The grand canonical potential $\varphi(T, \mu)$ is directly accessible by the largest eigenvalue of the QTM, cf. eq. (1.44). The charge susceptibility

$$\chi_c(T, \mu) = \frac{\partial n}{\partial \mu}\Big|_T \tag{3.11}$$

is obtained by computing the local density $n = n(T, \mu) = \langle n_i \rangle$ (cf. eq. (1.49)) of electrons for two different chemical potentials $\mu - \Delta\mu$ and $\mu + \Delta\mu$. Then, we use numerical derivatives

$$\chi_c(T, \mu) \approx \frac{n(T, \mu + \Delta\mu) - n(T, \mu - \Delta\mu)}{2\Delta\mu} \tag{3.12}$$

to approximate χ_c, where typically $\Delta\mu \sim 10^{-2}$ is chosen. Similarly, the spin susceptibility

$$\chi_s\big|_{h=0} = \frac{\partial m}{\partial h}\Big|_{\mu,T;h=0} \tag{3.13}$$

is obtained by the numerical derivative of the (Pauli) magnetization $m = m(T, \mu, h) = \langle m_i \rangle$ varying the magnetic field h.

The natural form of the specific heat in a grand canonical formulation is given by

$$c_\mu = T\frac{\partial s}{\partial T}\Big|_\mu = T\frac{\partial^2 \varphi}{\partial T^2}\Big|_\mu \ , \tag{3.14}$$

where s labels the local entropy. But usually data for the specific heat at constant density n is considered, which is related to c_μ by the thermodynamic relation

$$c_n = T\frac{\partial s}{\partial T}\Big|_n = c_\mu - T\frac{\partial n}{\partial T}\Big|_\mu \frac{\partial \mu}{\partial n}\Big|_T \ . \tag{3.15}$$

We mention, that concrete predictions about the low temperature asymptotics of the susceptibilities and the specific heat are known for the TL and LE model. These are based on results of the conformal field theory (CFT) (for an overview see e.g. [84, 85]).

The idea of CFT is that a model at criticality and with short-range interactions is invariant under a large group of *conformal transformations*. Thereby extremely powerful and *general* conclusions are possible. As an example, the CFT is used to relate properties of finite quantum chains with those of an infinite one, or temperature $T = 0$ properties with finite temperature $T > 0$ physics. Here, the latter one is interesting for our study of low-temperature physics.

We summarize the essential results for the thermodynamics [86, 87]. The free energy per site $f(T, n) = \varphi + \mu N$ takes a quadratic form

$$f = e_0 - kT^2 \ . \tag{3.16}$$

The constant k in case of the TLL explicitly reads

$$k = \frac{\pi}{6} \left(\frac{1}{v_c} + \frac{1}{v_s} \right) \ , \tag{3.17}$$

and depends on the spin and charge velocities $v_{v/s}$, defined in sec. 2.2.2. As a consequence, the specific heat has a linear dependence on T

$$c_n = T \frac{\partial^2 f}{\partial T^2} \Big|_n = \frac{k}{2} T \ . \tag{3.18}$$

For charge and spin susceptibilities one observes for $T \to 0$ [88]

$$\chi_{c/s} = \frac{K_{c/s}}{2\pi v_{c/s}} \ , \tag{3.19}$$

Note, that $K_s = 1$ for the TLL, cf. sec. 2.2.2. Eq. (3.19) suggests that the reciprocals of the velocities can be interpreted as the density of states in respect to spin and charge excitations. For a LEL the spin degrees of freedom are frozen out for small temperatures, which correspond to vanishing spin excitations $1/v_s \to 0$.

The mentioned general properties of TLL and LEL based on CFT will be very useful for the interpretation of the thermodynamic results obtained by the TMRG algorithm. It is even possible to predict the structure of the correlation functions, which is discussed later on in sec. 3.3.1.

3.2.1. TMRG Results for $X = 1$

As already shown in sec. 2.3.3, the Hirsch model is integrable for $X = 1$ and the complete eigenspectrum is accessible. Adding $\mathcal{H}_{\text{ext}}$ to the Hirsch Hamiltonian (2.46) splits up the energy levels of eq. (2.57). The spectrum can be used to calculate the partition function $Z_L = \operatorname{tr} e^{-\beta \mathcal{H}}$ for a chain of length L exactly. Thereby, the grand canonical potential

$$-\beta \varphi = \lim_{L \to \infty} \frac{\ln Z_L}{L} \tag{3.20}$$

for the thermodynamic limit $L \to \infty$ can be determined [76], which explicitly reads

$$-\beta \varphi = \ln(1 + e^{2\beta\mu}) + \frac{1}{\pi} \int_0^\pi \ln \left(1 + e^{-\beta(\epsilon_k - \mu^*)} \right) \mathrm{d}k \ . \tag{3.21}$$

μ^* is an "effective" chemical potential given by

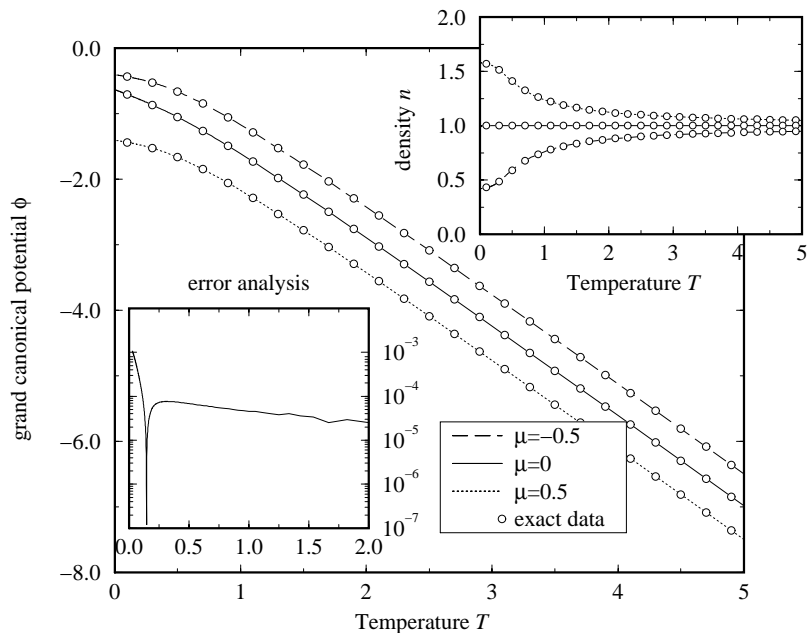$$\mu^*(\mu, \beta, h) = \mu + \frac{1}{\beta} \ln \frac{2 \cosh \beta h}{1 + e^{2\beta\mu}} \ . \tag{3.22}$$

Figure 3.2.: Grand canonical potential φ as a function of temperature for $X = 1$ and chemical potentials $\mu = -0.5, 0, 0.5$. The absolute deviation from the exact value in dependence of the temperature is plotted in the left inset for $\mu = 0$. The corresponding TMRG data for the density $n = n(T, \mu)$ is depicted in the right inset. For comparison exact data using eq. (3.21) are shown by circles ($\circ$).

Details of the analytic derivation (following [76]) are summarized in appendix B. Rigorous studies of the specific heat, susceptibilities etc. are thus possible.

We basically use the exact results to check the precision of our TMRG data. In particular, we focus on the case of *vanishing* Coulomb potential $U = 0$ and magnetic field $h = 0$. $h \neq 0$ is only considered to calculate the spin susceptibility, cf. eq. (3.13). The intention of theses choices is to elucidate the physical influence of the bond-charge interaction X *only*, even if physically U is usually not small (cf. eq. (2.12)).

The data presented as follows is computed for $\epsilon = 0.05$ (cf. eq. (1.24)) and $m = 70 - 100$ retained states in the renormalization process (cf. sec. 1.2). We typically compute $M \approx 1000 - 2000$ TMRG iterations, depending on the stability of the numerics, which correspond to a minimal reachable temperature of $T \approx 0.02 - 0.01$. As we use a grand canonical description, the chemical potential μ is used to control the density n of particles. Note, that the density is also temperature dependent $n = n(T, \mu)$.

In fig. 3.2 the grand canonical potential φ is plotted for the chemical potentials $\mu = -0.5, 0, 0.5$. For low temperatures, we have a quadratic dependence, in correspondence with eq. (3.16). The intersection with the ordinate is situated at $\varphi_0 = e_0 - \mu n_0$, where e_0 is the ground state energy and $n_0 = n(T \to 0)$. Contrarily, φ gets linear for the high temperature regime. The latter fact can be

understood by an entropy argument. As the entropy per site $s(T \to \infty) = \ln(4)$ gets constant for $T \to \infty$, we have

$$\frac{\partial \varphi}{\partial T}\Big|_{\mu, T \to \infty} = -s(T \to \infty) = -\ln 4 . \tag{3.23}$$

The temperature dependence of the density $n(T, \mu)$ is plotted in the upper inset. The particle-hole symmetry of the model is confirmed by the symmetry of $n(T, \pm 0.5)$ as well as by the potentials $\varphi(T, \pm 0.5)$, which are only shifted by $\Delta \mu = 1$.

Our data is compared to exact results, calculated by eq. (3.21), cf. the lower inset of fig. 3.2. The absolute deviation is less than 10^{-4} for temperatures $T > 0.1$ and for $0.02 < T < 0.1$ less than 10^{-3}. Not explicitly shown here, the errors of the density n as well as other expectation values (e.g. the magnetization) are approximately of the same order. This is a remarkable precision even in the low temperature region. The Trotter-Suzuki decomposition in eq. (1.25) is responsible for an error of at least $10^{-3} \sim \epsilon^2$ since $\epsilon = 0.05$. For low temperatures the error is expected to increase due to the renormalization steps.

It is interesting to investigate also the complete density $n(T, \mu)$ as a function of temperature T and chemical potential μ, cf. fig. 3.3. For $T \to 0$ one observes a discontinuity for $\mu = 0$. This can be explained by the ground states of the η-pair phase, which occurs for $0.5 < n < 1.5$, cf. sec. 2.3.3 . Here, all ground states with different numbers of pairs $N_{\uparrow\downarrow}$ are degenerate. Thus, the chemical potential does not change by adding a particle, because a new bound pair is formed without changing the energy. Note, that therefore the thermodynamics of the η-pair phase can only be realized for $\mu = 0$. Any $\mu \neq 0$ induces $n < 0.5$ or $n > 1.5$ and falls into the $U = \infty$ phase, cf. sec. 2.3.3.

Fig. 3.4 depicts the spin and charge susceptibilities for $X = 1$ and $\mu = 0, 0.5, 1.0$. The comparison with exact data results in a relative error less than 10^{-2} for temperatures $T \gtrsim 0.1$. Not surprisingly, it is larger than that for φ, because numerical errors are propagating through the numerical derivatives.

The findings of CFT in eq. (3.19) can be used to interpret the results of fig. 3.4. The ground states of $X = 1$ for $n < 0.5$ (and after particle-hole transformation for $n > 1.5$) corresponds to the $U = \infty$ Hubbard model, cf. sec. 2.3.3. For the $U = \infty$ Hubbard model it is known that

$$v_s = 0 \quad \text{and} \quad v_c = 2t |\sin(\pi n)| . \tag{3.24}$$

The spin excitations exhibit no dispersion due to degeneracy and are completely suppressed [76]. In fig. 3.4 we have plotted $\chi_s \cdot T$ to demonstrate, that the spin susceptibility χ_s is diverging for all μ and fillings n in the limit $T \to 0$ since $\lim_{T \to 0} T \chi_s$ is finite. The charge susceptibility χ_c is divergent for $\mu = 0$.

3.2.2. TMRG Results for $0 < X < 1$

We now consider the non-integrable case $0 < X < 1$. From analytical and numerical approaches (see sec. 2.3.4) it is known that a crossover from a TLL phase to a super-conducting LEL is observed. For $X \ll 1$ this is evident, because the bond-charge model is an effective Hubbard model (cf. sec. 2.3.2),
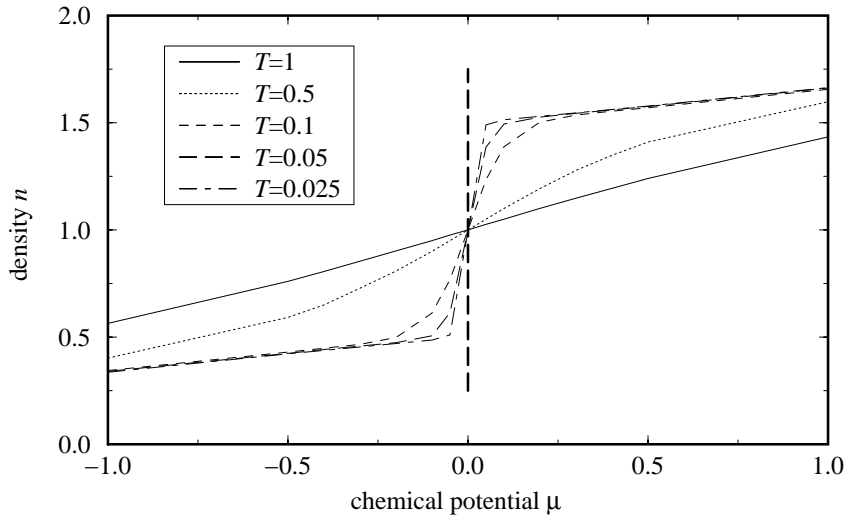
Figure 3.3.: Density $n(\mu, T)$ as a function of temperature and chemical potential for $X = 1$. For $T \to 0$ a discontinuity at $\mu = 0$ is found, where the density has a discontinuity and jumps from $n = 0.5$ to $n = 1.5$.
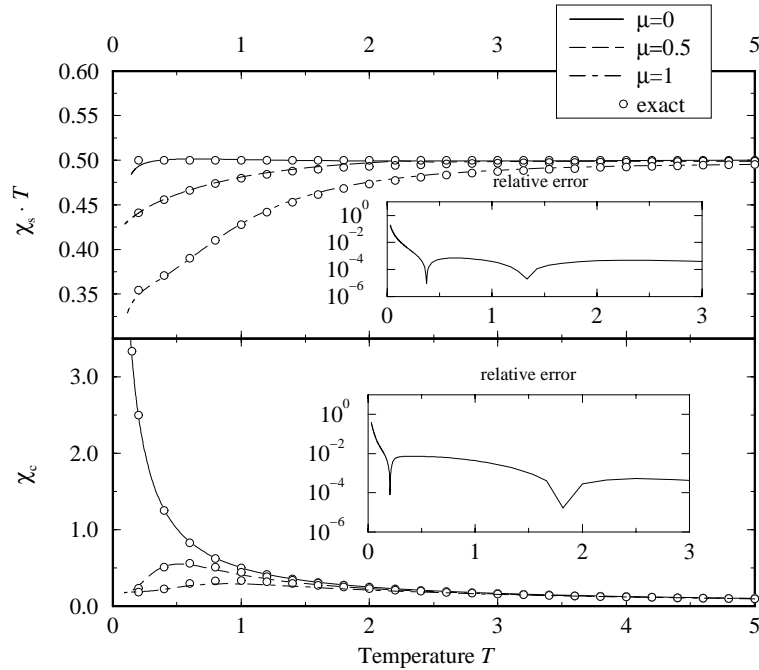

Figure 3.4.: Spin and charge susceptibility as a function of temperature for $X = 1$ and $\mu = 0, 0.5, 1.0$. The upper diagram plots $\chi_s \cdot T$ over T in order to demonstrate that χ_s diverges like $\chi_s \sim 1/T$. The insets depict the relative deviation from exact results for $\mu = 0$.

where the crossover is expected to appear at $U_{\text{eff}} = 0$, corresponding to half-filling $n = 1$ (see eq. (2.49)).

In our thermodynamic study we can identify the existence of a spin gap if the susceptibility χ_s vanishes for $T \to 0$.

In fig. 3.5 χ_s is depicted for fixed chemical potential $\mu = 0.6$ and various hopping amplitudes $0 < X < 1$. For $X > 0.65$ we can clearly verify TLL behavior, because the susceptibility does not vanish for $T \to 0$. At $X \approx 0.65$ we observe a crossover to a LEL phase with $\chi_s(T \to 0) = 0$. Decreasing X further, the gap seems to close again for $X \lesssim 0.3$.

Additionally, the inset of fig. 3.5 shows the density $n(T, \mu = 0.6)$ for the respective parameters X. Note, that $\mu = 0.6$ induces a regime of more than half filling $n > 1$ for each X. Therefore the spin gap should persist especially for $X \ll 1$, which we can not show by our TMRG results. But from the attractive Hubbard model it is known that the spin gap is exponentially small for $U \ll 1$. Since from (2.49) we have $U_{\text{eff}} \ll 1$ for $X \ll 1$, the gap in the bond-charge model becomes extremely small, especially at half filling. The decay of χ_s at $X \ll 1$ is therefore expected at such low temperatures, that are not accessible by TMRG.

To verify that all $X \le 0.5$ exhibit a spin gap we increased the filling in fig. 3.6. Here, the effective Coulomb potential U_{eff} is larger and the spin gap appears in our data.

In order to give a more detailed overview of the thermodynamics of the bond-charge model for $0 < X < 1$, we focus on three particular points $X = 0.1, 0.5$ and $X = 0.9$.

The Case $X = 0.1$

Fig. 3.7 plots the charge and spin susceptibility at $X = 0.1$ for various chemical potentials μ. Additionally, in the inset, the density $n(\mu, T)$ is depicted.

As X is small compared to the bandwidth t, the Hirsch model should coincide with the effective Hubbard model. We check the asymptotics of the susceptibilities χ_s and χ_c for $T = 0$ using eq. (3.19). These can be calculated exactly for the integrable Hubbard model [89, 90]. For a weak (repulsive) Coulomb potential U, one finds

$$v_{c/s} = v_F \left(1 \pm \frac{U}{4\pi t \sin k_F} \right) = v_F \pm \frac{U}{2\pi}, \qquad (3.25)$$

$$K_c = 1 - \frac{U}{4\pi t \sin(k_F)} \qquad (3.26)$$

with $v_F = 2t \sin(k_F)$ and $k_F = \frac{n\pi}{2}$. Using eqs. (3.25), (3.26) and (3.19) we have calculated χ_s and χ_c for $T \to 0$. The density $n_0 = n(\mu, T \to 0)$ which was used to determine k_F is denoted in the legend of fig. 3.7. We observe perfect agreement with our data, which again supports the correspondence of Hubbard and bond-charge model.

Even more evidence of Hubbard-like thermodynamics is given by the shape of the specific heat c_μ. As shown for c_μ in fig. 3.8, two characteristic features can be observed for large and small fillings, a shoulder at low temperatures and a
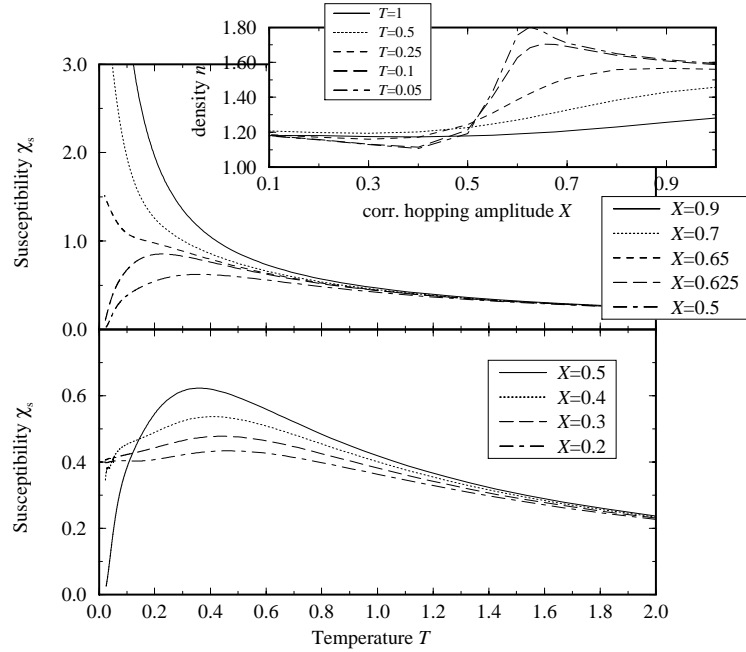
Figure 3.5.: Spin susceptibility as a function of temperature for various amplitudes $X/t = 0.9 \ldots 0.1$ and fixed chemical potential $\mu = 0.6$. The upper figure shows χ_s for $X = 0.9 \ldots 0.5$ the lower one for $X = 0.1 \ldots 0.5$, respectively. The inset depicts the density $n(X, \mu = 0.6, T)$ for various parameters X.
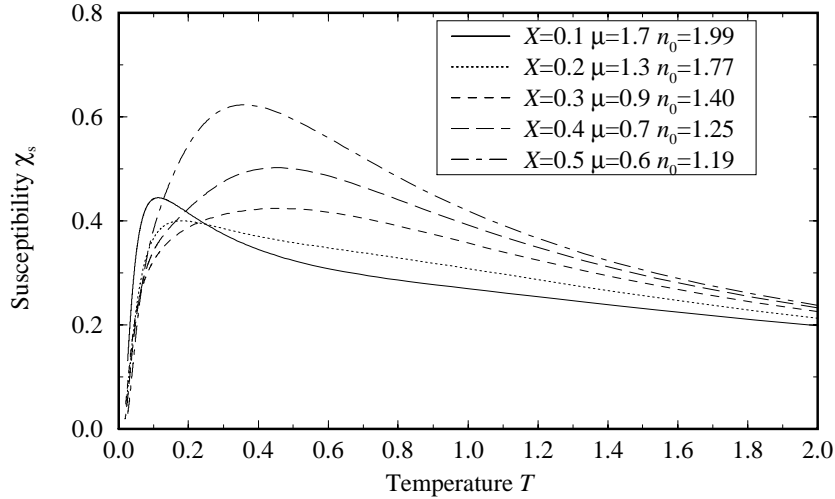

Figure 3.6.: Spin susceptibility χ_s as a function of temperature for the parameter region $X = 0.5 \ldots 0.1$ and sufficiently large fillings. The respective densities $n_0 = n(\mu, T \to 0)$ are given in the legend.
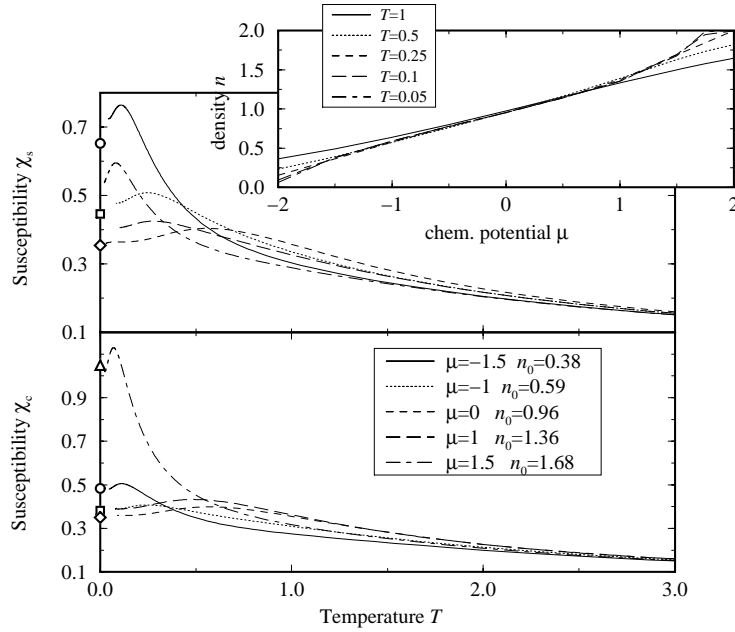
Figure 3.7.: Spin and charge susceptibilities χ_s and χ_c as a function of temperature for $X/t = 0.1$ and various chemical potentials μ. The inset plots the density $n(\mu, T)$. The corresponding $T = 0$ values calculated from the Bethe ansatz for the Hubbard model with effective U_{eff} and t_{eff} are shown by symbols, $(\circ) : \mu = -1.5$, $(\square) : \mu = -1$, $(\diamond) : \mu = 0$ and $(\triangle) : \mu = 1.5$.
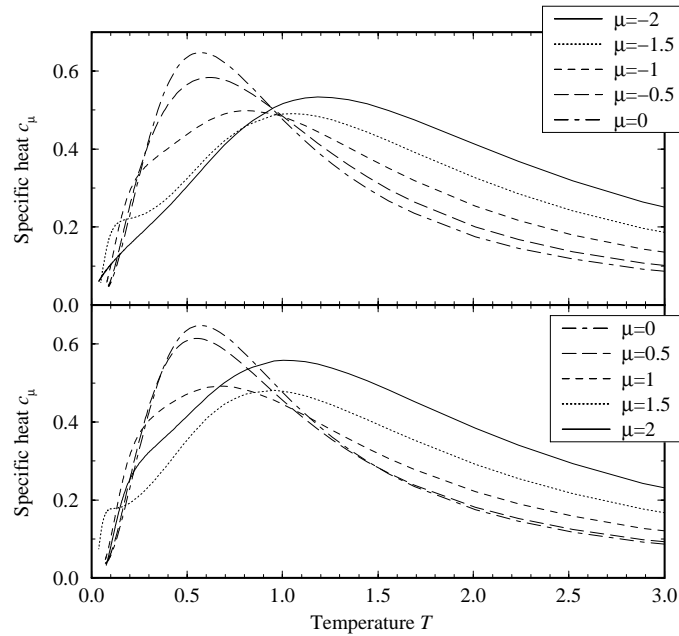

Figure 3.8.: Specific heat c_μ as a function of temperature for $X = 0.1$ and chemical potentials $\mu \leq 0$ (upper figure) and $\mu \geq 0$ (lower figure).

peak at a slightly larger temperature. As in the repulsive Hubbard model these features can be related to spin and charge excitations, respectively. They merge close to half filling where we have effectively a free fermion system for $X \ll 1$. Moreover the regime less than half filling $n < 1$ closely corresponds to $n > 1$. Again, this can be explained by the exponentially small gap, which does not affect the physics at those temperature scales we can observe by TMRG.

The effect of the spin gap manifests itself at larger interactions X.

The Case $X = 0.5$

Fig. 3.9 depicts charge and spin susceptibilites for $X = 0.5$. In contrast to $X = 0.1$, the spin susceptibility χ_s clearly affirms a gap for $n > 1$ since $\chi_s(T \to 0) \to 0$. Therefore the phase transition occurs at half filling, as predicted by bosonisation [69]. A significantly larger spin gap than at $X = 0.1$ is also verified by the specific heat shown in fig. 3.10. The linear behavior of c_μ for $\mu \gtrsim 1$ occurs only at very low temperatures and can not be observed on the temperature scale shown. Here the exponential corrections coming from the finite spin gap dominate.

Even though the numerical data for the thermodynamics suggest Hubbard like behavior on a qualitative level, a more detailed quantitative comparison fails for $X = 0.5$. Since U_{eff} is not small here, we used the Bethe ansatz (instead of eq. (3.25) and (3.26)) to calculate the $T \to 0$ values of χ_s and χ_c for the (effective) Hubbard model. Obviously, the exact results, which are also depicted in fig. 3.9, do not fit to our TMRG data.

The Case $X = 0.9$

For large $X < 1$ the spin gapped phase disappears, which also contradicts the results of bosonisation. As an example we show TMRG data for $X = 0.9$. The susceptibilities and the density, which are shown in fig. 3.11, qualitatively coincide with the $X = 1$ case.

At $\mu \approx 0$ we observe a jump in the density, indicating a phase comparable to the η-pair phase. The spin susceptibility $\chi_s(T \to 0)$ is diverging for all fillings n, which yields $v_s \to 0$. Fig. 3.12 additionally plots the specific heat c_μ for various chemical potentials μ. In fact, the model is observed to be nearly particle-hole symmetric ($\mu \to -\mu$). Note, that for $\mu = 0$ the specific heat exhibits an additional low energy peak. Spin excitations can not contribute to that peak, because they are strongly suppressed due to $v_s \to 0$. For $X = 1$ such peak has also been observed in ref. [76]. It is associated with the melting of pairs. Remarkably, the physics at $X = 0.9$ is very similar to the highly symmetric $X = 1$ case. Thus, $X = 1$ is not a singular point, but the characteristics persist for a certain neighborhood around $X = 1$.
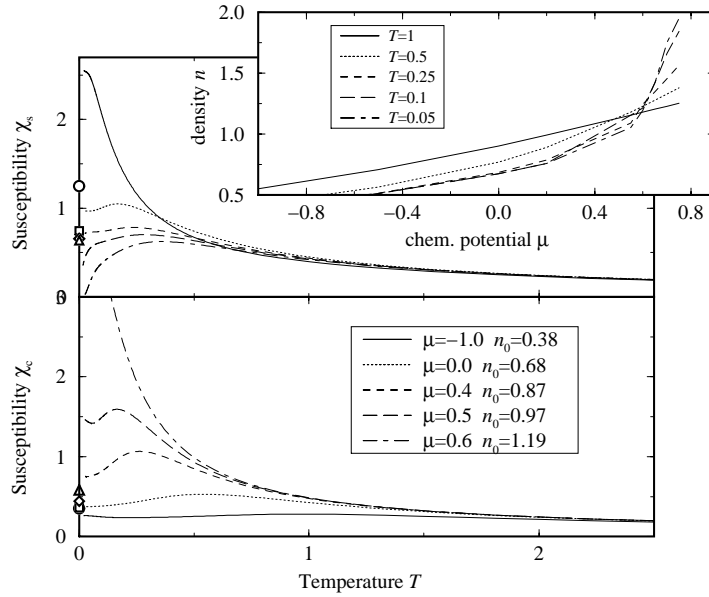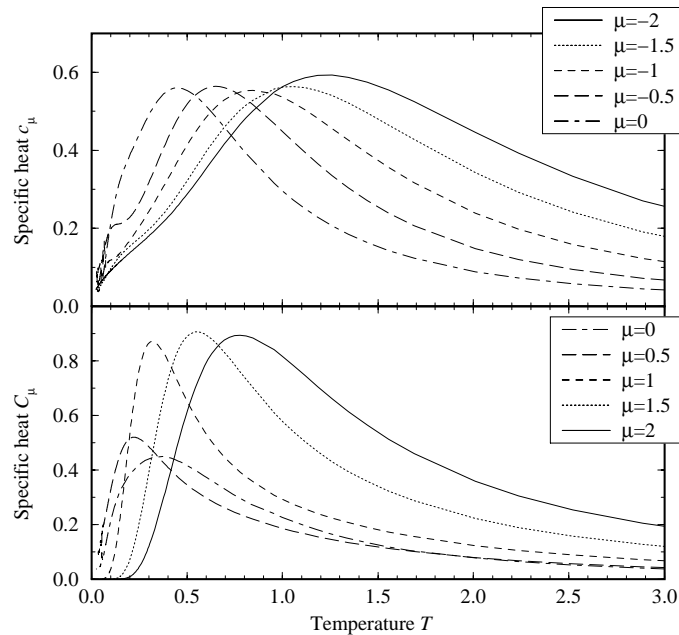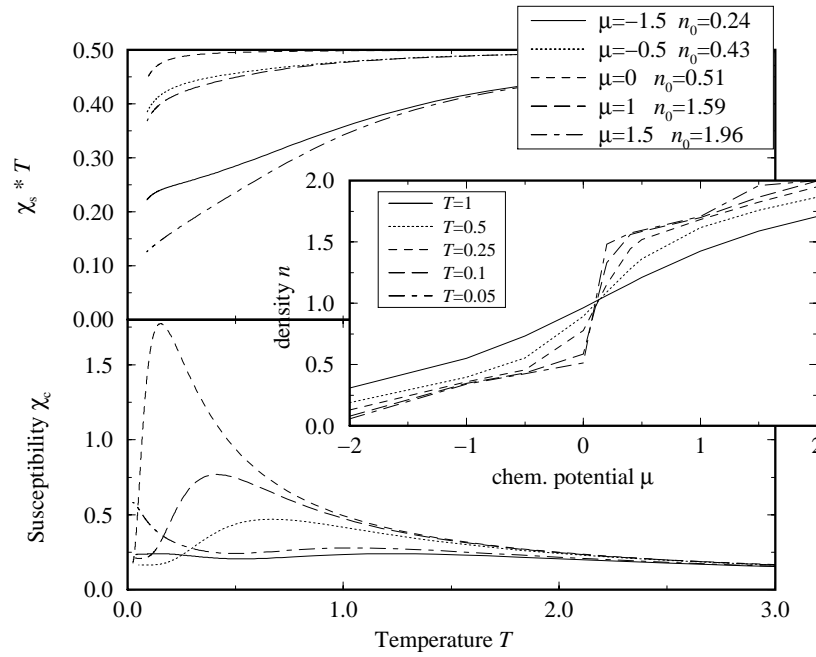
Figure 3.9.: Spin and charge susceptibilities χ_s and χ_c as a function of temperature are depicted for $X = 0.5$ and various chemical potentials μ. The inset plots the density $n(\mu, T)$. The corresponding $T = 0$ values for χ_s and χ_c calculated from the Hubbard model with effective U_{eff} and t_{eff} are shown by symbols, $(\circ) : \mu = -1$, $(\square) : \mu = 0$, $(\diamond) : \mu = 0.4$ and $(\triangle) : \mu = 0.5$.

Figure 3.10.: Specific heat c_μ as a function of temperature for $X = 0.5$ and various chemical potentials $\mu < 0$ (upper figure) and $\mu > 0$ (lower figure).

Figure 3.11.: Spin and charge susceptibilities χ_s and χ_c are depicted for $X = 0.9$ and various chemical potentials μ. The inset shows the density $n(\mu, T)$.
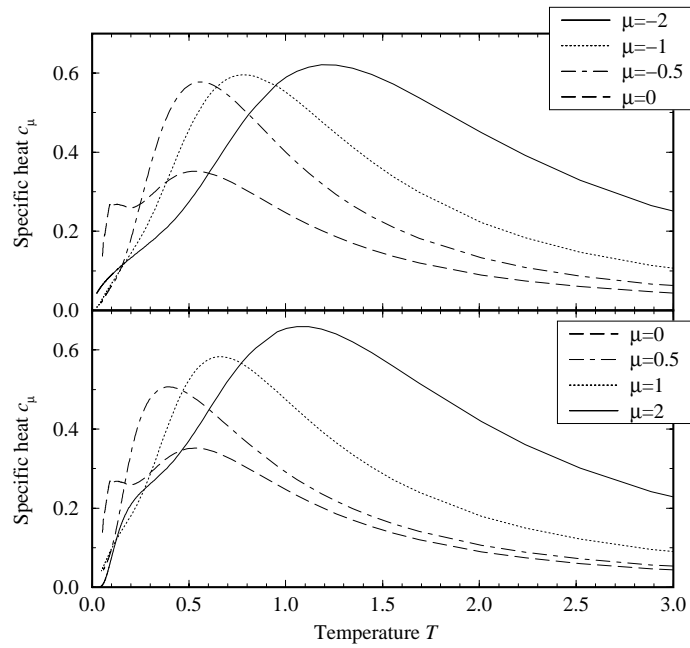

Figure 3.12.: Specific heat c_μ as a function of temperature for $X = 0.9$ and various chemical potentials $\mu \leq 0$ (upper figure) and $\mu \geq 0$ (lower figure).

3.3. Correlation Lengths

3.3.1. Conformal Field Theory Predictions

Before we present TMRG data for the thermal correlation length, it is interesting to review some CFT predictions.

In general, a (static) two-point correlation functions of any (field) operator $\phi(r)$ reads in the CFT

$$\left\langle \phi^\dagger(r)\phi(0) \right\rangle = \sum_{\Delta^\pm} a_{\Delta^\pm} \left\langle \phi^\dagger_{\Delta^\pm}(r)\phi_{\Delta^\pm}(0) \right\rangle \ , \tag{3.27}$$

The later equation shall implicate, that various parts $\left\langle \phi^\dagger_{\Delta^\pm}(r)\phi_{\Delta^\pm}(0) \right\rangle$ with coefficients $a_{\Delta^\pm}$ contribute to the correlation function. These parts intrinsically depend on the type of excitations, which are induced by the operator ϕ.

The CFT predicts a general shape for the correlation parts. In case of a TLL one finds [91, 92, 71]

$$\left\langle \phi^\dagger_{\Delta^\pm}(r)\phi_{\Delta^\pm}(0) \right\rangle = \frac{\mathrm{e}^{-4\mathrm{i}k_F D_c r}\mathrm{e}^{-2\mathrm{i}k_F D_s r}}{r^{2x_c}r^{2x_s}} \sim r^{-\alpha} \ , \tag{3.28}$$

where $\alpha = 2(x_c + x_s)$ and a vanishing magnetization m has been assumed. Here, $x_{c/s} = \Delta^+_{c/s} + \Delta^-_{c/s}$ label the so-called *scaling dimensions*, which are expressed by so-called *conformal weights* $\Delta^\pm_{c/s}$. The conformal weights depend on the excitation type and therefore the index $\Delta^\pm$ was chosen in eq. (3.27). The numbers D_c and D_s are counters of holons (charge excitations) and spinons (spin excitations), which have been transfered from one Fermi point $\pm k_F$ to the other one (cf. fig. 2.3) and lead to an *oscillation* of the correlation function.

In case of the repulsive Hubbard model, which is Bethe integrable, the conformal weights can be calculated explicitly [71]:

$$\Delta^\pm_c = \frac{1}{2}\left(\frac{I_c}{2\xi_c(Q)} \pm \xi_c(Q)\left(D_c + \frac{D_s}{2} \right) \right)^2 + N^\pm_c \tag{3.29}$$

$$\Delta^\pm_s = \frac{1}{4}\left(I_s - \frac{I_c}{2} \mp D_s \right)^2 + N^\pm_s \tag{3.30}$$

The multiplet $(I_c, I_s, D_c, D_s, N_c, N_s)$ of numbers is connected with the Bethe ansatz solutions and characterize the excitations: I_c counts the number of total holes, I_s the number of spin-up ($\uparrow$) holes, D_c (D_s) the number of holon (spinon) transfers from one Fermi point $\pm k_F$ to the other and N_c (N_s) is the number of charge (spin) particle hole excitations. The so-called dressed charge $\xi_c(Q)$ depends specifically on the Hubbard model's couplings and can be expressed by an integral equation. Note, that the possible choices of $D_{c/s}$ are restricted by the Bethe ansatz equations

$$D_c = \frac{I_c + I_s}{2} \mod 1 \quad \text{and} \quad D_s = \frac{I_c}{2} \mod 1 \tag{3.31}$$

and can also be half integers, whereas I_c, I_s , N_c and N_s are integers.

Eq. (3.29) and (3.30) facilitate to calculate the critical exponents of all correlation functions [71]. If we e.g. consider the density correlations $\langle n_r n_0 \rangle$ (cf. eq. (2.40)) there is a non-oscillating and oscillating part. As n_r does not change the particle number we have $I_c = I_s = 0$. The lowest non-oscillating charge excitation, which induces the smallest conformal weight and thus the leading part in $\langle n_r n_0 \rangle$, corresponds to one particle-hole excitation $(0,0,0,0,1,0)$. The conformal weights are $\Delta_c^{\pm} = 1$ and thus $\alpha = 2$ in correspondence with eq. (2.40). Consequently, $(0,0,\mp 1, \pm 1, 0, 0)$ induces the $2k_F$ part with $\alpha = 1 + \frac{\xi_c^2(Q)}{2}$ and $(0,0,\pm 1, 0, 0, 0)$ the $4k_F$ part with $\alpha = 2\xi_c(Q)^2$.

It is worth to emphasize, that eq. (3.29) and (3.30) are not universal, because the couplings of the Hubbard model enter the formulas by the dressed charge $\xi_c(Q)$. But if one calculates all correlations and compares them to the predictions of the TL model (in sec. 2.2.3), it is found, that all critical exponents coincide with the identification

$$K_c = \frac{\xi_c^2(Q)}{2} \ . \tag{3.32}$$

Therefore, it is possible to transfer the results of a special integrable TLL liquid (here the repulsive Hubbard model) to general TLL behavior (as far as not any relevant symmetries are different). In particular, the conformal weights can be expressed in dependency of K_c, which will be important for the later discussions.

Using the same arguments, the conformal weights of a LEL can be calculated. As a reference integrable model one can e.g. choose the BARIEV model [93], which is by the way closely related to the Hirsch model. Here, the conformal weights read

$$\Delta^{\pm} = \frac{1}{2} \left(\frac{I}{2\xi_c(Q)} \pm D\xi_c(Q) \right)^2 + N^{\pm} \ . \tag{3.33}$$

The excitations are characterized by (M, D, N): here M labels the number of holes of pairs, D transfers of pairs from one Fermi point to another and $N^{\pm}$ the usual particle-hole excitations. Using $x = 2(\Delta^+ + \Delta^-)$ the correlation function parts read

$$\left\langle \phi_{\Delta^{\pm}}^{\dagger}(r)\phi_{\Delta^{\pm}}(0) \right\rangle = \frac{e^{-i2k_F D}}{r^{2x}} \ . \tag{3.34}$$

In contrast to the Bethe ansatz solutions of the repulsive Hubbard model, the integers (M, D, N) are not restricted.

As an example the non-oscillating density correlation part is given by the excitation $(0,0,1)$, thus $\Delta^{\pm} = 1$ and $\alpha = 2$ (cf. eq. 2.44). The $2k_F$ part is induced by $(0,1,0)$, which implies $\alpha = 2\xi_c^2(Q)$. Identifying

$$K_c = 2\xi_c^2(Q) \tag{3.35}$$

the results (of all correlation functions) again coincide with those of eq. (2.44-2.45) and we can transfer all results to a general LEL (as well as the relevant symmetries are not different).

Up to now, we have only reproduced the $T = 0$ results of sec. 2.2.3 in terms of CFT results, supplied by Bethe ansatz findings. The advantage of this excursus is the extensibility to *finite* temperatures $T > 0$. Here, the CFT predicts the

corr.	k	excitation	α	γ	ref.
Tomonaga-Luttinger liquid					
density	0	$(0,0,0,0,1,0)$	2	$\frac{v_c}{2\pi}$	(a)
density	$2k_F$	$(0,0,\pm1,\pm1,0,0)$	$1+K_c$	$\frac{v_c}{\pi\left(\frac{v_c}{v_s}+K_c\right)}$	(b)
density	$4k_F$	$(0,0,\pm1,0,0,0)$	$4K_c$	$\frac{v_c}{4\pi K_c}$	(c)
spin	0	$(0,0,0,0,0,1)$	2	$\frac{v_s}{2\pi}$	(d)
spin	$2k_F$	$(0,0,0,\pm1,0,0)$	$1+K_c$	$\frac{v_c}{\pi\left(\frac{v_c}{v_s}+K_c\right)}$	(e)
singlet	0	$(2,1,\pm\frac{1}{2},\mp1,0,0)$	$1+\frac{1}{K_c}$	$\frac{v_c}{\pi\left(\frac{v_c}{v_s}+\frac{1}{K_c}\right)}$	(f)
singlet	$2k_F$	$(2,1,\pm\frac{1}{2},0,0,0)$	$K_c+\frac{1}{K_c}$	$\frac{v_c}{\pi\left(K_c+\frac{1}{K_c}\right)}$	(g)
triplet	0	$(2,2,0,0,0,0)$	$1+\frac{1}{K_c}$	$\frac{v_c}{\pi\left(\frac{v_c}{v_s}+\frac{1}{K_c}\right)}$	(h)
triplet	$2k_F$	$(2,2,0,1,0,0)$	$K_c+\frac{1}{K_c}+2$	$\frac{v_c}{\pi\left(2\frac{v_c}{v_s}+\frac{1}{K_c}+K_c\right)}$	(i)

Table 3.1.: Correlation functions of the Tomonaga-Luttinger model, split up into oscillating and non oscillating parts. For temperature $T = 0$ the correlations decay algebraically with critical exponent α. For low finite temperature $T > 0$ an exponential decay is observed with a thermal correlation length $\xi = \gamma/T$. The third column refers to the (lowest) exitation type $(I_c, I_s, D_c, D_s, N_c, N_s)$ which contributes to the respective correlation and determines the conformal weights in eq. (3.29) and (3.30). The last column (ref.) denotes reference labels, which we use later on.

following general form of static correlation functions, where we first consider a TLL [71]:

$$\left\langle \phi^\dagger_{\Delta\pm}(r)\phi_{\Delta\pm}(0) \right\rangle = \left(\frac{2\pi T}{v_c}\right)^{2x_c} \left(\frac{2\pi T}{v_s}\right)^{2x_s} \frac{e^{-4ik_F D_c r}e^{-2ik_F D_s r}}{e^{2\pi T\left(\frac{x_c}{v_c}+\frac{x_s}{v_s}\right)r}} \ . \qquad (3.36)$$

Thus, all correlations asymptotically decay *exponentionally* (in correspondence with eq. (1.50)) with a temperature dependent correlation length

$$\xi = \frac{1}{2\pi\left(\frac{x_c}{v_c}+\frac{x_s}{v_s}\right)T} =: \frac{\gamma}{T} \ . \qquad (3.37)$$

Note, that eq. (3.37) holds for sufficiently *low* temperatures. As an important difference to the $T = 0$ case in sec. 2.2.3, the low temperature behavior depends also on the spin and charge velocities v_c and v_s. Using the eqs. (3.29-3.30) and the identification (3.32), it is thus possible to calculate γ for each thermal correlation length explicitly [25, 94]. We summarize the results in tab. 3.1, referring additionally to the excitation type $(I_c, I_s, D_c, D_s, N_c, N_s)$ which has been considered.

Luther-Emery liquid					
corr. type	k	excitation	α	γ	ref.
density	0	$(0,0,1)$	2	$\frac{v_c}{2\pi}$	(a)
density	$2k_F$	$(0,1,0)$	K_c	$\frac{v_c}{\pi K_c}$	(b)
density	$4k_F$	$(0,2,0)$	$4K_c$	$\frac{v_c}{4\pi K_c}$	(c)
singlet	0	$(1,0,0)$	$\frac{1}{K_c}$	$\frac{v_c K_c}{\pi}$	(d)
singlet	$2k_F$	$(1,1,0)$	$K_c + \frac{1}{K_c}$	$\frac{v_c}{\pi\left(K_c+\frac{1}{K_c}\right)}$	(e)

Table 3.2.: The same as tab. 3.1, but for the Luther-Emery liquid. The exitation types characterized by (M, D, N) are denoted in the third column.

For a LEL eq. (3.37) simplifies to

$$\gamma = \frac{v_c}{2\pi T x} \ . \tag{3.38}$$

Using eq. (3.33) and the identification (3.35) the results obtained for γ are summarized in tab. 3.2. Note, that triplet and spin correlations do not play a role in the low temperature regime due to the spin gap. On the basis of these CFT results we discuss the correlation lengths of the Hirsch model, which is done in the following section.

3.3.2. TMRG Results for Correlation Lengths

A great advantage of the TMRG algorithm is that not only quantities related to the free energy are accessible, but also, through the next-leading eigenvalues of the transfer-matrix, thermal correlation lengths (1.51). As explained in Sec. 3.1.2, the corresponding correlation functions are identified by their quantum numbers $(\Delta N_\uparrow, \Delta N_\downarrow)$. It is even possible to distinguish the contributions of different wave-vectors $k_\alpha = \alpha k_F$ ($\alpha = 0, 2, 4, \ldots$). This will be done in the following to determine the dominant correlations in the different parameter regimes.

First, we check the precision of our TMRG data. For that purpose we choose $X = 0$, which describes a system of free fermions with spin. Here, all correlation lengths can be computed exactly. Due to WICK'S theorem (details are found in appendix C), spin, charge and pair CLs are identically given by

$$\xi^{-1} = 2\mathrm{arsinh}(\pi T/2) \ . \tag{3.39}$$

Fig. 3.13 compares the CLs computed by the TMRG program to exact data. Down to a temperature $T \approx 0.2$ the relative error is shown to be less then 10%. As already mentioned in Sec. 3.1.1 it is important to perform a JWT before applying the TMRG to the bond-charge model. Otherwise, particularly the singlet pair correlations are *not* correctly reproduced by the algorithm.

We now discuss in detail s-s, d-d, sp and tp correlations in the bond-charge model. The low temperature asymptotics have been extensively discussed in
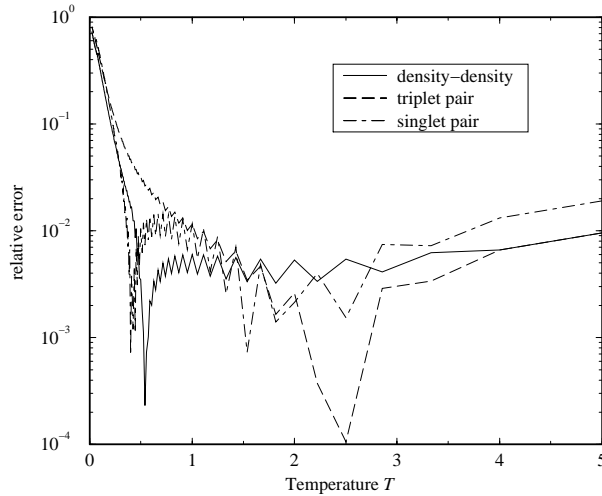
Figure 3.13.: Precision check of various correlation lengths computed by the TMRG algorithm for free fermions. The relative error is plotted as a function of temperature T, showing that the CLs keep reliable for $T > 0.2$.

sec. 3.3.1 and are summarized in tab. 3.1 and 3.2. The results are now used to interpret the correlation lengths, that have been computed with the TMRG algorithm.

We focus on the parameter point $X = 0.5$, where the spin gap is comparatively large for $n \gtrsim 1$. For $T = 0$, the system is then a LEL with dominating superconducting sp correlations due to $K_c > 1$. From the results shown in tab. 3.2 it is expected, that sp correlations should dominate even for finite low temperatures $T > 0$. At zero temperature, close to half-filling a transition to a TLL takes place which exists for all densities $n \lesssim 1$.

Fig. 3.14 shows the (leading) thermal CLs for three different chemical potentials ($\mu = -1, 0.4, 0.6$). The choice of μ covers the TLL ($\mu = -1$) and the LEL phase ($\mu = 0.6$) as well as a point close to the phase transition ($\mu = 0.4$). In these figures we have plotted $\xi \cdot T$ vs. T which allows to determine the low temperature asymptotics. As $\xi = \gamma/T$ for $T \to 0$ (cf. eq. (3.37)), the curves should become linear and intersect the ordinate at γ. According to CFT (see Sec. 3.3.1), the factor γ depends on the spin and charge velocities and the critical exponent K_c. For $\mu = -1$ ($n_0 \approx 0.38$) in fig. 3.14 (a) the system is in the TLL regime. The non-oscillating d-d CL dominates for all temperatures. The leading s-s CL for $T \to 0$ is shown to be incommensurable ($k = 2k_F$), whereas the $k = 0$ part is strongly suppressed and not shown in the figure. Additionally, the $k = 4k_F$ d-d correlation lengths dominate the $k = 2k_F$ d-d and all s-s CLs. This scenario can easily be understood by the fact, that the spin velocity is very small ($v_s \ll v_c$), which can be verified by fig. 3.9. The ratio $v_c/v_s \gg 1$ enters (a) and (e) of tab 3.1, thus these correlations are suppressed for low temperatures. For the same reason, the tp correlation length is crossed over by the leading incommensurable sp correlation length at low temperatures, cf. (h) of tab. 3.1. The inset of fig. 3.14 (a) depicts the wave-vectors k_F. We have also
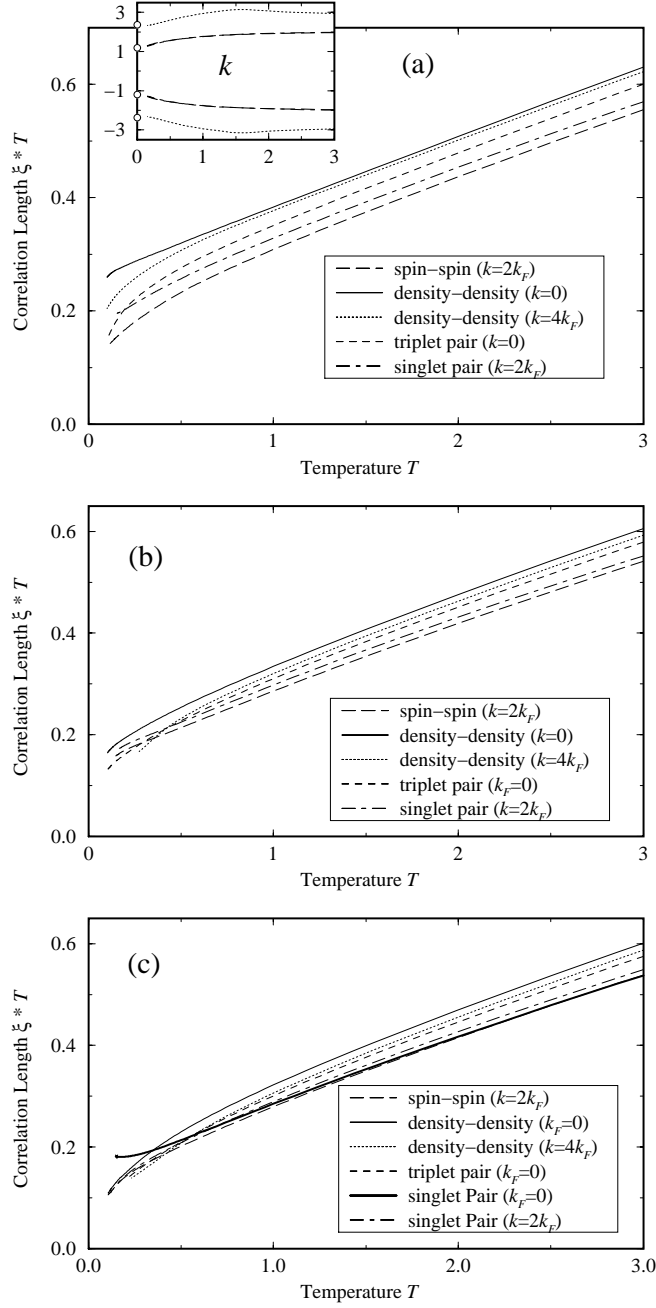
Figure 3.14.: Plot of the leading d-d, s-s, sp and tp correlation lengths ξ for $X = 0.5$ and (a) $\mu = -1$, (b) $\mu = 0.4$ and (c) $\mu = 0.6$. The corresponding densities $n_0 = n(T \to 0)$ read (a) $n_0 \approx 0.38$, (b) $n_0 \approx 0.88$ and (c) $n_0 = 1.19$. The diagrams show the respective correlation $\xi \cdot T$ as a function of T. As an example, the inset of (a) depicts the wave-vectors k of the oscillating CLs. The circles ($\circ$) correspond to the $T \to 0$ limit of $k = 2k_F$ and $k = 4k_F$ with $k_F = n\pi/2$.
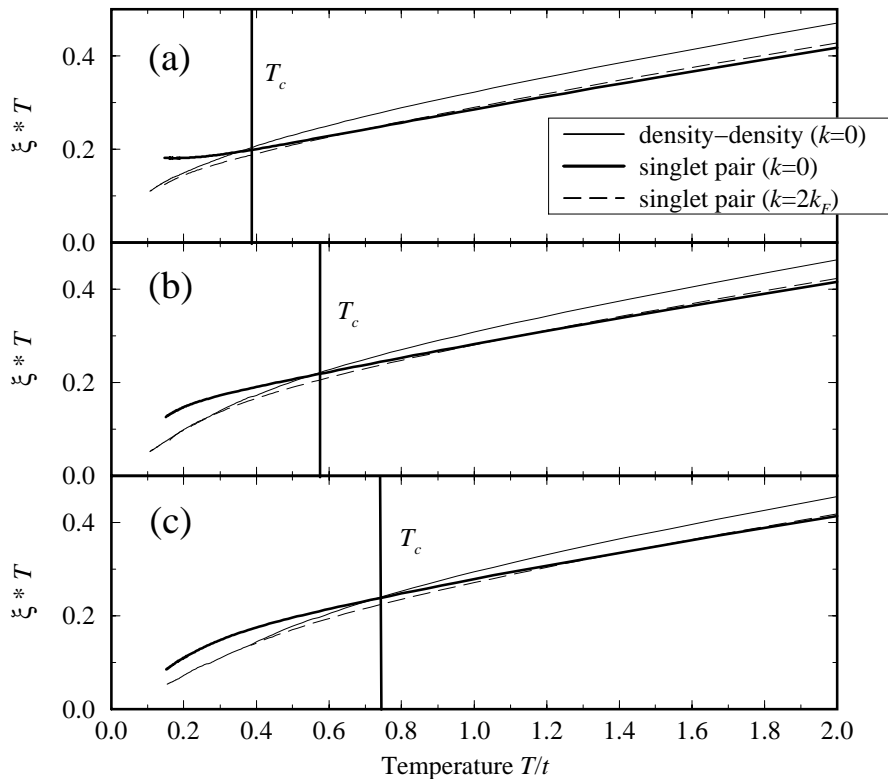
Figure 3.15.: Crossing phenomena of density-density ($k = 0$) and singlet pair ($k = 0, 2k_F$) correlation lengths for various chemical potentials (a) $\mu = 0.6$ (b) $\mu = 0.8$ and (c) $\mu 1.0$. The diagrams plot the particular correlation length $\xi \cdot T$ as a function of temperature T. The corresponding densities $n_0 = n(T \to 0)$ are given by (a) $n_0 \approx 1.21$ (b) $n_0 \approx 1.92$ (c) $n_0 \approx 1.99$.

plotted the $T \to 0$ values of $2k_F$ and $4k_F$ with $k_F = \frac{\pi}{2}n$ which agree perfectly with the TMRG data.

The case $\mu = 0.4$ ($n_0 \approx 0.88$) shown in fig. 3.14 (b) also falls into the TLL regime, but is situated close to the phase transition to the LEL. The CLs generally get smaller, because the charge velocity v_c is decreased (see fig. 3.9). Note, that the crossing phenomena of CLs become very rich close to the transition.

A crossover of sp and d-d correlations at finite temperature $T_c \approx 0.5$ is observed in fig. 3.14 (c) for $\mu = 0.6$ ($n_0 \approx 1.19$). And in contrast to the latter cases, the leading sp CL is shown to be commensurable. This agrees with the predictions of tab. 3.2, if $K_c > 1$ is assumed.

The crossing temperature T_c increases for higher fillings. This is demonstrated by fig. 3.15, which shows only the leading d-d and sp correlation lengths for $\mu = 0.6, 0.8, 1.0$. Note, that the CLs in fig. 3.14 (c) and fig. 3.15 do not show asymptotic $\frac{1}{T}$ behaviour for the achievable temperatures, which may indicate logarithmic corrections.

4. Stochastic Models

4.1. Introduction

As already mentioned in the preface, the second part of the present thesis is dedicated to the study of *non-equilibrium physics*. As a matter of fact, the thermal equilibrium, where theories are quite well elaborated, is in nature more an exception than a rule. Prominent examples are found in pure physical contexts, but also in many interdisciplinary fields and reach from dynamic growth processes [95], chemical diffusion [19], evolution of forest fires [96] or diseases [97], modelling traffic on a highway [20] to phenomena like self organized criticality [98]. By far this list is not exhaustive. Like in the quantum case, non-equilibrium phenomena – especially in one space dimension – show interesting non-trivial collective behavior and strong correlations.

However, the physics of non-equilibrium systems are a comparatively modern research field and by far not as well understood as equilibrium ones. Our research concentrates on so called *stochastic models*. A generic choice of such models stands to reason, if the microscopic dynamics of a process are not known in detail. But nevertheless from empirical considerations informations about transition probabilities are available. As already suggested by its name, stochastic models inherit these probabilities by stochastic (microscopic) dynamics.

The dynamic evolution of a large class of (Markov) stochastic models can be described by a so-called *master equation* [99]. During the last decades a lot of progress has been made here, which succeeded from a close formal analogy between stochastic and quantum models. The master equation can be mapped onto a Schrödinger's equation in imaginary time, which was first realized by Alexander and Holstein for the symmetric exclusion process [21]. Alcaraz et. al extended the idea to so-called reaction-diffusion processes [100], which represent a large, intensively studied class of stochastic models.

Reaction-diffusion models originate from chemical reactions with thermal diffusion. Meanwhile they have become something like a prototype for stochastic models. Their formal analogy to quantum systems allows to transfer various techniques like the Bethe ansatz, free fermion methods [101] or the matrix product ansatz [102].

Especially interesting is that also concepts of criticality, universality and (modified) versions of conformal invariance and scaling can be adapted to stochastic models. In spite of this remarkable progress, exact results still extremely rare. One of the most important universality classes, which occurs in case of *absorbing state* transitions, is *directed percolation* (DP) [103, 104]. We consider a typical example for DP to elucidate what is meant by an absorbing state transition,

namely the spreading of an infectious disease. Suppose, that a certain percentage of a population is infected. Each individual may recover from the disease or infect others. Thus, two so-called stationary "states" of the population are possible after a long time has passed by. Depending on the infection rate p, either the disease is completely eliminated $p < p_c$ (absorbing phase) or the disease is exuberant $p > p_c$ (active phase). Thus we have a *non-equilibrium phase transition* of two physically different regimes, which is illustrated by fig. 4.1.
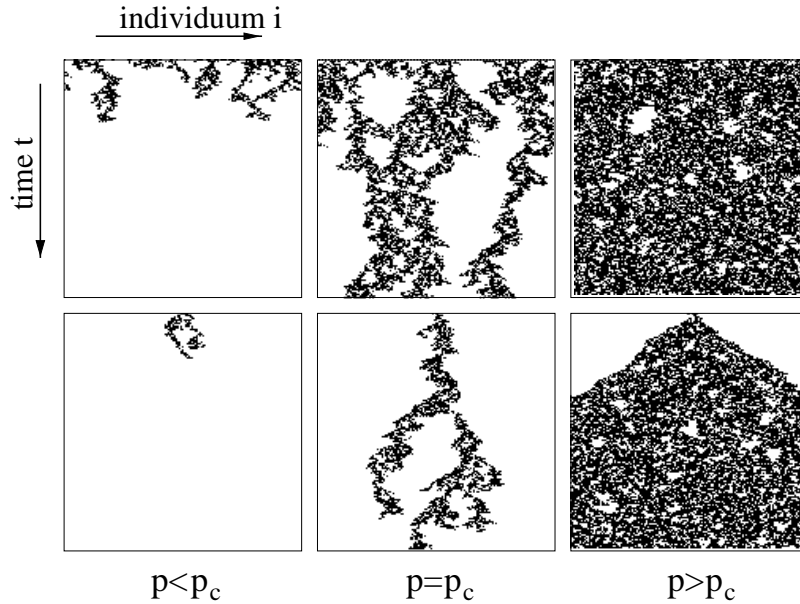
Figure 4.1.: The figures, taken from [105], sketch the dynamic evolution of the infectious disease in time t. Infected individuals i are marked with dots, where cured ones are noted with a space. In the upper three figures, a certain percentage of individuals are already infected. Depending on the infection rate p, the disease spreads ($p > p_c$) or is dammed ($p < p_c$). The lower figures contain the same process, but only one individual (like a seed of the spreading) is infected. In between at $p = p_c$ we obtain a phase transition point.

Even if the DP universality class is generic for a huge class of almost simple models, it is amazing that none of them can be solved exactly. Consequently critical exponents, which i.e. characterize the algebraic decay of correlation functions, can not be determined rigorously. Moreover, the number of universality classes is by far not completely known.

A quite unfavorable disadvantage of non-equilibrium studies is the lack of experimental realizations [106]. Most of the "experimental" evidence is given by computer simulations, which are widely known as Monte-Carlo simulations (MCS). This technique means nothing else than simulating a quite huge number of concrete realizations (also called *samples*) of the stochastic process. Then, all samples have to be averaged to predict the physical properties.

But particularly critical phenomena are sophisticated problems of MCS. As criticality is a property of a long-time stochastic evolution, simulations can

get extremely large-scaled. Additionally, quite large system sizes have to be simulated to interpolate physical properties of the thermodynamic limit.

Alternatively numerical methods to investigate stochastic systems are rare. Recently, CARLON et al. suggested a stochastic DMRG algorithm to study stationary state properties [107]. The aim of this thesis is to introduce a new method, based on the "classical TMRG" of section 1.2, to study the *dynamics* of stochastic models.

But before we step into the details of the *stochastic TMRG* in chapter 5, we briefly review the theoretic background of stochastic systems, following [105]. Section 4.2 sketches the formal correspondence of quantum and stochastic models. In sec. 4.4 we introduce a general class of stochastic models, namely reaction-diffusion processes. Two particular ones, namely the branch-fusion (BFP) and the diffusion-annihilation (DAP) process, are later on investigated within our stochastic TMRG studies.

4.2. The Master Equation and Quantum Formalism

We consider a stochastic process with many particles in d space dimensions. An additional dimension is in a natural manner the time, thus stochastic models are said to be of dimension $d+1$. In general the spatial and time degrees of freedom can either be continuous or discrete. As our aim is to use statistical methods to model stochastic processes, particles are considered to "live" on a discrete lattice. Depending on discrete or continuous time we distinguish *synchronous* or *asynchronous* dynamics.

The complete description of a stochastic model is provided by the dynamic evolution of the *probability distribution*

$$P_t : \mathcal{S} \to [0, 1] \tag{4.1}$$

where t labels the time and $\mathcal{S}$ is the spatial *configuration space* of the lattice. We restrict ourselves to one-dimensional *stochastic chains* of length L, where each site has a certain number n of degrees of freedom, thus

$$\mathcal{S} = \{1, \dots, n\}^{\otimes L}. \tag{4.2}$$

Consequently, $P_t(s)$ expresses the probability of a configuration $s \in \mathcal{S}$ at time t.

To introduce a quantum style formalism for stochastic models, we interpret P_t as a vector (or stochastic state)

$$\big|P_t\big\rangle = \sum_{s \in \mathcal{S}} P_t(s)\big|s\big\rangle \in \mathbb{R}_+^{|\mathcal{S}|} \tag{4.3}$$

where $\big|s\big\rangle$ has been identified as an (orthogonal) basis. $\big|P_t\big\rangle$ has to be normalized in the sense that the sum of all probabilities $P_t(s)$ results in unity

$$1 = \sum_{s \in \mathcal{S}} P_t(s) = \big\langle 1\big|P_t\big\rangle =: \|P_t\| \tag{4.4}$$

where we have introduced the vector

$$\langle 1| = \sum_{s \in \mathcal{S}} \langle s| \tag{4.5}$$

and a canonical norm $\|\cdot\|$. The physically reasonable "probability vectors" therefore are situated on the unity sphere $S_{\|\cdot\|}$.

4.2.1. Asynchronous Dynamics

Stochastic models in continuous time evolve by *asynchronous* dynamics. A transition from a configuration s to s' occurs spontaneously with a *transition rate* $w_{s \to s'}$. For sufficiently large system sizes, the dynamics (of a large class of models) can be described by the master equation, namely

$$\partial_t P_t(s) = \sum_{s' \in \mathcal{S} \setminus \{s\}} \left(w_{s' \to s} P_t(s') - w_{s \to s'} P_t(s) \right) . \tag{4.6}$$

The master equation is a kind of accounting equation, where each term is a balance of gained and loosed probability flow. Note, that the transition rates w do *not* depend on time. In other words: we assume that the stochastic process does not have any "memory" about the past, which characterizes so-called MARKOV processes.

Defining a *stochastic Hamiltonian*

$$\langle s'|H|s \rangle := -w_{s \to s'} + \delta_{ss'} \sum_{s'' \in \mathcal{S}} w_{s \to s''} \tag{4.7}$$

the master equation can be written in the compact representation

$$\partial_t |P_t\rangle = -H|P_t\rangle . \tag{4.8}$$

Eq. (4.8) obviously has the shape of a SCHRÖDINGER equation in imaginary time. So this is the point, where an analogy of stochastic and quantum models has been established. It is important to notice, that in contrast to a quantum Hamiltonian, H is in general *not hermitian*. This expresses the fact that the stochastic model is generically a non-equilibrium process and does not fulfill the detailed balance condition.

A formal solution of the master equation is given by

$$|P_t\rangle = \mathrm{e}^{-tH}|P_0\rangle \tag{4.9}$$

where P_0 denotes the *initial* probability distribution at time $t = 0$. The infinite time limit $t \to \infty$ is called the stationary limit and $|P_\infty\rangle$ the stationary state of the stochastic process. Note, that $|P_\infty\rangle$ may depend on the initial state $|P_0\rangle$ if the process is not ergodic. Stationarity of $|P_\infty\rangle$ yields

$$-H|P_\infty\rangle = \partial_t |P_\infty\rangle = 0 . \tag{4.10}$$

As a consequence $|P_\infty\rangle$ is an eigenvector of H of eigenvalue 0 and corresponds to the ground state in a quantum picture. By the way, the corresponding

left "ground state" eigenvector is trivially given by $\langle 1|$, which expresses the normalization of $|P_t\rangle$

$$\langle 1|H|P_t\rangle = -\langle 1|\partial_t|P_t\rangle = -\partial_t \langle 1|P_t\rangle = -\partial_t 1 = 0 . \tag{4.11}$$

Typically, the dynamics of stochastic models are investigated by (local) averages

$$\langle O \rangle (t) = \sum_{s \in \mathcal{S}} O(s) P_t(s) . \tag{4.12}$$

Introducing the operator O with diagonal elements $O(s) = \langle s|O|s\rangle$, the averages read in a vector notation

$$\langle O \rangle (t) = \langle 1|O|P_t\rangle = \langle 1|O \cdot \mathrm{e}^{-tH}|P_0\rangle . \tag{4.13}$$

By eq. (4.13) one can show that the "first excitations" of the stochastic Hamiltonian H characterizes the long time asymptotics. Representing

$$|P_0\rangle = \sum_{\lambda} a_\lambda |\lambda\rangle \tag{4.14}$$

by (complex) eigenvectors $|\lambda\rangle$ of H, eq. (4.13) reads

$$\langle O \rangle (t) = \sum_{\lambda} a_\lambda \mathrm{e}^{-tE_\lambda} \langle 1|O|\lambda\rangle . \tag{4.15}$$

Therefore the "energy" gap $\Re E_1 - E_0 = \Re E_1$ determines the exponentially decaying long-time asymptotics of $\langle O \rangle (t)$. Imaginary parts $\Im E_1$ lead to oscillatory effects, which indeed are experimentally observed [108]. If the gap closes, the stochastic system gets critical and $\langle O \rangle (t)$ crossovers to an algebraic behavior.

4.2.2. Synchronous Dynamics

In the discrete time case, the stochastic model is *synchronously* updated in discrete steps Δt. The master equation now reads

$$|P_{t+\Delta t}\rangle = \mathcal{T}|P_t\rangle . \tag{4.16}$$

$\mathcal{T}$ is called *stochastic transfer-matrix* and is defined by

$$\langle s'|\mathcal{T}|s\rangle = p_{s \to s'} . \tag{4.17}$$

Here, $0 \leq p_{s \to s'} \leq 1$ are transition probabilities, not rates

$$w_{s \to s'} = \lim_{\Delta t \to 0} \frac{p_{s \to s'}}{\Delta t} \tag{4.18}$$

like in the continuous case.

There are various kinds of synchronous update possibilities (parallel update, sub-lattice-parallel update, etc). Research studies verified that different dynamics are not necessarily equivalent [109]. Therefore the question has extensively been discussed, which dynamic is more "realistic", in particular in respect to continuous or discrete dynamics. However, synchronous dynamics are much easier to realize by Monte-Carlo simulations. In contrast, asynchronous dynamics are favored in theoretical studies due to the Hamilton formalism.

4.3. Non-Equilibrium Criticality and Universality Classes

One of the most challenging phenomena of stochastic systems are phase transitions (especially those to absorbing phases) and criticality. Similar to equilibrium physics, criticality is characterized by critical exponents that describe the *algebraic* decay of e.g. correlation functions, etc.

Suppose now a stochastic model, which is controlled by one parameter p only and exhibits a critical phase transition point p_c, almost like presented in fig. 4.1. In the non-critical regime correlations decay exponentially with a certain correlation length, which expresses characteristic microscopic length scales. In non-equilibrium physics, two types of correlation lengths have to be distinguished, corresponding to a *spatial* $\xi_\perp$ and *temporal* length scale $\xi_\parallel$. Their physical meaning is nicely visualized in fig. 4.2.
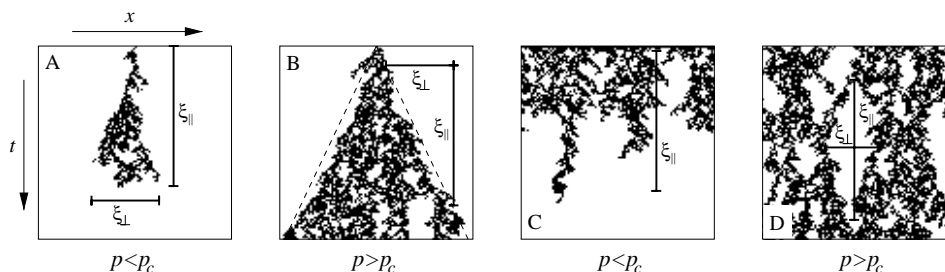
Figure 4.2.: Interpretation of the correlation length, taken from [105]. Fig. (A) and (B) depict the dynamic evolution of one seed in an active ($p > p_c$) and absorbing ($p < p_c$) phase. In the absorbing phase $\xi_\parallel$ and $\xi_\perp$ describe the broadening of the spreading, before the "active particles" vanish. Contrary, in the active phase the slope of the "light cone" is characterized by $\xi_\parallel/\xi_\perp$. Fig. (C) and (D) refer to the situation of a general initial state.

Close to criticality $p \sim p_c$ the scales $\xi_\perp$ and $\xi_\parallel$ diverge

$$\xi_\perp \sim |p - p_c|^{-\nu_\perp} \quad \text{and} \quad \xi_\parallel \sim |p - p_c|^{-\nu_\parallel} \ , \tag{4.19}$$

where we have introduced two critical exponents, which generically do not coincide $\nu_\perp \neq \nu_\parallel$. The quotient $z = \nu_\parallel/\nu_\perp$ is usually called *dynamic exponent* and e.g. is related to the slope of the cone which evolves in fig. 4.2 (B).

A typical order parameter is the local density of particles $n(t)$, which distinguishes e.g. absorbing ($n(\infty) = 0$) and active phases ($n(\infty) \neq 0$). Close to criticality, in the active regime, one finds

$$n(\infty) \sim (p - p_c)^\beta \tag{4.20}$$

where we have defined the critical exponent β.

In order to complete the list of *independent* critical exponents we consider the probability $\mathcal{P}(t)$, that a cluster grown from a single seed (cf. fig. 4.2 (A) and

(B)) remains active after t time steps. $\mathcal{P}(\infty)$ scales close to criticality by an exponent β'

$$\mathcal{P}(\infty) \sim (p - p_c)^{\beta'} \ . \tag{4.21}$$

It is widely accepted that four exponents $(\beta, \beta', \nu_\perp, \nu_\parallel)$ determine the non-equilibrium universality classes. Exponents of other physical properties can be obtained by *scaling*, which is a well known technique also in the equilibrium case.

As an example, the asymptotic dynamic evolution of $n(t)$ and $\mathcal{P}(t)$ for $t \to \infty$ at criticality $p = p_c$ reads

$$n(t) \sim t^{-\alpha} \quad \text{and} \quad \mathcal{P}(t) \sim t^{-\delta} \tag{4.22}$$

where the critical exponents are given by $\alpha = \beta/\nu_\parallel$ and $\delta = \beta'/\nu_\perp$.

The most prominent universality class of DP, which was already mentioned in sec. 4.1 , has been extensively studied by various numerical and pertubative approaches. The exponents have been calculated with high precision, which we summarized in tab. 4.1.

crit. exponent	DP [110]	PC [111]
β	0.276486(8)	0.92(2)
β'	0.276486(8)	0.92(2)
$\nu_\perp$	1.096854(4)	1.83(3)
$\nu_\parallel$	1.733847(10)	3.22(6)

Table 4.1.: Best known results of critical exponents of the directed-percolation (DP) and the parity-conserving (PC) class.

A fascinating property of DP is its robustness to the microscopic dynamics of the model. This property led JANSSEN and GRASSBERGER to the conjecture that absorbing phase transitions with certain general properties (symmetry, range of interaction, etc.) [112, 113] generically fall into the DP class.

Critical exponents of other universality classes are much less accurately accessible. As an example we mention the parity-conservation (PC) [111], see tab. 4.1. Here the best known results exhibit errors of a few percents. The problem, why even huge MCS can not fix the exponents more precisely is found in the *critical slowing-down*. The crossover to algebraic behavior of e.g. the order parameter $n(t)$ can occur at extremely large time-scales. MCS at such scales suffer from strong fluctuations, such that a huge number of samples have to be generated. A popular example, where MCS can not unambiguously determine the universality class, is the pair-contact process with diffusion (PCPD)

$$2A \to 3A, \quad 2A \to \emptyset, \quad \text{and diffusion} \quad A\emptyset \leftrightarrow \emptyset A \ . \tag{4.23}$$

A recent stochastic DMRG study of CARLON et. al [114] initiated intensive discussions, whether the PCPD exhibits a new universality class or is just DP [115, 116]. The problem is, that the crossover to critical behavior occurs at

such huge time scales, that the algebraic behavior can not really be identified in simulations.

Alternative methods apart from MCS are therefore demanded. The stochastic TMRG presented in the chapter 5 is considerable step towards a numerical non-simulation method for the study of stochastic models.
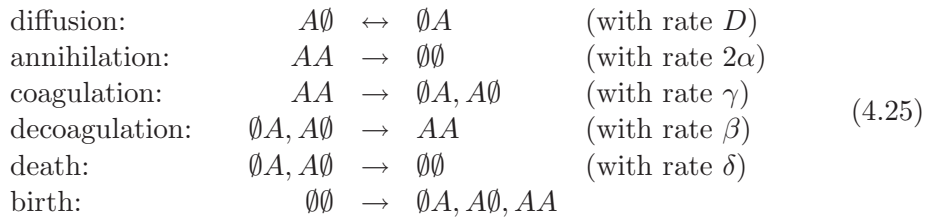
4.4. Reaction-Diffusion Models

As already mentioned, reaction-diffusion processes (RDP) originate from chemical reactions of various particle species (usually denoted by letters $A, B, C, \dots$) with thermal diffusion.

The reactions we consider are modeled on a one-dimensional lattice with only *one* particle species. Thus each site can either be empty $\emptyset$ or occupied A. As a natural assumption the particles react, if they are next-neighbors. Therefore the stochastic Hamiltonian reads

$$H = \sum_i h_{i,i+1} \; . \tag{4.24}$$

In general, a RDP (with one particle A) can exhibit the following reactions:

$$
\begin{array}{llll}
\text{diffusion:} & A\emptyset & \leftrightarrow & \emptyset A & \text{(with rate } D) \\
\text{annihilation:} & AA & \rightarrow & \emptyset\emptyset & \text{(with rate } 2\alpha) \\
\text{coagulation:} & AA & \rightarrow & \emptyset A, A\emptyset & \text{(with rate } \gamma) \\
\text{decoagulation:} & \emptyset A, A\emptyset & \rightarrow & AA & \text{(with rate } \beta) \\
\text{death:} & \emptyset A, A\emptyset & \rightarrow & \emptyset\emptyset & \text{(with rate } \delta) \\
\text{birth:} & \emptyset\emptyset & \rightarrow & \emptyset A, A\emptyset, AA &
\end{array} \tag{4.25}
$$

We restrict ourselves to processes, where particles can not spontaneously be created. Then the local stochastic interaction yields

$$
h_{i,i+1} = \begin{pmatrix}
0 & -\delta & -\delta & -2\alpha \\
0 & D+\delta+\beta & -D & -\gamma \\
0 & -D & D+\delta+\beta & -\gamma \\
0 & -\beta & -\beta & 2(\alpha+\gamma)
\end{pmatrix} \; . \tag{4.26}
$$

By different ways of choosing the transition rates $\alpha, \beta, \delta, \gamma$ one can generate a variety of diffusive models ($D \neq 0$).

Two special RDP will be of interest in the present thesis, the *diffusion-annihilation* (DAP) and *branch-fusion* (BFP) process, which we explicate in the following sections.

4.4.1. The Diffusion-Annihilation Process

The *diffusion-annihilation process* (DAP)

$$2D = \alpha, \quad \beta = \gamma = \delta = 0 \tag{4.27}$$

is an example of an exactly solvable model. The concept of the solution is to map the DAP onto an XY Heisenberg chain in magnetic field [117]. Both

models are connected by the same quantum group $SU(1|1)$ symmetry, which facilitates to transfer the Bethe ansatz solution of the XY chain.

In the framework of developing a TMRG algorithm for stochastic models the DAP is an ideal model for checking numerical by exact data. The dynamical evolution of the density of particles A is given by the simple expression

$$n(t) = \frac{1}{2}\left(I_0(4Dt) + I_1(4Dt)\right) e^{-4Dt} . \qquad (4.28)$$

I_0 and I_1 denote the conventional modified BESSEL functions

$$I_n = \sum_k \frac{\left(\frac{x}{2}\right)^{n+2k-2}}{k!\,\Gamma(n+k)} \quad \text{where} \quad \Gamma(x) = \int_0^\infty e^{-t} t^{x-1} \mathrm{d}t . \qquad (4.29)$$

The asymptotic decay of the density $n(t)$ reduces to be a power law decay

$$n(t) \sim t^{-1/2} \qquad (4.30)$$

with a critical exponent $\alpha = 1/2$. Thus, the DAP is critical for any diffusion constants D. Phase transitions do not occur. Actually we notice that there is a remarkable experimental realization, which verifies the critical exponent $1/2$ by the kinetics of laser induced excitons in tetramethylammonium manganese trichloride [118].

4.4.2. The Branch-Fusion Process

The *branch-fusion process* (BFP)

$$D = 2\alpha = \gamma = \delta =: 1-p, \quad \beta =: p \qquad (4.31)$$

is a simple one parameter model, that exhibits a non-equilibrium phase transition from an active to an absorbing phase. The BFP is not exactly solvable, but Monte-Carlo simulations [119, 120] and stochastic DMRG computations [107] are available.

The dynamics of the BFP principally coincide with the schematic plots of fig. 4.1. For $p < p_c$ the BFP exhibits an absorbing phase, where the stationary state is given by $\left|P_\infty\right\rangle = \left|\emptyset\emptyset\cdots\emptyset\right\rangle$. An active phase $n(t) \neq 0$ with non-trivial $\left|P_\infty\right\rangle$ occurs for $p > p_c$. The transition point

$$p_c \approx 0.84036(1) \qquad (4.32)$$

has been calculated e.g. by DMRG [107] and falls into the DP universality class. Both models, the DAP and the BFP, are studied in the chapter 6 in the framework of the newly introduced *stochastic light-cone TMRG* algorithm.

5. Stochastic TMRG

As shown in the last section, quantum and stochastic systems exhibit a close formal analogy, which has been used to transfer various methods (Bethe ansatz, matrix product ansatz, stochastic DMRG, etc.) from equilibrium to non-equilibrium physics. Thus it seems quite natural to apply the TMRG algorithm also to stochastic systems.

But a lot of significant differences appear by looking at the details. To differ between the quantum and stochastic case, the TMRG we describe in this section is called *stochastic TMRG*. This method was first used in [31, 121] as a feasibility study, applied to the DOMANY-KINZEL cellular automaton. It was shown, that the TMRG allows precise estimates of phase boundaries and critical exponents of a discrete time model. Following works of ENSS and SCHOLLWÖCK [122, 123] investigated theoretic properties of the stochastic transfer-matrix, focussing on the choice of an adequate density-matrix.

In this section we describe in detail the basic ideas of the stochastic TMRG according to [31, 121, 122, 123]. But even though the stochastic TMRG seems to be a promising new method at first glance, we will discuss why inherent numerical problems limit its practical use.

5.1. The Stochastic TMRG Algorithm

We focus now on a stochastic TMRG algorithm for *continuous* time models. An adaption to discrete time is straight forward [31, 121]. Our starting point is the calculation of the local density (see eq. (4.13))

$$n(t) = \langle 1 | n \cdot \mathrm{e}^{-t \cdot H} | P_0 \rangle \ . \tag{5.1}$$

We assume that the stochastic Hamiltonian H consists of NN interactions only

$$H = \sum_i h_{i,i+1} \tag{5.2}$$

and consider the (thermodynamic) limit $L \to \infty$ of the stochastic chain.

In analogy to the quantum case presented in chap. 1, first a Trotter-Suzuki decomposition of the time evolution operator $\mathrm{e}^{-t \cdot H}$ is performed. Thereby, the 1D stochastic chain is mapped onto a 2D model of classical spins, which is shown in figure 5.1. The spatial dimension L of the stochastic process is expanded by a virtual Trotter dimension $M = t/\Delta t$. M thus corresponds to the time direction, which is split up into discrete time steps Δt.
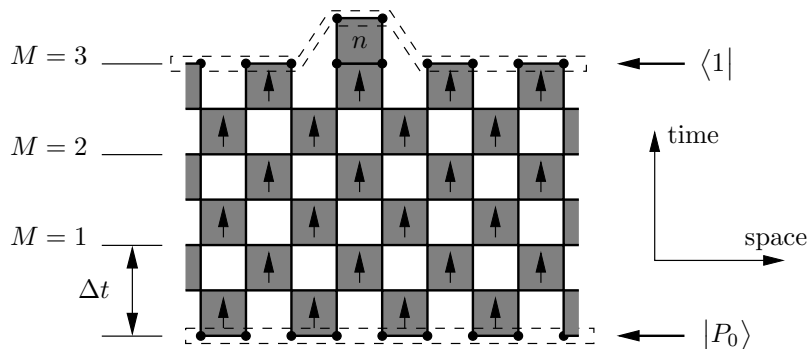
Figure 5.1.: Trotter-Suzuki decomposition of $3\Delta t$ time steps. The resulting 2D lattice consists of local plaquette interactions τ and is infinitely extended in space direction. The dimension of the time direction is finite and the boundary conditions are fixed by $\langle 1|$ and $|P_0\rangle$.

The plaquette interactions of the lattice are given by

$$(\tau)^{l_1 l_2}_{r_1 r_2} = \langle l_2 r_2 | e^{-\Delta t \cdot h} | l_1 r_1 \rangle = \begin{matrix} l_2 \quad r_2 \\ \boxed{\uparrow} \\ l_1 \quad r_1 \end{matrix} \qquad \text{with} \quad l_i, r_i \in \{1 \ldots n\} \ , \qquad (5.3)$$

where n (see sec. 4.2) labels the number of local states. The pictorial representation in (5.3) is chosen differently from eq. (1.32), which alludes to the fact, that $h_{i,i+1}$ is not hermition. The plaquettes physically describe the transition propabilities of two sites in a (discrete) time step Δt. Strictly speaking, the 2D lattice is only an approximation of the 1D continuous time model, because the Trotter-Suzuki decomposition discretizes time. But like in eq. (1.25) the error made enters of the order $\mathcal{O}(\Delta t^2)$ into the computation of $n(t)$. Thus, Δt has to be chosen sufficiently small (e.g. $\Delta t = 0.05$).

As an important difference to the quantum case the classical lattice has *fixed*, not periodic boundary conditions in Trotter direction, determined by the vectors $\langle 1|$ and $|P_0\rangle$. The initial vector $|P_0\rangle$ is assumed to have a "local" structure

$$|P_0\rangle = |p_1\rangle \otimes |p_2\rangle \otimes \cdots \otimes |p_L\rangle \qquad (5.4)$$

where $|p_i\rangle$ is the probability distribution of one site. Typically we choose

$$|p_i\rangle = \frac{1}{n} \sum_{s=1}^{n} |s\rangle \qquad (5.5)$$

which generates an unbiased distribution $|P_0\rangle$, i.e. each local state has the same probability. The vector $\langle 1|$ has the local structure

$$\langle 1| = \langle 1_1| \otimes \langle 1_2| \otimes \cdots \otimes \langle 1_L| \ , \quad \text{with} \quad \langle 1_i| = \sum_{s=1}^{n} \langle s| \ . \qquad (5.6)$$

Due to eq. (5.5) and (5.6) the boundary sites are simply summed out, where the summation induced by $|P_0\rangle$ corresponds to a weighted sum.

In order to solve the 2D classical model we use again a transfer matrix approach. The transfer-matrices T_M and $T_M(A)$ used in the quantum case (sec. 1.2) have to be modified by the fixed boundary conditions, e.g.

$$(T_M)^{l_1 \dots l_{2M-1}}_{r_1 \dots r_{2M-1}} = \sum_{r_0 l_{2M} m_0 \dots m_{2M}} p_{m_0} \, p_{r_0} \prod_{k=1}^{M} (\tau)^{l_{2k-1} m_{2k-1}}_{l_{2k} m_{2k}} \, (\tau)^{m_{2k-2} r_{2k-2}}_{m_{2k-1} r_{2k-1}} \, , \quad (5.7)$$

where $p_i = \langle i | p \rangle$. As an example, the transfer-matrices of $M = 3$ (cf. figure 5.1) have the shape

$$T_M = \qquad \text{and} \quad T_M(A) = \qquad . \qquad (5.8)$$

The bullets represent the indices $r_1 \dots r_{2M-1}$ and $l_1 \dots l_{2M-1}$ of the right and left vector space of T_M. Note, that the indices marked by the shaded bullets are summed out according to the boundary conditions given by $\langle 1 |$ and $|P_0\rangle$. Thereby, the local density $n(t)$ in the thermodynamic limit $L \to \infty$ can be calculated by

$$n(t) = \langle \Lambda_0^L | T_M(n) | \Lambda_0^R \rangle \, . \qquad (5.9)$$

$|\Lambda_0^R\rangle$ and $\langle \Lambda_0^L |$ are the left and right eigenvector of the leading eigenvalue Λ_0 of T_M. Compared to (1.49) Λ_0 does not appear in (5.9), because it can be shown that $\Lambda_0 = 1$, cf. section 5.2.

The computation of $n(t)$ for an arbitrary time $t = M \cdot \Delta t$ necessitates an increasement of the Trotter number M. This can be done numerically by a TMRG algorithm, but compared to the quantum case in sec. 1.2 a number of modifications are necessary:

1. The first difference appears due to the open boundary conditions in Trotter direction. But this is rather an advantage than a disadvantage. The dimensions of the system and environment block S and E are reduced, as no indices at the edges of T_M are necessary. These were necessary in the quantum case to periodically close the transfer-matrix.

2. A disadvantage is the lack of symmetry of the local plaquettes τ. As an effect, the environment E can generically not be constructed from the system block. Additionally, stochastic models do rarely show local conservation laws. All these technical details decrease drastically the computation time of the algorithm.

3. A crucial difference is found in the density-matrix projection. The asymmetric density-matrix, used in the quantum case, turns out to be completely useless in the stochastic case. This first empirical observation in [31, 121] can be explained analytically. As we show in the next section, the asymmetric density-matrix reduces in the stochastic case to a pure projector. Such a projector neglects correlations of the model, which is undesired in a DMRG algorithm. A better choice for stochastic models is the symmetrized version

$$\rho = \text{tr}' \left(\left| \Lambda_0^L \right\rangle \left\langle \Lambda_0^L \right| + \left| \Lambda_0^R \right\rangle \left\langle \Lambda_0^R \right| \right) \ . \tag{5.10}$$

5.2. Properties of the Stochastic Transfer-Matrix

Even if the stochastic TMRG method looks closely similar to the quantum case, various properties of the stochastic transfer-matrix are different. The key idea is that correlation lengths in the 2D lattice are limited by a *causality mechanism*, which we describe now in detail.

The local stochastic transfer-matrix τ obeys probability conservation, i.e. the probability of ending up in any state is unity. As an effect, τ trivializes by summing out the "future" indices

$$\forall l_1, r_1 : \sum_{l_2 r_2} (\tau)_{r_1 r_2}^{l_1 l_2} = 1, \qquad \begin{array}{c} \Sigma l_2 \ \ \Sigma r_2 \\ \text{(diagram)} \\ l_1 \ \ \ r_1 \end{array} = \begin{array}{c} \\ \text{(diagram)} \\ l_1 \ \ \ r_1 \end{array} \ . \tag{5.11}$$

Equation (5.11) shows an additional pictorial illustration of the "trivialization mechanism" which we use later on for visualizing the mathematical structure of the 2D lattice.

We will show next that the the property (5.11) already determines the spectrum of the stochastic transfer-matrix T_M. For the proof we first deduce

$$\text{tr}\, T_M = 1 \tag{5.12}$$

and

$$\forall k \geq 2M - 1 : T_M^{2M-1} = \left| \Lambda_0^R \right\rangle \left\langle \Lambda_0^L \right| = T_M^k, \tag{5.13}$$

i.e. that sufficiently large powers of T_M reduce to an outer product of left and right eigenvectors of Λ_0. This is an important difference to quantum TMRG, where only the limit $k \to \infty$ shows a similar property. For simplicity, the proofs are given exemplarily for particular Trotter numbers M in a pictorial way. A generalization to arbitrary M can be done analogously.

Figure 5.2 demonstrates that performing the trace of T_M is equivalent to T_M being rolled up on a cylinder. Hence, using (5.11) all plaquette interactions trivialise and therefore $\text{tr}\, T_M = 1$.

Figure 5.3 visualizes for the case $M = 2$ the lattice structure of powers of transfer-matrices T_M^1, T_M^2, T_M^3 and T_M^4. It is shown step by step that a number of plaquettes trivialize due to (5.11). The corresponding lattice decouples
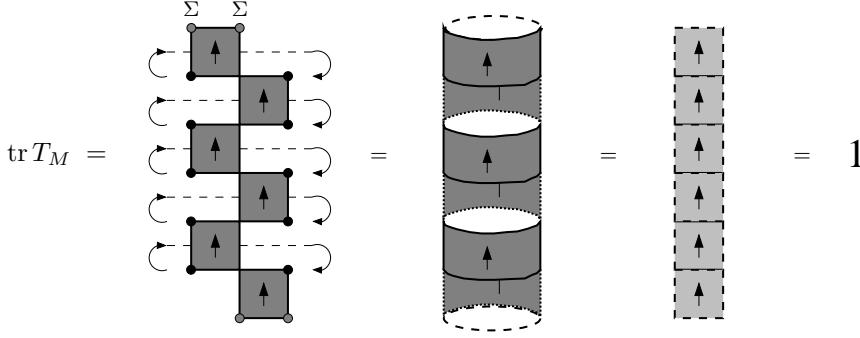
Figure 5.2.: Performing the trace of the transfer-matrix connects left and right indices. Thereby, T_M is rolled up on a cylinder and all local plaquettes trivialize. Thus, $\operatorname{tr} T_M = 1$.
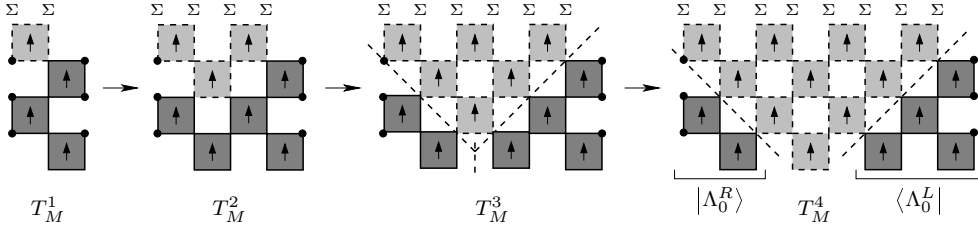

Figure 5.3.: By multiplying transfer-matrices a number of plaquettes decouple due to the trivialisation process. T_M^{2M-1} is shown to decompose into two separate parts, which are identified with the left and right leading eigenvectors $\left|\Lambda_0^R\right\rangle$ and $\left\langle\Lambda_0^L\right|$ of T_M.

completely into two separate parts for T_M^3, which are not connected by any non-trivial plaquette. The lattice formed by any higher powers of T_M corresponds to the case T_M^3, because only the number of trivial plaquettes is increased.

We now explicitly construct two vectors to prove (5.13) (here shown for the case $M = 2$)

$$(5.14)$$

The index l_{2M-1} is used as a dummy index, because it is not connected by any plaquette. Using the definition (5.14) and figure 5.3 we have shown that large powers of T_M indeed reduce to an outer product $\left|\Lambda_0^R\right\rangle\left\langle\Lambda_0^L\right|$.

Furthermore, one can easily show that $\left|\Lambda_0^R\right\rangle$ and $\left\langle\Lambda_0^L\right|$ are right and left eigenvectors of T_M with eigenvalue $\Lambda_0 = 1$, cf. figure 5.4.
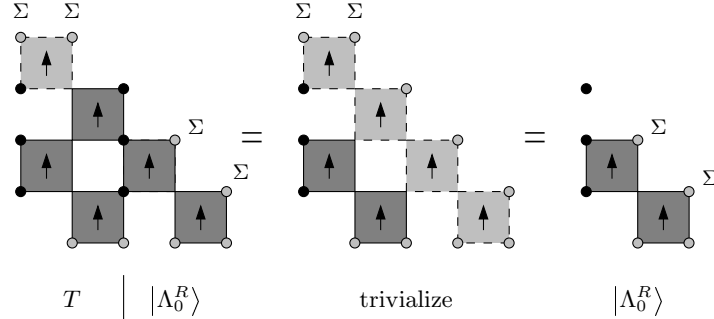
Figure 5.4.: Pictorial proof, that $\left|\Lambda_0^R\right\rangle$ is indeed the right eigenvector of T_M, belonging to the eigenvalue $\Lambda_0 = 1$. Analoguously one can show straightforward that $\left\langle\Lambda_0^L\right|$ is the corresponding left eigenvector.

As a consequence, equation (5.12) and (5.13) already determine the whole spectrum of T_M. The property $T_M^k = T_M^{2M-1}$ for all $k \geq 2M-1$ implies $\Lambda_i^{2M-1} = \Lambda_i^k$ for all eigenvalues Λ_i. Hence, Λ_i either vanishes or is unity. We have already shown, that $\Lambda_0 = 1$ is an eigenvalue of T_M. Due to (5.12) all other eigenvalues Λ_i ($i > 0$) must vanish, thus the complete spectrum reads

$$\mathrm{Spec}(T_M) = \{1, 0, 0, 0 \cdots, 0\} \ . \tag{5.15}$$

$\Lambda_0 = 1$ is therefore the leading eigenvalue and its eigenspace is not degenerate. The degenerate shape of the other eigenvalues of T_M can be understood physically in terms of two-point correlations in the stochastic model. Consider e.g. the density correlation function (cf. eq. (1.51) with $\Lambda_0 = 1$)

$$\langle n_0 n_r \rangle = \left\langle\Lambda_0^L\right| T_M(n) T_M^{r/2-1} T_M(n) \left|\Lambda_0^R\right\rangle \ . \tag{5.16}$$

Eq. (5.16) is visualized in fig. 5.5. The trivialization process verifies that the
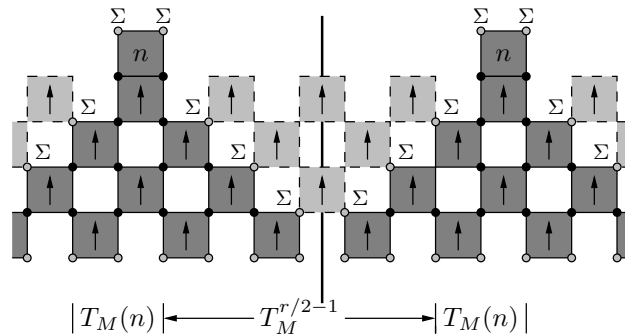
Figure 5.5.: The figure proves in a pictorial way that correlations $\langle n_0 n_r \rangle$ resolve into separate parts, which correspond to $\langle n_0 \rangle \langle n_r \rangle$.

the lattice site 0 at the time step $t = M\Delta t$ is completely uncorrelated with r

$$\langle n_0 n_r \rangle = \langle n_0 \rangle \langle n_r \rangle \, , \tag{5.17}$$

if they are sufficiently far away from each other $r \geq 2M - 1$. The correlation length therefore is zero. Referring to eq. (1.51) which connects the spectrum of the T_M with its eigenvalues

$$\xi_\alpha = -\frac{2}{\ln |\Lambda_\alpha|} \tag{5.18}$$

either implicates $\Lambda_\alpha = 0$ ($\alpha \neq 0$).

5.3. The Choice of the Density-Matrix

The properties of the stochastic transfer-matrix discussed in the previous section give rise to the choice of the density-matrix.
We first consider the asymmetric density-matrix as also used in the quantum TMRG case

$$\rho = \mathrm{tr}_{\mathrm{e}} \left| \Lambda_0^R \right\rangle \left\langle \Lambda_0^L \right| \, . \tag{5.19}$$

We exemplify by means of the special case $M = 2$, why ρ reduces to a projector. In fig. 5.6 left and right eigenvector $\left| \Lambda_0^L \right\rangle_{M=2}$ and $\left| \Lambda_0^R \right\rangle_{M=2}$ are pictorially rep-

$$\left| \Lambda_0^R \right\rangle_{M=2} \quad \left| \left\langle \Lambda_0^L \right|_{M=2} \qquad \qquad \text{trivialize} \qquad \left| \Lambda_0^R \right\rangle_{M=1} \quad \left| \left\langle \Lambda_0^L \right|_{M=1}$$
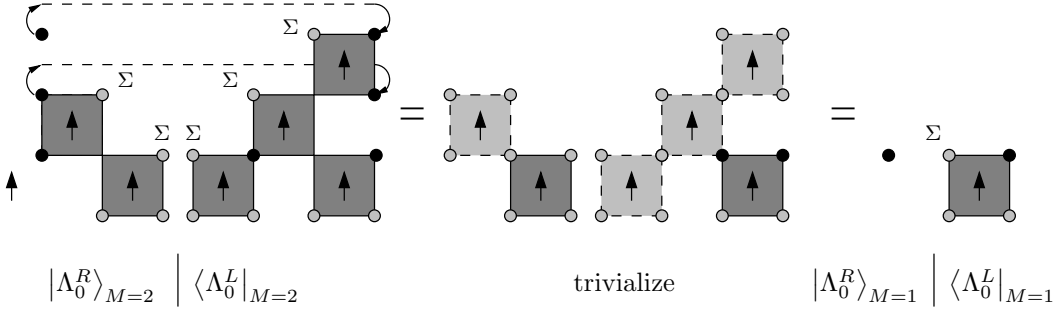
Figure 5.6.: The density-matrix for $M = 2$ is shown, which reduces due to the trivialisation process to a pure projector

resented, (see eq. (5.13)). The partial trace sums out the environmental indices. Due to the trivialization process of eq. (5.11), one finds that

$$\mathrm{tr}_{\mathrm{e}} \left(\left| \Lambda_0^R \right\rangle_M \left\langle \Lambda_0^L \right|_M \right) = \left| \Lambda_0^R \right\rangle_{M-1} \left\langle \Lambda_0^L \right|_{M-1} \, . \tag{5.20}$$

Interpreting the latter result physically, the states of the system block are completely uncorrelated with the environment block. A simple physical argument is that the environment block represents something like the "future" of the system block. Therefore, information of the environment does not influence the "past" of the system part.
However, such behavior spoils severely the concept of a density-matrix renormalisation. It is not predictable, which states of the system block are relevant for the enlargement procedure.

The alternative choice of the symmetrised density-matrix in eq. (5.10) has a different projecting effect. Here, a *simultanious* right and left renormalisation basis for $\left|\Lambda_0^{L/R}\right\rangle$ is constructed, since the functional

$$S(\left|\tilde{\Lambda}_0^R\right\rangle) + S(\left|\tilde{\Lambda}_0^L\right\rangle) = \left\| \left|\Lambda_0^R\right\rangle - \left|\tilde{\Lambda}_0^R\right\rangle \right\| + \left\| \left|\Lambda_0^L\right\rangle - \left|\tilde{\Lambda}_0^L\right\rangle \right\| . \tag{5.21}$$

is minimized, following the notation of sec. 1.1.2. Numerical results confirm that this choice of ρ works fine at least for some TMRG steps, which is demonstrated in the next section. Nevertheless the question remains, why the left and right projection basis has to be mixed.

An ad hoc explanation was given by ENSS and SCHOLLWÖCK [122], which aims at the structure of $\left|\Lambda_0^{L/R}\right\rangle$. We specify their arguments by considering the renormalization step from $M = 2$ to $M = 3$:

$$\left\langle\Lambda_0^L\right|_{M=2} \qquad \left|\Lambda_0^R\right\rangle_{M=2} \qquad \left|\Lambda_0^R\right\rangle_{M=3}$$
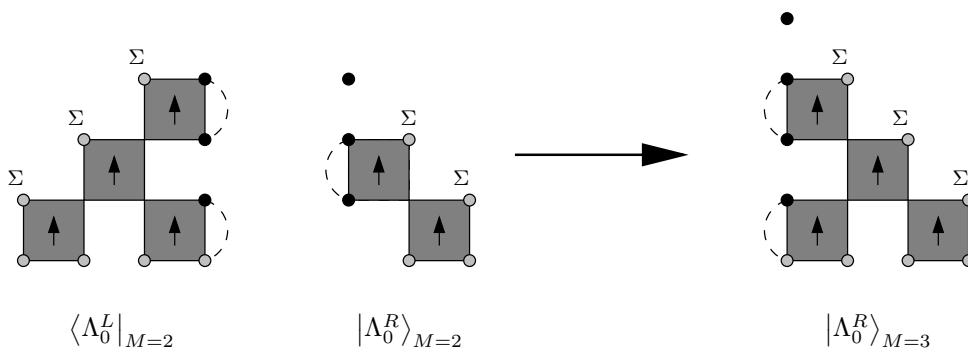
They argued that the enlarged vector $\left|\Lambda_0^R\right\rangle_{M=3}$ is not adequately represented by a renormalisation basis coming from $\left|\Lambda_0^R\right\rangle_{M=2}$. In $\left|\Lambda_0^R\right\rangle_{M=2}$ the even bonds are connected (correlated) by a plaquettes which changes in $\left|\Lambda_0^R\right\rangle_{M=3}$ to odd bonds. ENSS and SCHOLLWÖCK concluded that it is necessary to mix a renormalisation basis coming from $\left\langle\Lambda_0^R\right|_{M=2}$, which better suites to the structure of $\left|\Lambda_0^R\right\rangle_{M=3}$. Vice versa, a renormalisation basis for $\left\langle\Lambda_0^L\right|_{M=3}$ should involve $\left\langle\Lambda_0^L\right|_{M=2}$.

This at least explains, why the choice of a symmetric density-matrix is better than the asymmetric one. Nevertheless, we think that the arguments of more or less correlated bonds do not really prove that (5.10) induces an *optimal* renormalisation basis.

5.4. Applications

In this section we present TMRG results and interpretations, taken from [123, 122]. Fig. 5.7 presents TMRG data for the diffusion-annihilation process (see sec. 4.4.1), which is compared to exact data, calculated by eq. (4.28). The exact result is well reproduced up to $M \sim 100$ Trotter steps. The relative error is shown in the inset of fig. 5.7. It is interesting that data obtained by the asymmetric density-matrix is physically completely different. ENSS and SCHOLLWÖCK found out that here the density decays like $n(t) \sim t^{-1}$, which is exactly the mean field result.

In the simplest mean field approximation is the rate of reaction is proportional to the product of the concentration of reacting particles [105]. This approach
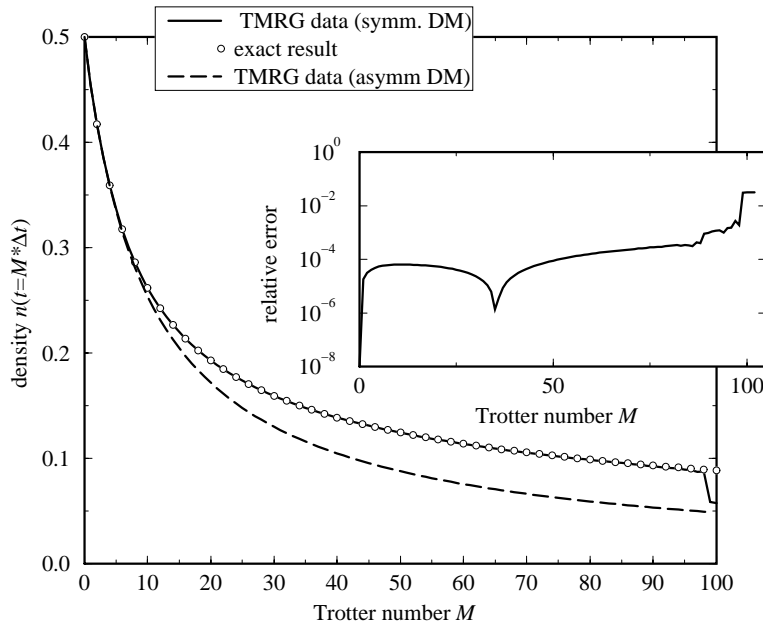
Figure 5.7.: TMRG results for the DAP for $D = \alpha = 0.5$ and $\Delta t = 1$, taken from [122]. The data is compared to exact results ($\circ$), which is shown in the inset. Additionally, TMRG data using the asymmetric DM is plotted by the dashed line.

assumes the homogeneity of the propability distribution, which is induces by a strong diffusion. In the case of the DAP the mean field equation reads

$$\partial_t n = -2\alpha n^2(t) \ , \tag{5.22}$$

yielding a solution

$$n(t) = \frac{n(0)}{1 + 2\alpha n(0)t} \sim t^{-1} \ . \tag{5.23}$$

This gives rise to the fact that the asymmetric density-matrix destroys important correlations and simply produces a mean field result.

Nevertheless, it is a crucial question, why the stochastic TMRG breaks down after $M \approx 100$ Trotter steps. Computations of various models, such as computations of the Domany-Kinzel cellular automaton in [121] or the branch-fusion process in [122], show the same behaviour. ENSS and SCHOLLWÖCK experimented with several numerical tricks to increase the precision. It seems that a great problem of the stochastic TMRG is found in the bad conditioned numerics. Just in order to give an impression of what happens, a typical situation of the minimal and maximal matrix element of the stochastic transfer-matrix T_M are plotted in fig. 5.8. The bandwidth of these extremal numbers increases exponentially by each Trotter step. This is a typical situation, where the floating point arithmetic of a computer numerically collapses.
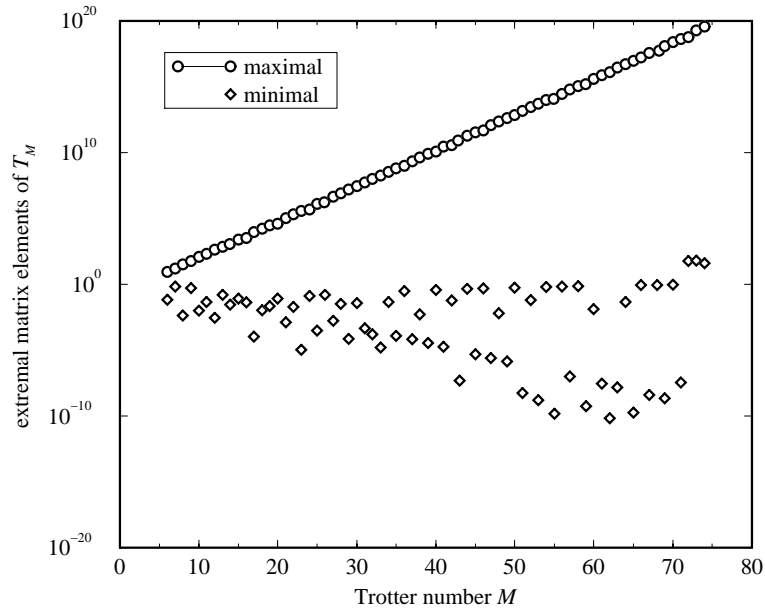
Figure 5.8.: Typical numerical evolution of the (absolute) extremal matrix ele-
ments of the stochastic transfer-matrix T_M. The maximal and min-
imal values exhibit an exponentially growing gap, showing that the
transfer-matrix is very bad conditioned.

Therefore, research was stopped in that field, because it was not possible to
overcome the inherent numerical problems in the stochastic TMRG. The ques-
tion arises, whether the numerical instabilities are a pure technical problem or
trace back to physical reasons of a wrong choice of T_M or the density-matrix.
We solved the problem by proposing a completely new variant of the algorithm
that is presented in the next section.

6. The Light-Cone CTMRG Algorithm

6.1. Introduction

As shown in the last section, the stochastic TMRG algorithm suffers from inherent numerical problems with physical origin. Therefore, possibilities of alternative approaches were evaluated, motivated by the physical properties of the stochastic transfer-matrix discussed in sec. 5.2.

One of the most important results of the theoretic studies of stochastic transfer-matrices is the computation of local averages, e.g. the local density $n(t)$. The decoupling process can be used to introduce a new method of calculating $n(t)$.
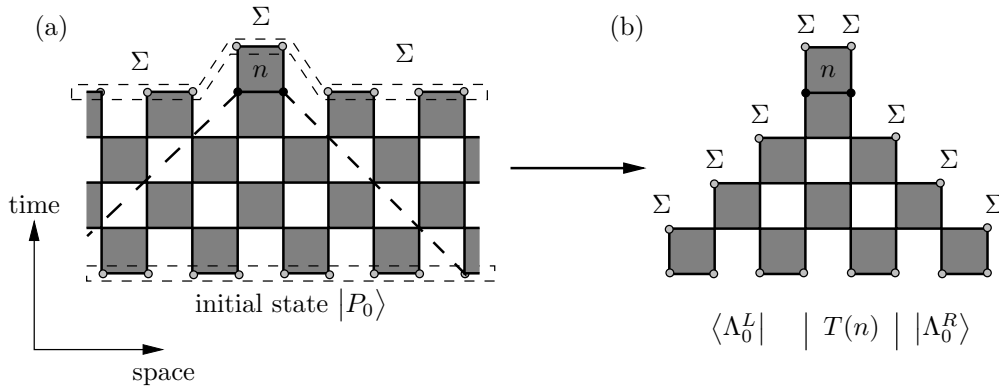
Figure 6.1.: (a) Trotter-Suzuki decomposition of $n(t) = \langle 0|n \cdot \mathrm{e}^{-tH}|P_0\rangle$ for $M = 2$. The 2D lattice is infinitely extended in space and finite in time direction. (b) Reduction of the 2D lattice to a triangle structure due to the trivialization mechanism (5.11). Note, that the lattice structure corresponds to the calculation of $n(t) = \langle \Lambda_0^L|T(n)|\Lambda_0^R\rangle$.

Figure 6.1 depicts the 2D classical lattice which evolves from the Trotter-Suzuki decomposition (here shown for $M = 2$). Using the trivialization mechanism of (5.11) the infinite lattice can be reduced to a *finite* triangle one. The pictorial representation in (5.8) and (5.14) verifies that the weight of the triangle lattice corresponds to the matrix element $\langle \Lambda_0^L|T(n)|\Lambda_0^R\rangle$ (see also (5.1)). Physically, the decoupling process can be explained by a causality argument: only the "past" light-cone of plaquette interactions can influence the site where the local average is measured.

The observation that a finite dimensional lattice is sufficient for the purpose of computing local averages raises the question, if the TMRG algorithm of chapter 5 is an appropriate numerical approach to stochastic systems.

The main advantage of the TMRG is that the thermodynamic limit of the space dimension is performed exactly, cf. sec. 1.2.1. But as most parts of the lattice in fig. 6.1 trivialize, only a *finite* triangle lattice remains. For such finite lattices much more powerful and stable numerical methods are known, such as the corner-transfer-matrix DMRG (CTMRG) algorithm, which was introduced by NISHINO and OKUNISHI in 1996 [22, 23].

Therefore, we have developed a completely new approach using a CTMRG based algorithm [124], which particularly fits onto the specific temporal characteristics of stochastic models. We refer to the newly proposed algorithm as *stochastic light-cone CMTRG* (LCTMRG). As suggested by its name, the LCTMRG combines ideas of the the stochastic TMRG and CTMRG algorithms, adjusted by the causality argument of the "light-cone decoupling" described above. Applications to two stochastic models (cf. section 6.6) display impressively that the LCTMRG is a considerable improvement of the stochastic TMRG with respect to numerical stability and performance.

We briefly recapitulate the basic concepts of the "classical" CTMRG algorithm in sec. 6.2, following [22, 23], before we present the LCTMRG method in sec. 6.3.

6.2. The Traditional CTMRG Algorithm

Similar to the TMRG algorithm, the CTMRG method is used to calculate physical properties of two-dimensional classical systems. As an example we consider a square lattice (see fig. 6.2) with classical spins on each site, e.g. the 2D ISING model.
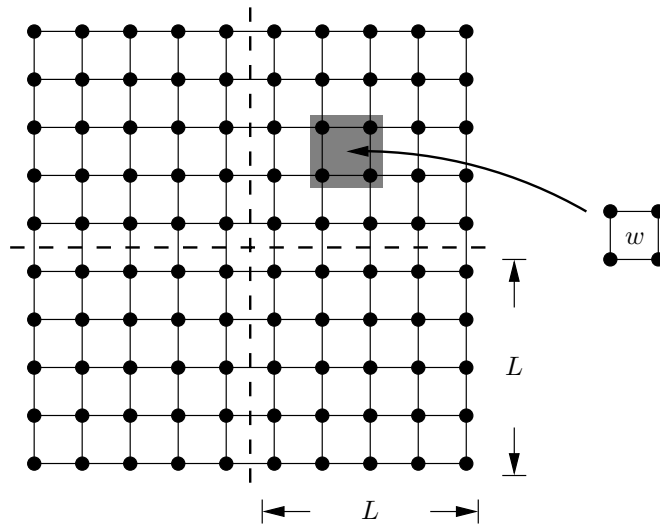
Figure 6.2.: Classical Ising lattice with dimension $2L \times 2L$. The bonds represent local interactions between neighboring sites. Classical spins are situated on the sites. The shades sites are summed out to establish open boundary conditions.

In the TMRG algorithm, transfer-matrices T_M were used, such that the solution

of the (classical) partition function

$$Z = \sum_{\{s\}} \prod_{\langle i,j,k,l \rangle} w_{s_k s_l}^{s_i s_j} \tag{6.1}$$

transforms into an eigenvalue problem of T_M. In eq. (6.1) $w_{s_k s_l}^{s_i s_j}$ label BOLTZ-MANN weights, which effect only neigboring sites $\langle i,j,k,l \rangle$.

The philosophy of the CTMRG algorithm is quite different. The lattice is first decomposed (see fig. 6.2) into four so-called corner-transfer-matrices (CTMs)

$$(C_N)_n^{n'} = \tag{6.2}$$

The indices of the cuts are summarized to block indices $n = s_1 \otimes \cdots \otimes s_L$ and $n' = s_1' \otimes \cdots \otimes s_L'$. Note, that by definition s_L and s_L' are the same, thus $(C_L)_n^{n'} = 0$ for $s_L \neq s_L'$. We have defined only one CTM, because the Ising model is isotrop and all CTMs coincide. Note, that the definition of CTMs was already done by BAXTER [125] in the framework of analytical calculations.

In a DMRG-like manner the CTMs represent the "system block" of the model, which has to be *enlarged* and numerically *renormalized*. This is done by adding column and row transfer-matrices

$$(T_L)_n^{n'} = \tag{6.3}$$

to each cut of the CTM, which explicitly reads

$$(C_{L+1})_{\tilde{n}}^{\tilde{n}'} = \sum_{n'''n''} \delta_{s_{L+1}' s_{L+1}} w_{s_L s_{L+1}}^{s_L'' s_L'} (T_L)_{n'''}^{n'} (C_L)_{n''}^{n'''} (T_L)_n^{n''} . \tag{6.4}$$

Similar to n the indices n', n'', n''' label the block spin of L classical spins, $\tilde{n}$ and $\tilde{n}'$ those of $L+1$ spins. Analogously, the transfer-matrices are enlarged $T_L \rightarrow T_{L+1}$. The enlargement procedure is visualized in fig. 6.3.

The density-matrix to reduce the enlarged $L+1$ spin CTMs is given by the forth power of the CTMs

$$\rho^{\tilde{n}''''\tilde{n}} = \sum_{\tilde{n}'''\tilde{n}''\tilde{n}'} (C_{L+1})_{\tilde{n}'''}^{\tilde{n}''''} (C_{L+1})_{\tilde{n}''}^{\tilde{n}'''} (C_{L+1})_{\tilde{n}'}^{\tilde{n}''} (C_{L+1})_{\tilde{n}}^{\tilde{n}'} , \tag{6.5}$$

which is depicted in fig. 6.4. The indices $\tilde{n}, \tilde{n}', \tilde{n}'', \tilde{n}'''$ and $\tilde{n}''''$ label again block spins of $L+1$ spins. Pictorially speaking, the square lattice has partially been
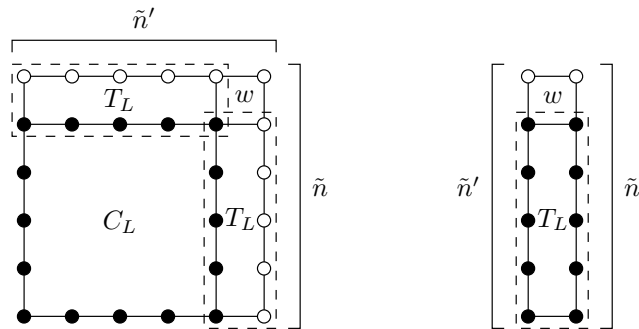
Figure 6.3.: Enlargement of the CTM $C_L \to C_{L+1}$ and TM $T_L \to T_{L+1}$. The indices $\tilde{n}, \tilde{n}'$ are block spins of $L + 1$ sites.

cut to construct the density-matrix.

It is important to notice that the density-matrix defined here corresponds to that of the TMRG algorithm. Two CTMs approximate the leading eigenvector $\left| \Lambda_0 \right\rangle$

$$(\Lambda_0)_{\tilde{n}\tilde{n}''} = \sum_{\tilde{n}'} (C_{L+1})_{\tilde{n}'}^{\tilde{n}} (C_{L+1})_{\tilde{n}''}^{\tilde{n}'} . \tag{6.6}$$

(Note, that left and right eigenvectors have not to be distinguished here due to the symmetry). Consequently, the DM can also be written as

$$\rho_{\tilde{n}}^{\tilde{n}'} = \sum_{\tilde{n}''} (\Lambda_0)_{\tilde{n}'\tilde{n}''} (\Lambda_0)_{\tilde{n}\tilde{n}''} . \tag{6.7}$$

The leading eigenvector $\left| \Lambda_0 \right\rangle$ is approximated by the CTMs, because they can be viewed as a number of stacked transfer-matrices. According to eq. (1.71) sufficiently large powers of T_L project onto the leading eigenvector.

Like in the traditional DMRG algorithm, the DM can now be used to reduce the vector space of the CTMs $C_{L+1} \to \tilde{C}_{L+1}$ and TMs $T_{L+1} \to \tilde{T}_{L+1}$. The procedure continues iteratively to increase the effective size of the CTMs and TMs, whereas the absolute dimension is fixed by the number of retained DMRG states.

The CTMRG has successfully been applied to various classical models [126, 127]. We finally mention that in principle expansions of the method to higher dimensional models are possible [128].

6.3. The Concept of the LCTMRG

We now construct the LCTMRG algorithm, which is a variant of the CTMRG algorithm presented in the last section, applied to the triangle structure of the 2D lattice (see also fig. 6.1). Exemplarily, we consider the case $M = 3$ to illustrate the concept of the new algorithm. As shown in figure 6.5, four cuts are set to separate the triangle lattice into four parts, similar as in the CTMRG algorithm. These cuts are somewhat native to our model, because they form
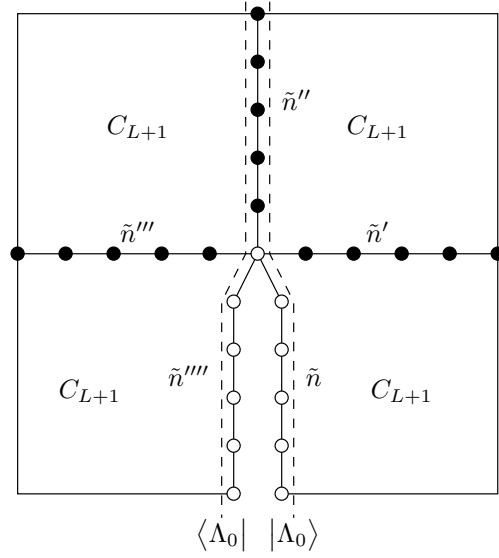
Figure 6.4.: Construction of the (reduced) density-matrix ρ by the forth power of the corner transfer-matrix C_{L+1}.
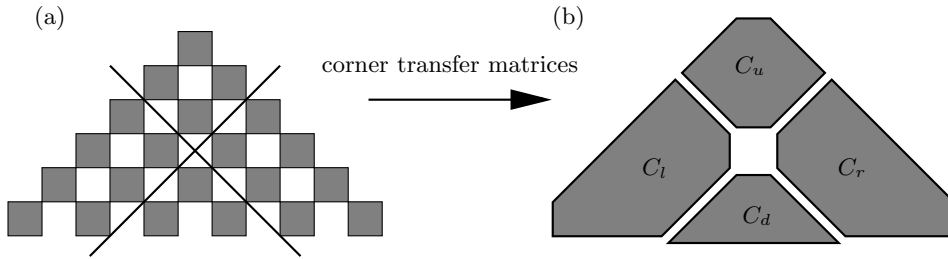

Figure 6.5.: Construction of corner-transfer-matrices. (a) The lattice is split into four parts. (b) Schematic plot of the corner-transfer-matrices C_u, C_d, C_l, and C_r evolving from (a).

the boundaries of the "future" and "past light cone" of the center point of the triangle.

The four parts

$$(C_l)_{n_s}^{\bar{n}_s} = \qquad , \qquad (C_r)_{n_s}^{\bar{n}_s} = \qquad (6.8)$$

$$(C_d)_{n_s}^{\bar{n}_s} = \bar{n}_s \qquad n_s \qquad , \qquad (C_u)_{n_s}^{\bar{n}_s} = \qquad (6.9)$$

are consequently interpreted as corner transfer-matrices (CTM), where the indices n_s and $\bar{n}_s$ label the block-spins of each cut.

We next show how these CTMs can be treated within a CTMRG algorithm. However, a number of modifications are necessary to adapt the "traditional" CTMRG to the light cone of plaquettes. Note, that as an important difference to sec. 6.2, the classical lattice of the stochastic case is in general not homogeneous. In the last section it was shown that in a CTMRG algorithm the CTMs are enlarged sequentially by adding transfer-matrices (TMs) to each cut. We first define these TMs in a pictorial way

$$(T_{ld})_{n_s s}^{\bar{n}_s \bar{s}} = \qquad , \qquad (T_{rd})_{n_s s}^{\bar{n}_s \bar{s}} = \qquad \qquad (6.10)$$

$$(T_{lu})_{n_s s}^{\bar{n}_s} = \qquad , \qquad (T_{ru})_{n_s s}^{\bar{n}_s} = \qquad . \qquad (6.11)$$

The bullets represent single-spin sites $s, \bar{s}$ and the spins $n_s, \bar{n}_s$ marked with bars will become renormalized block spins in the DMRG algorithm. Exemplarily, (6.10) and (6.11) show TMs which are used to enlarge the triangle lattice of figure 6.5 (a).

Figure 6.6 demonstrates graphically how the TMs are used to enlarge the CTMs, whereby CTMs and TMs are "jointed" by summing out the adjacent indices (similar to eq. (6.4)). Due to the exotic geometry of the lattice we have to distinguish between an "upper" and "lower" extension step, depending on whether C_u or C_d should be enlarged. In our LCTMRG algorithm both extension steps
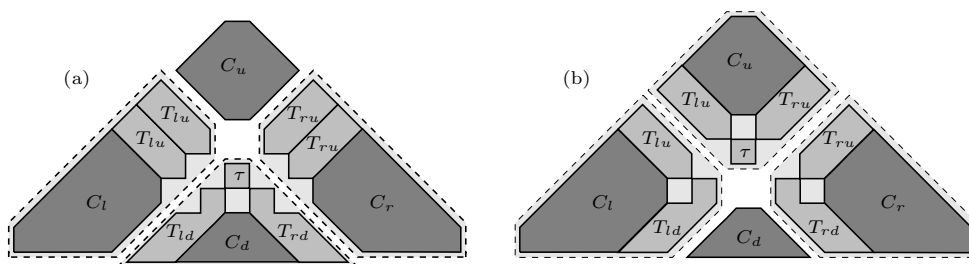

Figure 6.6.: Extension of the CTMs by adding diagonal TMs. In (a) the lower part of the triangle is enlarged whereas in (b) the extension is performed to the upper part. In the LCTMRG algorithm the upper and lower extensions are done alternately, so that all CTMs grow step by step.

are implemented alternately. That way all CTMs grow step by step with the crossing point of the cuts always situated in the effective center of the triangle. After each extension step the CTMs have to be renormalized by a density-matrix projection, cf. section 6.4.

The local density $n(t)$ can be obtained using C_d, T_{ld} and T_{rd}:

$$n(t) = \qquad (6.12)$$

It is important that $n(t)$ has to be computed *in the center* of the triangle lattice. Here, influences of boundary effects are expected to be smallest. In terms of a DMRG algorithm, the CTMs C_l, C_r and C_u act as an "environment" of the "system" C_d. As a technical remark, the summation of the boundaries in (6.12) is realized by storing the vector $|1\rangle$ of all possible configurations explicitly and multiplying it in (6.12) to the left and right hand side. Note, that $|1\rangle$ has to be renormalized as well.

6.4. The Choice of the Density-Matrix

The key problem is to find a reasonable density-matrix projection for the renormalization of the CTMs after each extension step. We exemplify the construction of the density-matrix by looking at figure 6.6 (a). Here, one block-spin and two spins of C_d, C_l and C_r have to be renormalized into one block-spin. The construction of the optimal density-matrix projection is now discussed in detail.

First, we define four vectors:

$$(\psi_R^R)^{\bar{n}_s}_{n_s,s_1,s_2} = \qquad\qquad (\psi_L^R)^{\bar{n}_s}_{n_s,s_1,s_2} = \qquad (6.13)$$

$$(\psi_R^L)^{\bar{n}_s}_{n_s,s_1,s_2} = \qquad\qquad (\psi_L^L)^{\bar{n}_s}_{n_s,s_1,s_2} = \qquad (6.14)$$

The block spin $\bar{n}_s$ belongs to the environment, s_1, s_2 and n_s to the system block. Note that these vectors approximate the left and right eigenvector of the leading eigenvalue of diagonal TMs

$$T_R = \qquad \text{and} \qquad T_L = \qquad (6.15)$$

which have a different shape compared to the stochastic TMs used in the stochastic TMRG, cf. sec. 5. As ψ_R^x and ψ_L^x $(x = L, R)$ have not to be computed by any expensive diagonalization routine like in TMRG, the LCTMRG algorithm is much faster.

ψ_R^x and ψ_L^x are used to construct a reduced density-matrix for each of the two cuts. The generic choice would be a symmetric density-matrix

$$\rho_x^{[1]} = \text{tr}_{\bar{n}_s} \left(\left| \psi_L^x \right\rangle \left\langle \psi_L^x \right| + \left| \psi_R^x \right\rangle \left\langle \psi_R^x \right| \right) \tag{6.16}$$

which was also used in section 5. Here $\text{tr}_{\bar{n}_s}$ denotes the partial trace over $\bar{n}_s$. $\rho_x^{[1]}$ produces a reduced system block basis which optimally approximates ψ_L^x and ψ_R^x [107]. However, one can easily proof that ψ_R^x is trivially given by

$$(\psi_R^x)_{n_s, s_1, s_2}^{\bar{n}_s} = 1 \quad \text{for all } n_s, s_1, s_2, \bar{n}_s , \tag{6.17}$$

which follows directly from the trivialization process (5.11). Obviously ψ_R^x is not very useful for constructing a density-matrix, because

$$\text{tr}_{\bar{n}_s} \left| \psi_R \right\rangle \left\langle \psi_R \right| = \left| 1_s \right\rangle \left\langle 1_s \right| \quad \text{with} \quad (1_s)_{n_s, s_1, s_2} = 1 \tag{6.18}$$

reduces to a trivial projector which does not correlate system and environment block, see also sec. 5.3. Hence, we omitted ψ_R^x and tested the density-matrix

$$\rho_x^{[2]} = \text{tr}_{\bar{n}_s} \left| \psi_L^x \right\rangle \left\langle \psi_L^x \right| \tag{6.19}$$

which led to much better results (cf. section 6.6). An asymmetric choice

$$\rho_x^{[3]} = \text{tr}_{\bar{n}_s} \left| \psi_R^x \right\rangle \left\langle \psi_L^x \right| \tag{6.20}$$

of the density-matrix performs worst. As

$$\left\langle n_s', s_1', s_2' \right| \rho_x^{[3]} \left| n_s, s_1, s_2 \right\rangle = \sum_{\bar{n}_s} (\psi_L^x)_{n_s, s_1, s_2}^{\bar{n}_s} \tag{6.21}$$

is independent of n_s', s_1', s_2', the density-matrix $\rho_x^{[3]}$ has rank one and represents a pure projector.

A physical explanation for the choice of $\rho_x^{[2]}$ can be given in terms of the light-cone picture of section 5.2. The trivial vector $\left| \psi_R^x \right\rangle$ is a superposition of all feasible states which means that at each cut no further information about the "future" is available. Not surprisingly, the system and environmental part of the cut are uncorrelated, which is expressed by a trivial density-matrix projection of $\text{tr}_{\bar{n}_s} \left| \psi_R^x \right\rangle \left\langle \psi_R^x \right|$. Only the physics of the past, the information of which is carried by $\left| \psi_L^x \right\rangle$, correlate system and environment indices.

6.5. Some Technical Aspects

We briefly discuss some implementation details of the LCTMRG algorithm. The first TMRG step should start with the following configuration
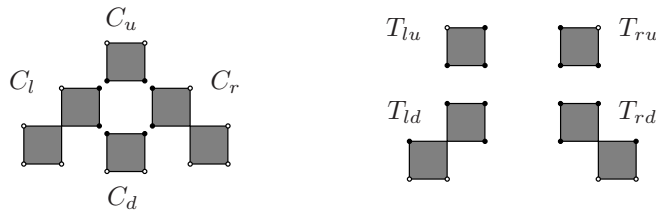
of transfer-matrices. This corresponds to the time $t = 1.5 \cdot \Delta t$ and is the simplest construction of initial CTMs and TMs. The first extension steps (cf. figure 6.6) are performed without renormalization until the dimension of the CTMs exceeds the number m of DMRG states.

As the transfer-matrix C_u is only used for the construction of ψ_R^x, which is not needed for computing $\rho_x^{[2]}$, C_u can be omitted completely. If additionally the local Hamiltonian $h_{i,i+1}$ is parity invariant, i.e. $h_{i,i+1} = h_{i+1,i}$, the local transfer-matrix τ becomes symmetric. Hence, only the CTMs C_l, C_d and TMs T_{ld}, T_{lu} have to be stored. C_r, T_{rd} and T_{ru} can be reconstructed by mirroring C_l, T_{ld} and T_{lu}.

In order to avoid floating point overflows of the algorithm, it is recommended to rescale all CTMs and TMs

$$C_x \to \frac{C_x}{\|C_x\|}, \quad T_x \to \frac{T_x}{\|T_x\|} \tag{6.22}$$

where $\|\cdot\|$ is some norm. Note, that these rescaling factors have to be considered in the computation of $n(t)$.

All computations, which are shown in the next section, were done on Sun Workstations (Ultra Sparc III, 900 MHz). Compared to the old stochastic TMRG the LCTMRG algorithm is tremendously more efficient. Furthermore, as most parts of the program consist of matrix multiplications of CTMs and TMs, the LCTMRG algorithm can easily be parallelized. The CPU time needed for one Trotter step ranges from a few milliseconds for $m = 32$ states up to a couple of seconds for $m = 400$ states. The consumption of computer memory is modest as well, e.g. 10 MB for $m = 32$ up to 200 MB for $m = 400$.

6.6. Applications

We applied the LCTMRG algorithm to the diffusion-annihilation (DAP) and branch-fusion (BFP) process, which were introduced in sec. 4.4.1 and sec. 4.4.2. The motivation of these choices is:

- The DAP is an exactly solvable, but non-trivial (i.e. not solvable by a mean-field approach) reaction-diffusion model.

- The BFP is a simple model, which exhibits a phase transition from an active into an absorbing phase. The critical point belongs to the DP universality class, where highly precise estimates of the critical exponents are available (see tab. 4.1).

Therefore, we have reliable reference data to judge about the precision of the LCTMRG results.

6.6.1. LCTMRG Results for the Diffusion-Annihilation Process

Figure 6.7 compares LCTMRG calculations with exact data for $D = 0.05$, keeping various numbers of DMRG states m. Up to more than $M \sim 10^5$ Trotter steps we obtain highly precise data with a deviation of less than 10^{-5} from the exact results. The inset of fig. 6.7 plots the LCTMRG data in a double-logarithmic plot, which shows that $n(t)$ falls of algebraically.

The high number of Trotter steps M is a considerable improvement to the old stochastic TMRG algorithm [121, 122] by at least *three* orders (see also fig. 5.7). Even though the DAP is critical, we observe an extremely stable convergence of the LCTMRG algorithm.

Figure 6.8 plots numerical data for different density-matrices $\rho^{[1]}$ and $\rho^{[2]}$, cf. sec. 6.4. In all our calculations we observe highly instable numerics, if the "conventional" density-matrix $\rho^{[1]}$ is used. In the example of fig. 6.8 the convergence of the algorithm breaks down after $M \sim 10^2$ Trotter steps, while $M \sim 10^5$ is possible for $\rho^{[2]}$. Thus the arguments given in sec. 6.4 can be confirmed numerically: $\rho^{[1]}$ is not an adequate density-matrix for the stochastic LCTMRG.

6.6.2. LCTMRG Results of the Branch-Fusion Process

In this section we focus on the critical phase transition of the BFP at $p_c = 0.84036(1)$ [107]. Figure 6.9 compares numerical data computed by the LCTMRG algorithm with conventional Monte-Carlo simulations.

For p sufficiently far away from criticality, we observe a convergence up to more than 10^4 Trotter steps. In the vicinity of the critical point $p \sim p_c$ the convergence becomes worse. Nevertheless, we want to determine the critical exponent α (see tab. 4.1), which should correspond to the value of the DP universality class.

Figure 6.10 plots the logarithmic derivative

$$\mathcal{L}(t) = \frac{\log n(t + \Delta t) - \log n(t)}{\log \Delta t} \tag{6.23}$$

at the critical point $p \sim p_c$ for $m = 400$ states. If the decay of $n(t)$ is algebraically, $L(t \to \infty)$ converges and determines the critical exponent α. It is even well known, that logarithmic derivatives are very sensitive to numerical errors, such that $L(t)$ is a good indicator for stable or instable numerics.

Up to more than 10^3 Trotter steps the numerics in fig. 6.10 are extremely precise and one can verify that $n(t)$ switches to an algebraic behavior. It is also possible to determine the critical exponent α by extrapolating $\mathcal{L}(t \to \infty)$, cf. inset of fig. 6.10. Thereby, we were able to compute α up to a precision of less than 0.1%:

$$\alpha \approx 0.1600(5) \qquad \text{(literature } \alpha_{\text{lit}} = 0.159464(5), \text{ cf. tab. } 4.1.) \tag{6.24}$$

The question arises why the convergence of the LCTMRG at $p \sim p_c$ is two orders less than in the DAP process, yet both models behave critical. We checked various numerical aspects to determine the origin of the worse convergence.
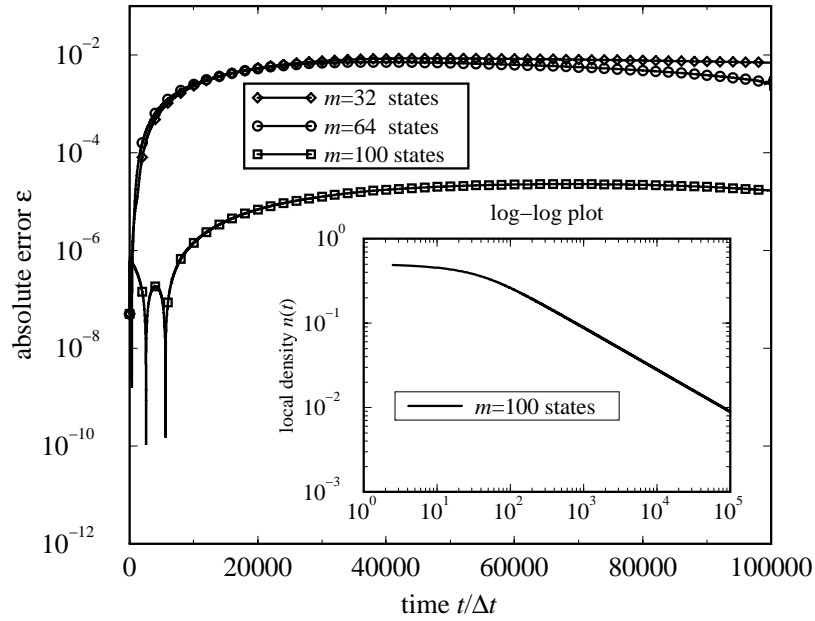
Figure 6.7.: The figure compares exact data for the DAP with LCTMRG computations by showing the absolute error $\epsilon = |n_{\mathrm{LCTMRG}}(t) - n_{\mathrm{exact}}(t)|$ for $D = 0.05$, keeping $m = 32, 64, 100$ states. The inset plots LCT-MRG data for $D = 0.05$ and $m = 100$ in a double-logarithmic plot and shows the algebraic decay.
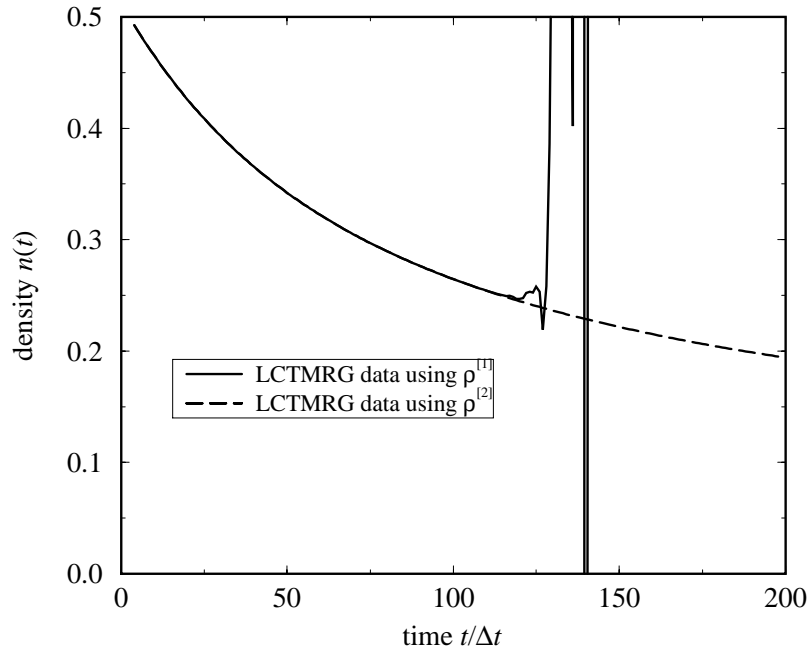

Figure 6.8.: The figure depicts LCTMRG data for $D = 0.5$, $m = 32$ by using different density matrices $\rho^{[1]}$ and $\rho^{[2]}$, showing that $\rho^{[1]}$ causes numerical instabilities.
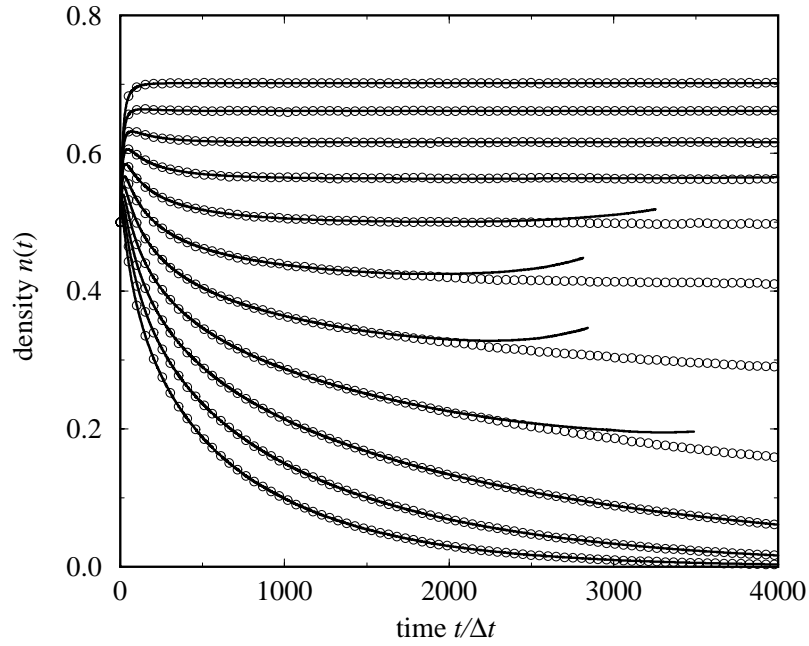
Figure 6.9.: The figure shows the dynamic evolution of the order parameter $n(t)$ of the BFP for $p = 0.9 \ldots 0.8$ (in steps of 0.01) keeping $m = 200$ states. For comparison Monte-Carlo simulations ($\circ$) are plotted.
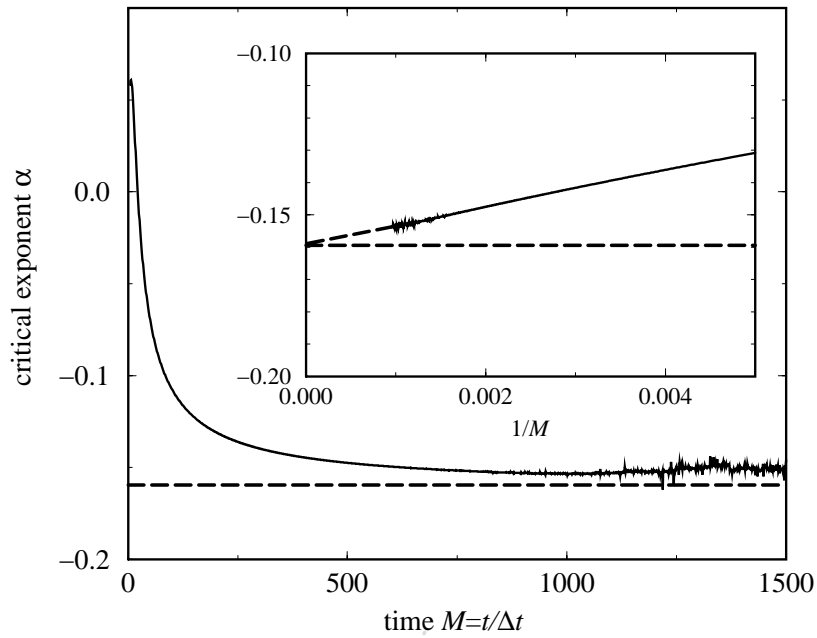

Figure 6.10.: The figure plots the logarithmic derivative $\mathcal{L}(t)$ which converges to the critical exponent α. The literature value is plotted by a dashed line. The inset shows $\mathcal{L}(1/t)$ which is used to interpolate the critical exponent α.

In the BFP it is conspicuous that the quality of the results at $p \sim p_c$ strongly depends of the number of states m that are retained within the LCTMRG algorithm. This is demonstrated in fig. 6.11 which plots numerical computations for various m at $p \sim p_c$.

However, it is surprising that so many states m are needed although there is a very strong fall off of the density-matrix eigenvalues ρ_i, cf. fig. 6.12.

As another possibility we check the influence of the size of the Trotter steps Δt on the numerics. The curves of fig. 6.13 belong to various Δt, but are rescaled to $\Delta t = 0.05$ for comparison. Even though finer Trotter decompositions increase the total number of convergent Trotter steps, one can not improve the accuracy of the data with respect to the absolute time t. If on the other hand Δt becomes too large, the Trotter decomposition itself gets worse and is then responsible for unsatisfactory numerical data.

To estimate the effect of numerical errors caused by floating point inaccuracies we implemented the diagonalization routine for the density-matrix alternatively by using higher mantissa bits. This was technically realized by using the GMP library [129] which allows an arbitrary number of mantissa bits. As shown in fig. 6.14, only a marginal effect on the numerics is observed.

Overall, it remains an open question what exactly is the limiting factor for the worse convergence at the phase transition point $p \sim p_c$ in the BFP. To exclude model specific reasons, we also checked other RDPs, e.g. the contact process. Qualitatively, the same limited convergence near the critical phase transition point is observed.

The numerical investigations show that the new LCTMRG algorithm is a considerable step towards a general and very efficient method for 1D stochastic problems. Compared to the traditional approach using Monte-Carlo simulations, we finally emphasize two fundamental advantages of out method:

- The LCTMRG is not a simulation technique. There is no need of taking random numbers and sample averages. The LCTMRG is a numerical renormalization group based on the quantum formalism for stochastic models where averages are directly accessible.

- The algorithm describes the *exact* thermodynamic limit $L \to \infty$ of the stochastic model. Note, that here we even have to deal with a *finite* classical 2D system only, due to the simplification from the "light-cone decoupling". Thus, there are in principle no finite-size effects like in MCS or stochastic DMRG.
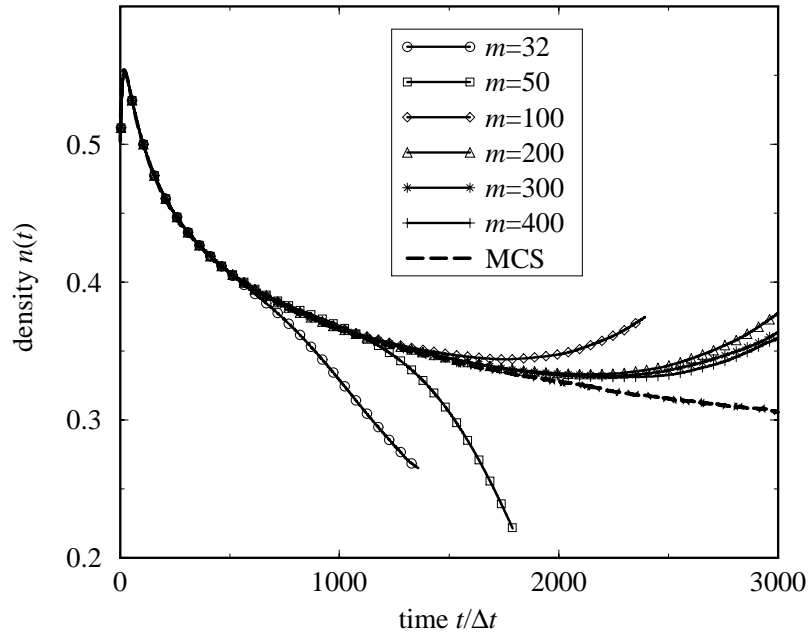
Figure 6.11.: The figure plots the dynamic evolution of the order parameter $n(t)$ of the BFP at criticality $p \sim p_c$ for various number of kept states $m = 32 \ldots 400$. A MCS is plotted for comparison by a dashed line.
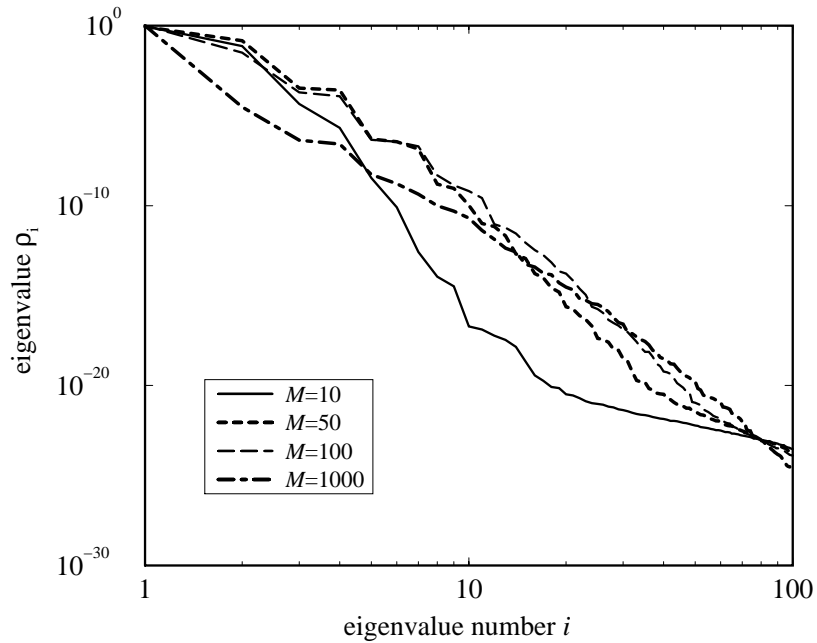

Figure 6.12.: In the figure one can see the spectrum ρ_i of the density-matrix ρ for Trotter steps $M = 10, 50, 100, 1000$ at criticality $p \sim p_c$.
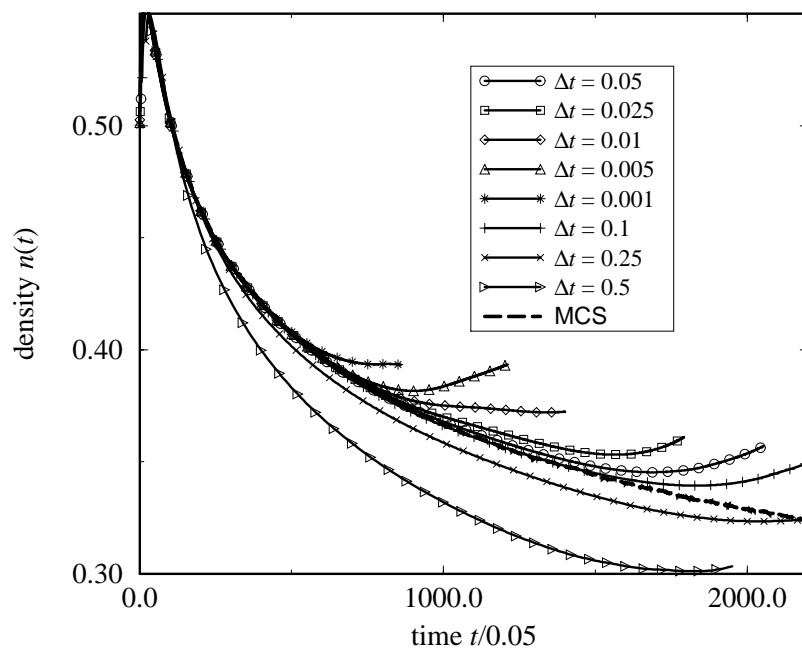
Figure 6.13.: Plot of the order parameter $n(t)$ of the BFP at criticality $p \sim p_c$, keeping $m = 64$ states, where $\Delta t = 0.001 \ldots 0.5$ is varied.
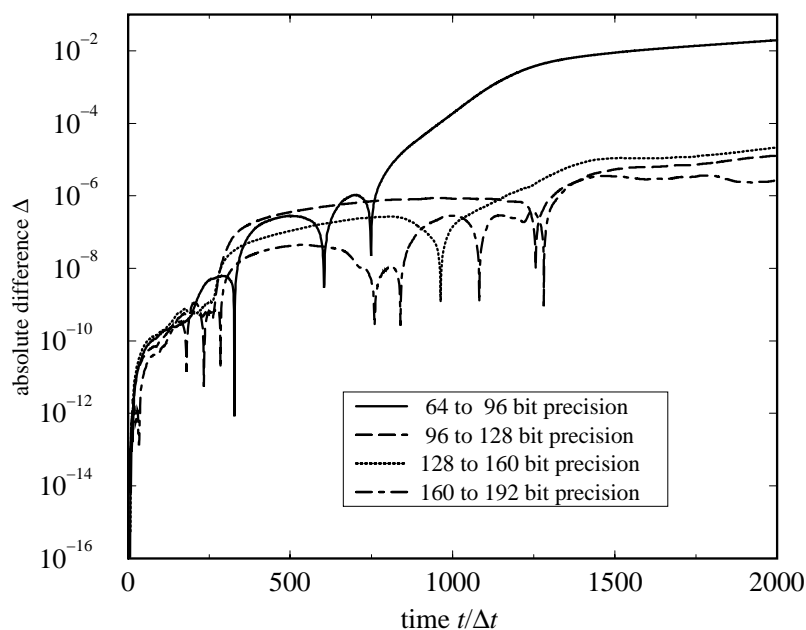

Figure 6.14.: The figure compares data calculated with various floating point precisions (i.e. 64, 96, 128 and 160 bits). The plot shows the differences of numerical data for each precision compared to the next higher one.

7. Conclusions

The present thesis dealt with two seemingly different types of physical models. In a first part thermodynamic properties of the Hirsch model are studied. In contrast, the second part of the thesis turns from equilibrium to non-equilibrium physics and investigated dynamic properties of stochastic systems. At first glance both models seem to be physically opposed, but a general *methodical* framework is found to study them, namely the transfer-matrix DMRG (TMRG) algorithm. Whereas the applicability of the traditional "quantum TMRG" onto the thermodynamics of fermionic systems necessitates only a few modifications, the "stochastic TMRG" is completely novel and its development an integral part of this thesis. In the following we summarize the essential results.

Thermodynamics of the Hirsch model

The Hirsch model extends the one-dimensional Hubbard model by an off-diagonal bond-charge interaction X, that leads to rich physics based on the breaking of particle-hole symmetry. We particularly focused on the parameter region $0 \leq X/t \leq 1$, which by symmetry arguments is representative for all parameters. Bosonization studies – valid for $X/t \ll 1$ – predict that the Hirsch model behaves like a Hubbard model with density n dependent effective Coulomb potential $U_{\mathrm{eff}} = 8X \cos(\pi n/2)$ and hopping amplitude $t_{\mathrm{eff}} = t - nX$. The particular case $X/t = 1$ is exactly solvable by free fermion techniques. Here, the whole energy spectrum is accessible and thermodynamic properties can be calculated rigorously. Between the bosonisation region $X/t \ll 1$ and the exact solvable point $X/t = 1$, some numeric groundstate studies are available as well, but only very little is known about the model's thermodynamics.

We numerically studied the Hirsch model using the quantum TMRG algorithm. The method allows for computations of thermodynamic potentials, local expectation values, the specific heat, susceptibilities and the asymptotic behavior of various two-point correlation functions. Since TMRG studies of fermion systems are quite rare in literature, we allude to some important technical details of the algorithm, e.g. the relevance of the fermion statistics and the role of spin and charge quantum numbers. We are able to realize up to 2000 TMRG iteration steps, which corresponds to a minimal reachable temperature of $T/t = 0.01$.

Our computations concentrate on *vanishing* Coulomb potential $U = 0$ and the particular cases $X/t = 0.1, 0.5, 0.9$ and $X/t = 1$. These choices represent small, intermediate and large values of X/t in the representative region $0 \leq X/t \leq 1$. The integrable case $X/t = 1$ is mainly used to check the precision of the numerics, verifying excellent agreement of exact and TMRG data down to temperatures $T/t \approx 0.02$.

In accordance with previous works, our studies of the spin and charge susceptibilities confirm two ($T = 0$) phases in the non-integrable regime $0 < X/t < 1$. Below half-filling we principally identify Tomonaga-Luttinger liquid behavior, where spin and charge excitations are gapless. For more than half-filling a Luther-Emery liquid phase with spin gap is found, if X/t is not too large.

The low-temperature behavior of the susceptibilities for $X/t = 0.1$ essentially correspond to the Hubbard model with effective Coulomb potential U_{eff} and hopping amplitude t_{eff}, as predicted by bosonization. For intermediate coupling $X/t = 0.5$ the correspondence holds qualitatively, but not quantitatively: Even though the phase transition occurs at approximately half filling, the low-temperature behavior of the susceptibilities contradict the bosonization results. For large $X \gtrsim 0.65$, the spin gap disappears for any fillings. Additionally, numerical investigations of the specific heat and density exhibit interesting phenomena of nearly universal crossing points. These can be understood from quite general thermodynamic considerations and have also been observed e.g. in the Hubbard model.

We completed the thermodynamic studies by focusing on thermal correlation functions, which is a fairly new TMRG research field. The asymptotic behavior of correlations can be characterized by thermal correlation lengths. These are connected with the eigenspectrum of the quantum transfer matrix. We discussed, how the respective eigenvalue can be assigned to the correct correlation function. Thereby, two-point density-density, spin-spin, singlet and triplet pair correlation lengths can be computed and even be distinguished into oscillating and non-oscillating parts.

The dominating correlation lengths in each phase characterize the principal physics of the Hirsch model. In the Tomonaga-Luttinger liquid phase the density correlations are observed to be dominant for all temperatures. In contrast, in the spin-gapped Luther-Emery liquid phase we find an interesting crossover of superconducting singlet-pair and density-density correlation lengths at *finite* temperature $T_c > 0$. Consequently, the low-temperature physics $T < T_c$ confirm a strong tendency to superconductivity. The crossover phenomena are indeed expected from previous $T = 0$ results and conformal field theory predictions. Note, that the one-dimensional Hirsch model is not strictly superconducting at finite temperatures, since off-diagonal long-range order is not possible. But our results give rise to speculate about true superconductivity of the Hirsch model in two dimensions. Unfortunately, up to now no reasonable TMRG algorithms have been developed for such two-dimensional quantum systems.

This thesis concentrates on the influence of the bond-charge term X only, thus we have chosen a vanishing on-site potential $U = 0$. However, in practice U may not be neglected for many experimental materials. This would be an interesting matter of future research, which could e.g. clarify the existence of a Mott transition for repulsive $U, X > 0$.

Overall we finally allude that the TMRG algorithm is indeed an *optimal* choice for our purposes. Alternatively, quantum Monte-Carlo simulations are often chosen to study thermodynamic properties. But in contrast, the TMRG has some fundamental advantages:

- The thermodynamics are treated in the *exact* thermodynamic limit of the quantum chain. This is guaranteed by the underlying transfer-matrix approach. Thus no finite size corrections affect the TMRG data.

- The TMRG does not suffer from "the sign problem" known from quantum Monte-Carlo simulations of fermionic models. We explicitly include the Fermi statistics into our approach by using a Jordan-Wigner transformation.

- The TMRG provides an elegant and effective way to compute the asymptotics of correlation functions in great detail. The correlation lengths can even be distinguished by oscillating and non-oscillating parts.

Dynamics of Stochastic Models

The second part of the thesis was dedicated to the development of a capable TMRG algorithm for stochastic models. This is possible due to certain well-known formal analogies to quantum models: The master equation, which describes the dynamic evolution of a stochastic model, can be mapped onto a Schrödinger equation in imaginary time. Thus various concepts known from equilibrium physics, such as criticality or universality, similar persist in the non-equilibrium case.

It was quite natural to transfer also the TMRG concept to the stochastic counterpart. In a similar way to the quantum case, the *dynamics* can be mapped onto a classical two-dimensional system by Trotter-Suzuki decomposition, where the time dimension takes the role of the (reciprocal) temperature. In almost one-to-one correspondence a "stochastic TMRG" algorithm is constructed up to a few, but important modifications. Astonishing mathematical properties of the stochastic transfer-matrices appear, that are deeply related to the underlying causal structure of the stochastic process. These are *not* known from the quantum TMRG, thus the identification of time and temperature is much more sophisticated than one would have originally expected.

Additionally, it is found that the numerical stability of the stochastic TMRG is poor. Only about 10^2 TMRG iterations are possible, which is small compared to usual quantum TMRG applications. The numerical problems seemed to be of a principal type, connected with ill-conditioned matrix elements of the transfer-matrix that are characteristical for the stochastic case.

Therefore, we introduced a completely new variant of a stochastic TMRG algorithm, which we call stochastic light-cone CTMRG (LCTMRG). As suggested by its name, this novel method allows for the causal structure of stochastic system mentioned above: Only a reduced, triangle shaped classical lattice has to be considered for calculating local averages. Such finite systems can numerically be studied by a corner-transfer-matrix DMRG (CTMRG) algorithm, which is well-known from studies of two-dimensional classical systems.

We have tested the new algorithm by comparing LCTMRG data to exact results and Monte-Carlo simulations of two different reaction-diffusion models, namely the diffusion-annihilation and branch-fusion process. As a spectacular result, we confirm highly precise numerical LCTMRG results up to 10^5 Trotter steps,

even if the model is *critical* as the diffusion-annihilation process. Compared to the "old" stochastic TMRG this means a considerable increase of at least *three* orders of magnitude. As an important observation, inherent numerical problems of the old stochastic TMRG algorithm obviously do not appear in our new approach. Thus the causal structure, that presumably induces the instabilities before, turns out to be an *advantage* after all.

However, in the vicinity of critical phase transition points, exemplified by the branch-fusion model, the convergence of the LCTMRG gets worse. Nevertheless we are able to determine sufficiently precise results for critical exponents. But it remains an open question what exactly causes the instabilities at critical phase boundaries. A crucial point of future studies should inherently focus on the density-matrix projection. We stress, that our choice is mainly based on numerical observations. But conspicuously the density-matrix weights in the LCTMRG algorithm decay extremely fast, which alludes to weak correlations between system and environment block. However, in each DMRG-style algorithm "sufficiently" strong correlations are important, since the renormalization step has to predict the physically relevant renormalization states for the enlargement of the system block. It is worth to speculate about the question, if White's density-matrix is indeed the best truncation procedure in the stochastic case, since the affected correlations are (too) weak.

But even if the number of possible time steps in particular *at phase transition points* can not compete with e.g. Monte-Carlo simulations up to now, we believe that stochastic TMRG algorithms can be an extremely valuable tool for future studies. Compared to the traditional simulations, there are two fundamental advantages of the LCTMRG:

- The LCTMRG is not a simulation technique. There is no need of taking random numbers and sample averages. The LCTMRG is a numerical renormalization group based on the quantum formalism for stochastic models, where all sample averages are intrinsically included. Therefore, the numerical results are extremely precise, do not suffer from any fluctuations, and consequently are well suited for interpolations of e.g. critical exponents.

- The algorithm describes the *exact* thermodynamic limit $L \to \infty$ of the stochastic model, even though only a finite triangle shaped classical system has to be computed. Thus, there are in principle no finite-size effects like in simulations.

We finally mention that a generalization of the LCTMRG to more than one dimension is imaginable, since higher dimensional CTMRG variants are known in the context of three-dimensional classical systems. It is also worth to study the (corner-)transfer-matrix spectrum that presumably is connected with correlation functions, similar to the quantum case. This use of spectral properties necessitates further intense contentions with theoretic properties of stochastic transfer-matrices. But the possibility of studying correlations in that way could be another valuable advantage over Monte-Carlo simulations.

A. Jordan-Wigner Transformation

The Jordan-Wigner transformation (JWT) is a very powerful mapping between spin and fermion systems. The basic idea is to identify the canonically local spin basis (e.g. $\left|S^z\right\rangle = \left|\uparrow\right\rangle, \left|\downarrow\right\rangle$) with the fermion basis (e.g. $\left|n\right\rangle = \left|0\right\rangle, \left|1\right\rangle$). Consequently, the creation (annihilation) operators $c_i^\dagger$ (c_i) are substituted by raising (lowering) spin operator S_i^+ (S_i^-). Although this equivalence works well for one site, one crucial problem arises for a many-site model; while two fermion operators of different sites anticommute, two spin operaters commute. This dilemma was solved by JORDAN and WIGNER [83] by choosing an adequate transformation, which we will show in the following sections.

A.1. Spinless Fermions

This section outlines the JWT for spinless fermions. Our aim is to substitute the fermion operators by spin operators. Exemplarily, we will also investigate, how the Hamilton operator of 1D free spinless fermions

$$H = \sum_{<ij>} c_i^\dagger c_j \ . \tag{A.1}$$

transforms under the JWT.

Let $\vec{S}_i = (S_i^x, S_i^y, S_i^z)$ be a spin-1/2 at site i, with the raising and lowering operators S_i^+, S_i^- defined by

$$S_i^\pm = S_i^x \pm \mathrm{i} S_i^y \tag{A.2}$$

Consider the non-local "kink" operator

$$K_j = \exp\left(\mathrm{i}\pi \sum_{i=1}^{j-1} S_i^+ S_i^-\right) \ . \tag{A.3}$$

We define the operators

$$c_j = K_j S_j^- \quad \text{and} \quad c_j^\dagger = S_j^+ K_j \tag{A.4}$$

which one can show are indeed fermion operators. For a proof, we use that $S_i^\pm$ and K_j anti-commute for $i < j$ and commute otherwise:

$$\{S_i^\pm, K_j\} = 0 \quad \text{for } i < j \qquad \text{and} \qquad [S_i^\pm, K_j] = 0 \quad \text{for } i \geq j \ . \tag{A.5}$$

Thus we observe for $i < j$

$$c_i c_j = K_i S_i^- K_j S_j^- = -K_i K_j S_i^- S_j^- \qquad (A.6)$$
$$= -K_j S_j^- K_i S_i^- = -c_j c_i$$

and similarly one proves for $i \neq j$

$$c_i^\dagger c_j = S_i^+ K_i K_j S_j^- = -K_j S_j^- S_i^+ K_i = -c_j c_i^\dagger \ . \qquad (A.7)$$

In summary, we have shown that c_i obeys the canonical anti-commutation relations

$$\{c_i, c_j\} = \{c_i^\dagger, c_j^\dagger\} = 0 \quad \text{and} \quad \{c_i, c_j^\dagger\} = \delta_{i,j} \qquad (A.8)$$

Thus, $c_i^\dagger$ (c_i) creates (destroys) a fermion at site i.
If we insert the JWT (A.4) into (A.1), one observes

$$c_{i+1}^\dagger c_i = S_{i+1}^+ K_{i+1} K_i S_i^- = S_{i+1}^+ e^{i\pi S_i^+ S_i^-} S_i^- = -2 S_{i+1}^+ S_i^z S_i^- \qquad (A.9)$$

$$= -2 S_{i+1}^+ \left(S_i^+ S_i^- - \frac{1}{2} \right) S_i^- = S_{i+1}^+ S_i^- \qquad (A.10)$$

and similarly

$$c_i^\dagger c_{i+1} = S_i^+ S_{i+1}^- \qquad (A.11)$$

Thus, the Hamiltonian has the same shape in terms of spin operators

$$H = \sum_{<ij>} S_i^+ S_{i+1}^- \ . \qquad (A.12)$$

Note, that in the JWT the boundary conditions may change from periodic to anti-periodic ones, depending on if the number of lattice sites are odd or even.

A.2. Fermions with Spin

If we consider 1D free fermions with spin the JWT has to be generalized:

$$c_{j\sigma} = K_{j\sigma} S_{j\sigma}^-, \quad c_{j\sigma}^\dagger = S_{j\sigma}^+ K_{j\sigma} \qquad (A.13)$$

with the kink operators

$$K_{j\uparrow} = \exp\left(i\pi \sum_{i,\sigma}^{j-1} S_{i\sigma}^+ S_{i\sigma}^- \right) \quad \text{with} \qquad K_{j\downarrow} = \exp\left(i\pi \sum_{i,\sigma}^{j} S_{i\sigma}^+ S_{i\sigma}^- \right) \qquad (A.14)$$

$S_{i\sigma}$ are spin-1/2 operators at site i, where two "types" of spins are distinguished by σ. Note, that here the JWT identifies the basis $|n_\uparrow, n_\downarrow\rangle$ with a spin basis $|S_\uparrow^z, S_\downarrow^z\rangle$. The difference of the operators $K_{j\uparrow}$ and $K_{j\downarrow}$ is, that the summation is taken up to $j-1$ or j, respectively. This is in particular necessary to guarantee, that the fermion operators of the same site j and different spins σ anti-commute. We next show, that this JWT conserves the anti-commuting relations of the fermion operators. For that purpose, we use the relations

$$K_{j\uparrow} S_{l\sigma}^\pm = (-1)^{\delta_{l<j}} S_{l\sigma}^\pm K_{j\uparrow} \quad \text{and} \quad K_{j\downarrow} S_{l\sigma}^\pm = (-1)^{\delta_{l\leq j}} S_{l\sigma}^\pm K_{j\downarrow} \ . \qquad (A.15)$$

A. Jordan-Wigner Transformation

We next show the anti-commutator relation

$$\{c_{j\sigma}, c_{l\tau}\} = 0 \quad \text{and} \quad \{c_{j\sigma}^\dagger, c_{l\tau}\} = \delta_{j,l}\delta_{\sigma,\tau} \ . \tag{A.16}$$

For $j < l$ one observes

$$
\begin{aligned}
c_{j\sigma}^\dagger c_{l\tau} &= S_{j\sigma}^+ K_{j\sigma} K_{l\tau} S_{l\tau}^- = (-1)^{\delta_{\tau,\downarrow}} S_{j\sigma}^+ K_{j\sigma} S_{l\tau}^- K_{l\tau} \\
&= (-1)^{\delta_{\tau,\downarrow}} S_{l\tau}^- S_{j\sigma}^+ K_{l\tau} K_{j\sigma} = -(-1)^{\delta_{\tau,\downarrow}} S_{l\tau}^- K_{l\tau} S_{j\sigma}^+ K_{j\sigma} \\
&= -K_{l\tau} S_{l\tau}^- S_{j\sigma}^+ K_{j\sigma} = -c_{l\tau} c_{j\sigma}^\dagger
\end{aligned}
\tag{A.17}
$$

and

$$
\begin{aligned}
c_{j\sigma} c_{l\tau} &= K_{j\sigma} S_{j\sigma}^- K_{l\tau} S_{l\tau}^- = -K_{j\sigma} K_{l\tau} S_{j\sigma}^- S_{l\tau}^- \\
&= -K_{l\tau} K_{j\sigma} S_{l\tau}^- S_{j\sigma}^- = -K_{l\tau} S_{l\tau}^- K_{j\sigma} S_{j\sigma}^- = -c_{l\tau} c_{j\sigma}
\end{aligned}
\tag{A.18}
$$

For $j = l$ one finds

$$
\begin{aligned}
c_{j\sigma}^\dagger c_{j\tau} &= S_{j\sigma}^+ K_{j\sigma} K_{j\tau} S_{j\tau}^- = (-1)^{\delta_{\sigma\neq\tau}} K_{j\sigma} S_{j\sigma}^+ S_{j\tau}^- K_{j\tau} \\
c_{j\tau} c_{j\sigma}^\dagger &= K_{j\tau} S_{j\tau}^- S_{j\sigma}^+ K_{j\sigma} \ ,
\end{aligned}
\tag{A.19}
$$

For $\sigma \neq \tau$ the operators $S_{j\sigma}^+$ and $S_{j\tau}^-$ commute and hence $\{c_{j\sigma}^\dagger, c_{j\tau}\} = 0$. Otherwise ($\sigma = \tau$) we have $\{S_{j\sigma}^+, S_{j\sigma}^-\} = 1$ and thus $\{c_{j\sigma}^\dagger, c_{j\sigma}\} = 0$. This completes the proof.

In contrast to the free spinless fermion case, the local Hamiltonian of free fermions with spin

$$H = \sum_{<ij>\sigma} c_{i\sigma}^\dagger c_{j\sigma} \ , \tag{A.20}$$

is not "invariant" under the JWT. Inserting (A.13) into (A.20) yields

$$
\begin{aligned}
c_{i+1\uparrow}^\dagger c_{i\uparrow} &= S_{i+1\uparrow} K_{i+1\uparrow} K_{i\uparrow} S_{i\uparrow} = S_{i+1\uparrow} \, e^{i\pi S_{i\uparrow}^+ S_{i\uparrow}^-} \, e^{i\pi S_{i\downarrow}^+ S_{i\downarrow}^-} S_{i\downarrow} \tag{A.21} \\
&= e^{i\pi S_{i\downarrow}^+ S_{i\downarrow}^-} \, S_{i\downarrow} S_{i+1\uparrow} S_{i\uparrow} \quad \text{(cf. (A.9))} \\
&= (-1)^{n_{i\downarrow}} S_{i+1\uparrow} S_{i\uparrow} \ , \tag{A.22}
\end{aligned}
$$

where $n_{i\downarrow} = S_{i\downarrow}^+ S_{i\downarrow}^-$. Similarly one can prove

$$c_{i+1\downarrow}^\dagger c_{i\downarrow} = (-1)^{n_{i+1\uparrow}} S_{i+1\downarrow} S_{i\downarrow} \ . \tag{A.23}$$

Hence, the transformed Hamilton reads

$$H = -\sum_i \left((-1)^{n_{i\downarrow}} S_{i+1\uparrow}^+ S_{i\uparrow}^- + (-1)^{n_{i+1\uparrow}} S_{i+1\downarrow}^+ S_{i\downarrow}^- + \text{h.c.}\right) \tag{A.24}$$

The fermion statistic demands changing signs for the hopping terms in a spin description. Note, that as in the spinless case the boundary conditions may also change.

B. Exact Thermodynamics of the Hirsch model at $X/t = 1$

This section summaries the basic steps of calculating the partition function and grand canonical potential (3.21) of the Hirsch model at $X/t = 1$ ($t = 1$) (see also sec. 3.2.1) in the thermodynamic limit $L \to \infty$. The Hamilton operator $\mathcal{H} = \mathcal{H}_X + \mathcal{H}_U + \mathcal{H}_{\text{ext}}$ we consider is found in (3.10). We use the rearrangement of the FOCK space shown in sec. 2.3.3. The energy levels of eq. 2.57 additionally split up due to $\mathcal{H}_{\text{ext}}$ and explicitly read

$$E(\{n_k^A\}, N_{\uparrow\downarrow}, \tilde{N}_\uparrow) = \sum_k \epsilon_k n_k^A + U N_{\uparrow\downarrow} - hM - \mu N$$

$$\overset{(\star)}{=} \sum_k (\epsilon_k - \mu + h) n_k^A + N_{\uparrow\downarrow}(U - 2\mu) - 2h\tilde{N}_\uparrow \qquad \text{(B.1)}$$

where $\tilde{N}_\uparrow = N_\uparrow - N_{\uparrow\downarrow}$ counts the A species (cf. sec. 2.3.3) with spin up and the momentum k takes values $k = \pi j/(L+1), j = 1 \ldots L$. The identity $(\star)$ can be proved by using

$$N = N_A + 2N_{\uparrow\downarrow} = N \;, \qquad \text{(B.2)}$$
$$M = 2\tilde{N}_\uparrow - N_A \quad \text{and} \qquad \text{(B.3)}$$
$$N_A = \sum_k n_k^A \;. \qquad \text{(B.4)}$$

The degeneracy g of each energy level is found by combinatorial arguments. For each sequence $\{n_k^A\}$ there are $\binom{N_A}{\tilde{N}_\uparrow}$ configurations of $\tilde{N}_\uparrow$ A-species of type $|\uparrow\rangle$. Analogously, $\binom{L-N_A}{N_{\uparrow\downarrow}}$ configurations of $N_{\uparrow\downarrow}$ doubly occupied sites $|\uparrow\downarrow\rangle$ are possible, thus

$$g(\{n_k^A\}, N_{\uparrow\downarrow}, \tilde{N}_\uparrow) = \binom{N_A}{\tilde{N}_\uparrow}\binom{L - N_A}{N_{\uparrow\downarrow}} \qquad \text{(B.5)}$$

Note, that the latter equation is consistent with eq. (2.58) by summing out $\tilde{N}_\uparrow$.

B. Exact Thermodynamics of the Hirsch model at $X/t = 1$

For the partition function of a finite system of length L we find

$$
\begin{aligned}
Z_L &= \sum_{\{n_k^A\}} \sum_{N_{\uparrow\downarrow}=0}^{L-N_A} \sum_{\tilde{N}_\uparrow=0}^{N_A} \binom{N_A}{\tilde{N}_\uparrow} \binom{L-N_A}{N_{\uparrow\downarrow}} e^{-\beta\left(\sum_k (\epsilon_k-\mu+h)n_k^A + N_{\uparrow\downarrow}(U-2\mu)-2h\tilde{N}_\uparrow\right)} \\
&= \sum_{\{n_k^A\}} \left(\sum_{N_{\uparrow\downarrow}=0}^{L-N_A} \binom{L-N_A}{N_{\uparrow\downarrow}} e^{-\beta(U-2\mu)N_{\uparrow\downarrow}} \right) \left(\sum_{\tilde{N}_\uparrow=0}^{N_A} \binom{N_A}{\tilde{N}_\uparrow} e^{2\beta h \tilde{N}_\uparrow} \right) \\
&\quad \times \prod_k e^{-\beta(\epsilon_k-\mu+h)n_k^A} \\
&= \sum_{\{n_k^A\}} \left(1+e^{-\beta(U-2\mu)}\right)^{L-N_A} \left(1+e^{2\beta h}\right)^{N_A} \prod_k e^{-\beta(\epsilon_k-\mu+h)n_k^A} \\
&= \left(1+e^{\beta(2\mu-U)}\right)^L \prod_k \sum_{n^A=0}^1 \left(\frac{1+e^{2\beta h}}{1+e^{-\beta(U-2\mu)}} e^{-\beta(\epsilon_k-\mu+h)} \right)^{n^A} \\
&= \left(1+e^{\beta(2\mu-U)}\right)^L \prod_k \left(1+ \frac{2\cosh(\beta h)}{1+e^{-\beta(U-2\mu)}} e^{-\beta(\epsilon_k-\mu)} \right) \\
&= \left(1+e^{\beta(2\mu-U)}\right)^L \prod_k \left(1+e^{-\beta(\epsilon_k-\mu^*)}\right) \tag{B.6}
\end{aligned}
$$

where

$$
\mu^*(\mu,\beta,U,h) = \mu + \frac{1}{\beta} \ln \frac{2\cosh(\beta h)}{1+e^{\beta(2\mu-U)}} . \tag{B.7}
$$

is an effective chemical potential. Thus, the grand canonical potential φ reads

$$
-\beta\varphi = \frac{1}{L} \ln Z_L = \ln\left(1+e^{\beta(2\mu-U)}\right) + \frac{1}{L} \sum_k \ln\left(1+e^{-\beta(\epsilon_k-\mu^*)}\right)
$$

$$
\xrightarrow{L\to\infty} \ \ln\left(1+e^{\beta(2\mu-U)}\right) + \frac{1}{\pi} \int_0^\pi dk \, \ln\left(1+e^{-\beta(\epsilon_k-\mu^*)}\right) \tag{B.8}
$$

The result coincides with [76]. The integral is not trivially solvable. But nevertheless precise numerical analysis is possible, so that various thermodynamic properties are accessible.

C. Correlation Lengths of Free Fermions with Spin

In section 3.3.2 we referred to exact results for the correlation lengths of free fermions with spin. We derive the formula for the correlation length

$$\xi^{-1} = 2\mathrm{arsinh}(\pi T/2) \ , \tag{C.1}$$

which is valid for all spin, density, triplet and singlet pair correlations.
We start with the free fermion Hamiltonian

$$H = -t \sum_{j\sigma} \left(c^\dagger_{j,\sigma} c_{j+1,\sigma} + c^\dagger_{j+1,\sigma} c_{j,\sigma} \right) \ . \tag{C.2}$$

H is diagonal in momentum space

$$H = -2t \sum_{q\sigma} \cos q \, c^\dagger_{q\sigma} c_{q\sigma} = \sum_{q\sigma} \epsilon_q n_{q\sigma} \tag{C.3}$$

where $\epsilon_q = -2t \cos q$, $n_{q\sigma} = c^\dagger_{q\sigma} c_{q\sigma}$ and $c_{q\sigma}$ is given by the Fourier transformation

$$c^{(\dagger)}_{j\sigma} = \sum_q \mathrm{e}^{iqj} c^{(\dagger)}_{q\sigma} \ . \tag{C.4}$$

We consider the the density correlation function at finite temperature $T > 0$

$$\langle n_r n_0 \rangle = \sum_{\sigma,\sigma'} \langle c^\dagger_{r\sigma} c_{r\sigma} c^\dagger_{0\sigma'} c_{0\sigma'} \rangle \ . \tag{C.5}$$

Following WICK'S theorem the density correlation separates into

$$\langle n_r n_0 \rangle = \sum_{\sigma\sigma'} \left(\langle n_{r\sigma} \rangle \langle n_{0\sigma'} \rangle - \langle c^\dagger_{r\sigma} c_{0\sigma'} \rangle \langle c^\dagger_{0\sigma'} c_{r\sigma} \rangle \right) = n^2 - 2f^2(r) \tag{C.6}$$

where

$$f(r) = \langle c^\dagger_{r\sigma} c_{0\sigma} \rangle = \sum_{q,q'} \mathrm{e}^{-iqr} \underbrace{\langle c^\dagger_{q\sigma} c_{q'\sigma} \rangle}_{n_{q\sigma}\delta_{q,q'}} = \sum_q \frac{\mathrm{e}^{-iqr}}{\mathrm{e}^{\beta\epsilon_q} + 1} \tag{C.7}$$

$$\to \frac{1}{2\pi} \int_{-\pi}^{\pi} \mathrm{d}q \, \underbrace{\frac{\mathrm{e}^{-iqr}}{\mathrm{e}^{2\beta\cos q} + 1}}_{=:g(q)} \quad \text{for the thermodynamic limit .} \tag{C.8}$$
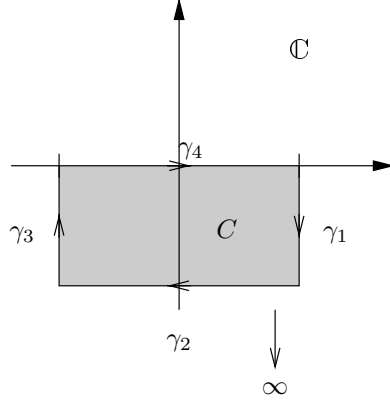
Figure C.1.: Integral path $\partial C = \gamma = \bigcup_i \gamma_i$. The path γ_2 is shifted to infinity, such that this part of the integral does not contribute. The integrals along γ_1 and γ_3 cancel each other. Therefore the integrals over γ and $[-\pi, \pi]$ are equal.

We solve the integral by residuum calculus

$$f(r) = \frac{1}{2\pi} \int_{-\pi}^{\pi} \mathrm{d}q\, g(q) = \frac{1}{2\pi} \oint_\gamma \mathrm{d}z\, g(z) = -\mathrm{i} \sum_{z_i} \mathrm{res}_{z_i} g \qquad (C.9)$$

The integration path $\gamma = \partial C$, which border the complex area $C \in \mathbb{C}$, is shown in fig. C.1. The poles of g are

$$z_{k,n} = (2k+1)\frac{\pi}{2} + \mathrm{i}(-1)^k \mathrm{arsinh}(\alpha_n), \quad \text{with } \alpha_n = \frac{(2n+1)\pi}{2\beta} \quad \text{and } k,n \in \mathbb{Z}\ . \tag{C.10}$$

Singularities with $(k,n) \in (-1, \mathbb{N}_0) \cup (1, -\mathbb{N})$ fall into the area C and contribute to eq. (C.9). The residuum of g explicitly reads

$$\mathrm{res}_{z_{k,n}} g = -\frac{\mathrm{e}^{-\mathrm{i}z_{k,n}r}}{2\beta \sin z_{k,n}} = \frac{\mathrm{e}^{-r\,\mathrm{arsinh}(\alpha_n)}}{\sqrt{4\beta^2 + (2n+1)^2\pi^2}} \cdot \mathrm{e}^{\pm\mathrm{i}\frac{\pi}{2}r}\ . \tag{C.11}$$

The dominant part of (C.11) (i.e. $r \gg 1$) is obviously given by the residuum of $z_{-1,0}$ and $z_{0,-1}$, which yields

$$f(r) \sim -\mathrm{i}\left(\mathrm{res}_{z_{-1,0}} g + \mathrm{res}_{z_{0,-1}} g\right) = \frac{2\sin\left(\frac{\pi}{2}r\right)}{4\beta^2 + \pi^2} \cdot \mathrm{e}^{-r\,\mathrm{arsinh}(\frac{\pi}{2\beta})} \tag{C.12}$$

Therefore the asymptotics of the density-density correlation function reads

$$\langle n_r n_0 \rangle \sim f^2(r) \sim \mathrm{e}^{-r/\xi} \tag{C.13}$$

with the thermal correlation length

$$\xi^{-1} = 2\,\mathrm{arsinh}\left(\frac{\pi}{2\beta}\right)\ . \tag{C.14}$$

All other correlation function, such as spin-spin, singlet pair or triplet pair correlations have the same correlation length due to WICK'S theorem. As an example we consider the singlet-pair correlation $\left\langle P_s^\dagger(r)P_s(0)\right\rangle$ and deduce

$$
\begin{aligned}
2\left\langle P_s^\dagger(r)P_s(0)\right\rangle &= \left\langle (c_{r+1,\uparrow}^\dagger c_{r,\downarrow}^\dagger - c_{r+1,\downarrow}^\dagger c_{r,\uparrow}^\dagger)\cdot(c_{1,\uparrow}c_{0,\downarrow} - c_{1,\downarrow}c_{0,\uparrow})\right\rangle \\
&= \left\langle c_{r+1,\uparrow}^\dagger c_{r,\downarrow}^\dagger c_{1,\uparrow}c_{0,\downarrow}\right\rangle - \left\langle c_{r+1,\uparrow}^\dagger c_{r,\downarrow}^\dagger c_{1,\downarrow}c_{0,\uparrow}\right\rangle - \\
&\quad \left\langle c_{r+1,\downarrow}^\dagger c_{r,\uparrow}^\dagger c_{1,\uparrow}c_{0,\downarrow}\right\rangle + \left\langle c_{r+1,\downarrow}^\dagger c_{r,\uparrow}^\dagger c_{1,\downarrow}c_{0,\uparrow}\right\rangle \\
&= -\left\langle c_{r+1,\uparrow}^\dagger c_{r,\uparrow}\right\rangle\left\langle c_{1,\downarrow}^\dagger c_{0,\downarrow}\right\rangle - \left\langle c_{r+1,\uparrow}^\dagger c_{0,\uparrow}\right\rangle\left\langle c_{r,\downarrow}^\dagger c_{1,\downarrow}\right\rangle \\
&\quad -\left\langle c_{r+1,\downarrow}^\dagger c_{0,\downarrow}\right\rangle\left\langle c_{r,\uparrow}^\dagger c_{1,\uparrow}\right\rangle - \left\langle c_{r+1,\downarrow}^\dagger c_{1,\downarrow}\right\rangle\left\langle c_{r,\uparrow}^\dagger c_{0,\uparrow}\right\rangle \\
&= -f^2(r) - f(r+1)f(r-1) \sim f^2(r)\ . \qquad \text{(C.15)}
\end{aligned}
$$

Analogous one obtains

$$
\begin{aligned}
\left\langle S_r^z S_0^z\right\rangle &= \frac{S_z^2}{4} - \frac{1}{2}f^2(r) \sim f^2(r) \quad \text{and} \\
\left\langle P_t^\dagger(r)P_t(0)\right\rangle &= f^2(r) - f(r+1)f(r-1) \sim f^2(r)\ . \qquad \text{(C.16)}
\end{aligned}
$$

Hence we have proved, that the thermal correlation lengths of all correlation functions, that we consider in this thesis, have the same correlation length (C.14).

Bibliography

[1] S. R. White, Phys. Rev. Lett. **69**, 2863 (1992).

[2] S. R. White, Phys. Rev. B **48**, 10345 (1993).

[3] T. Nishino, J. Phys. Soc. Jpn. **64**, 3598 (1995).

[4] M. Suzuki, Comunn. Math. Phys. **51**, 183 (1976).

[5] H. Trotter, Proc. Amer. Math. Soc. **10**, 545 (1959).

[6] R. J. Bursill, T. Xiang, and G. A. Gehring, J. Phys.: Cond. Mat. **8**, L583 (1996).

[7] X. Wang and T. Xiang, Phys. Rev. B **56**, 5061 (1997).

[8] J. G. Bednorz and K. A. Müller, Z. Phys. B **64**, 189 (1986).

[9] M. C. Gutzwiller, Phys. Rev. Lett. **10**, 159 (1963).

[10] J. Hubbard, Proc. Roy. Soc. A **276**, 238 (1963).

[11] J. Kanamori, Prog. Theor. Phys **30**, 275 (1963).

[12] D. K. Campbell, J. T. Gammel, and E. Y. L. Jr., Phys. Rev. B **42**, 475 (1990).

[13] A. A. Aligia and E. Gagliano, Phys. Rev. B **60**, 15332 (1999).

[14] J. E. Hirsch, Phys. Lett. A **134**, 452 (1989).

[15] J. E. Hirsch, Physica C **158**, 326 (1989).

[16] J. E. Hirsch and F. Marsiglio, Phys. Rev. B **39**, 11515 (1989).

[17] J. E. Hirsch and F. Marsiglio, Physica C **162-164**, 591 (1989).

[18] F. Marsiglio and J. E. Hirsch, Phys. Rev. B **41**, 6435 (1990).

[19] N. G. van Kampen, *Stochastic processes in physics and chemistry*, North Holland, 1981.

[20] M. Schreckenberg, A. Schadscheider, K. Nagel, and M. Ito, Phys. Rev. E **51**, 2939 (1995).

[21] S. Alexander and T. Holstein, Phys. Rev. B **18**, 301 (1978).

[22] T. Nishino and K. Okunishi, J. Phys. Soc. Jpn. **65**, 891 (1996).

[23] T. Nishino and K. Okunishi, J. Phys. Soc. Jpn. **66**, 3040 (1997).

[24] J. Sirker and A. Klümper, Europhys. Lett. **60**, 262 (2002).

[25] J. Sirker, *Transfer matrix approach to thermodynamics and dynamics of one-dimensional quantum systems*, PhD thesis, University of Dortmund (Germany), 2002.

[26] I. Peschel, X. Wang, M. Kaulke, and K. Hallberg, editors, *Density-Matrix Renormalisation*, volume 528 of *Lecture Notes in Physics*, Springer, 1998.

[27] K. G. Wilson, Phys. Rev. B **4**, 3174 (1971).

[28] K. G. Wilson, Rev. Mod. Phys. **47**, 773 (1975).

[29] J. W. Bray and S. T. Chui, Phys. Rev. B **19**, 4876 (1979).

[30] T. Xiang and G. Gehring, Phys. Rev. B **48**, 303 (1993).

[31] A. Kemper, *Transfermatrix-Dichtematrix-Renormierungsgruppe für zwei-dimensionale klassische Modelle der statistischen Mechanik*, Diplomarbeit, University of Cologne, 2000.

[32] F. Zhang, *Matrix Theory, Basic Results and Techniques*, Springer, 1999.

[33] I. Peschel, M. Kaulke, and O. Legeza, Ann. Physik (Lpz.) **8**, 153 (1999).

[34] R. Noack and S. White, in *Density Matrix Renormalisation Group*, edited by I. Peschel et al., volume 528 of *Lecture Notes in Physics*, Springer, 1998.

[35] E. Davidson, J. Comput. Phys. **17**, 87 (1975).

[36] C. Lanczos, J. Res. Natl. Nur. Stand. **45**, 225 (1950).

[37] M. Suzuki, Phys. Rev. B **31**, 2957 (1985).

[38] G. Jüttner, A. Klümper, and J. Suzuki, Nuc. Phys. B **487**, 650 (1997).

[39] G. Jüttner, A. Klümper, and J. Suzuki, J. Phys. A **30**, 1181 (1997).

[40] W. E. Arnoldi, Quart. Appl. Math. **9**, 17 (1951).

[41] ARPACK software availiable at `ftp.caam.rice.edu`.

[42] E. Anderson et al., *LAPACK Users' Guide*, SIAM, 1995.

[43] J. Sirker, private communications.

[44] F. Bloch, Herv. Phys. Acta **7**, 385 (1934).

[45] L. D. Landau, Sov. Phys. JETP **3**, 920 (1957).

[46] L. D. Landau, Sov. Phys. JETP **5**, 101 (1957).

[47] L. D. Landau, Sov. Phys. JETP **8**, 70 (1958).

[48] J. R. Schrieffer, *Theory of Superconductivity*, Frontiers in Physics, Addison-Wesley, 1988.

[49] E. H. Lieb and F. Wu, Phys. Rev. Lett. **20**, 1445 (1968).

[50] A. Ovchinnikov, Soviet Phys. JETP **30**, 1160 (1970).

[51] C. Coll, Phys. Rev. B **9**, 2150 (1974).

[52] F. Woynarovich, J. Phys. A **15**, 2985 (1982).

[53] A. Klümper, A. Schadschneider, and J. Zittartz, Z. Phys. B **78**, 99 (1990).

[54] H. Shiba, Phys. Rev. B **6**, 930 (1972).

[55] M. Ogata and H. Shiba, Phys. Rev. B **41**, 2326 (1990).

[56] C. Yang, Phys. Rev. Lett. **63**, 2144 (1989).

[57] F. Essler, V. Korepin, and K. Schoutens, Phys. Rev. Lett. **67**, 3848 (1991).

[58] S. Murakami and F. Göhmann, Phys. Lett. A **227**, 216 (1997).

[59] A. Klümper and R. Z. Bariev, Nuc. Phys. B **458**, 523 (1996).

[60] H. J. Schulz, G. Cuniberti, and P. Pieri, in *Field Theories of Low-Dimensional Condensed Matter Systems*, edited by G. Morandi et al., volume 131 of *Spinger Series in Solid-State Sciences*, Springer, 2000.

[61] F. D. M. Haldane, J. Phys. C: Sol. Stat. Phys. **12**, 4791 (1979).

[62] F. D. M. Haldane, Phys. Rev. Lett. **45**, 1358 (1980).

[63] F. D. M. Haldane, Phys. Lett. **81A**, 153 (1981).

[64] S. Tomonaga, Prog. Theor. Phys. **5**, 4544 (1950).

[65] J. M. Luttinger, J. Math. Phys. **4**, 1154 (1963).

[66] A. Luther and V. J. Emery, Phys. Rev. Lett. **33**, 589 (1974).

[67] H. Shiba and M. Ogata, Prog. Theor. Phys. Suppl. **108**, 265 (1992).

[68] F. Marsiglio and J. E. Hirsch, Physica C **171**, 554 (1990).

[69] G. Japaridze and E. Müller-Hartmann, Ann. Physik **3**, 168 (1994).

[70] N. Kawakami and S.-K. Yang, Phys. Rev. B **44**, 7844 (1991).

[71] H. Frahm and V. E. Korepin, Phys. Rev. B **42**, 10553 (1990).

[72] J. de Boer and A. Schadschneider, Phys. Rev. Lett. **75**, 4298 (1995).

[73] J. de Boer, V. E. Korepin, and A. Schadschneider, Phys. Rev. Lett. **74**, 789 (1995).

[74] A. Schadschneider, Phys. Rev. B **51**, 10386 (1995).

[75] L. Arrachea and A. A. Aligia, Phys. Rev. Lett. **73**, 2240 (1994).

[76] F. Dolcini and A. Montorsi, Phys. Rev. B **66**, 075112 (2002).

[77] F. Dolcini and A. Montorsi, Phys. Rev. B **63**, 121103 (2001).

[78] F. Dolcini and A. Montorsi, Phys. Rev. B **65**, 155105 (2002).

[79] M. Quaisser, *Untersuchungen zu Fermionenmodellen mit korreliertem Hüpfen in niedrigen Dimensionen*, PhD thesis, University of Cologne, 1995.

[80] M. Quaisser, A. Schadschneider, and J. Zittartz, Europhys. Lett. **32**, 179 (1995).

[81] L. Arrachea, A. A. Aligia, E. Galgliano, K. Hallberg, and C.Balseiro, Phys. Rev. B **50**, 16044 (1994).

[82] C. Dziurzik, *On the numerical investigation of generalized Hubbard models*, PhD thesis, University of Cologne, to be published.

[83] P. Jordan and E. Wigner, Z. Phys. **47**, 631 (1928).

[84] J. Cardy, in *Phase Transitions and Critical Phenomena*, edited by C. Domb and J. L. Lebowitz, volume 11, Academic Press, 1987.

[85] J. Cardy, *Scaling and Renormalization in Statistical Physics*, Cambridge Lecture Notes in Physics, Cambridge University Press, 1996.

[86] I. Affleck, Phys. Rev. Lett. **56**, 746 (1986).

[87] H. W. J. Blöte, J. L. Cardy, and M. P. Nightingale, Phys. Rev. Lett. **56**, 742 (1986).

[88] F. D. M. Haldane, Phys. Rev. Lett. **47**, 1840 (1981).

[89] H. Shiba, Phys. Rev. B **6**, 930 (1972).

[90] H. J. Schulz, Phys. Rev. Lett. **64**, 2831 (1990).

[91] A. A. Belavin, A. M. Polyakov, and A. B. Zamolodchikov, Nucl. Phys. B **241**, 333 (1984).

[92] N. M. Bogoliubov, A. G. Izergin, and N. Y. Reshetikhin, J. Phys. A **20**, 5361 (1987).

[93] R. Z. Bariev, A. Klümper, A. Schadschneider, and J. Zittartz, J. Phys. A **26**, 1249 (1993).

[94] J. Sirker and A. Klümper, Phys. Rev. B **66**, 245102 (2002).

[95] A. L. Barabási and H. Stanley, *Fractal concepts in surface growth*, Cambridge University Press, 1995.

[96] E. V. Albano, J. Phys. A **27**, L881 (1994).

[97] D. Mollison, J. Roy. Stat. Soc. B **39**, 283 (1977).

[98] P. Bak, C. Tang, and K. Wiesenfeld, Phys. Rev. Lett. **59**, 381 (1987).

[99] L. P. Kadanoff and J. Swift, Phys. Rev. **165**, 310 (1968).

[100] F. C. Alcaraz, M. Droz, M. Henkel, and V. Rittenberg, Ann. Phys. (NY) **230**, 250 (1994).

[101] G. Schütz, in *Phase Transitions and Critical Phenomena*, edited by C. Domb and J. Lebowitz, volume 19, Academic Press, 2000.

[102] B. Derrida and M. Evans, in *Nonequilibrium statistical mechanics in one dimension*, edited by C. Domb and J. L. Lebowitz, Cambridge University Press, 1997.

[103] W. Kinzel, *Percolation structures and processes*, volume 5 of *Ann. Isr. Phys. Soc.*, Adam Hilger, 1983.

[104] W. Kinzel, Z. Phys. B **58**, 229 (1985).

[105] H. Hinrichsen, Adv. Phys. **49**, 815 (2000).

[106] H. Hinrichsen, A. Jimeńez-Dalmaroni, Y. Rozov, and E. Domany, Phys. Rev. Lett. **83**, 4999 (1999).

[107] E. Carlon, M. Henkel, and U. Schollwöck, Eur. Phys. J. B **12**, 99 (1999).

[108] S. K. Scott, *Oscillations, waves, and chaos in chemical kinetics*, Oxford University Press, 1994.

[109] N. Rajewsky, L. Santen, A. Schadschneider, and M. Schreckenberg, Stat. Phys. **92**, 151 (1998).

[110] I. Jensen and R. Dickman, J. Stat. Phys **71**, 89 (1993).

[111] J. Cardy and U. C. Täubner, Phys. Rev. Lett. **77**, 4870 (1996).

[112] H. K. Janssen, Z. Phys B **42**, 151 (1981).

[113] P. Grassberger, Z. Phys. B **47**, 365 (1982).

[114] E. Carlon, M. Henkel, and U. Schollwöck, Phys. Rev. E **63**, 036101 (2001).

[115] H. Hinrichsen, Phys. Rev. E **63**, 036102 (2001).

[116] G. Ódor, Phys. Rev. E **62**, R3027 (2000).

[117] H. Hinrichsen, K. Krebs, and I. Peschel, Z. Phys. B **100**, 105 (1996).

[118] R. Kroon, H. Fleurent, and R. Sprik, Phys. Rev. E **47**, 2462 (1993).

[119] M. A. Munoz, R. Dickman, A. Vespignani, and S. Zapperi, Phys. Rev. E **59**, 6175 (1999).

[120] J. W. Essam, I. J. A. J. Guttmann, and D. Tanlakishani, J. Phys. A **29**, 1619 (1996).

[121] A. Kemper, A. Schadschneider, and J. Zittartz, J. Phys. A: Math. Gen. **34**, L279 (2001).

[122] T. Enss and U. Schollwöck, J. Phys. A: Math. Gen. **34**, 7769 (2001).

[123] T. Enss, *Transfermatrixrenormierung fern vom statistischen Gleichgewicht*, Diplomarbeit, University of Munich, 2002.

[124] A. Kemper, A. Gendiar, T. Nishino, A. Schadschneider, and J. Zittartz, J. Phys. A: Math. Gen. **36**, 29 (2003).

[125] R. J. Baxter, *Exactly Solved Models in Statistical Mechanics*, Academic Press, 1982.

[126] A. Gendiar and T. Nishino, Phys. Rev. E **65**, 046702 (2002).

[127] T. Nishino and K. Okunishi, J. Phys. Soc. Jpn **67**, 1492 (1998).

[128] T. Nishino and K. Okunishi, J. Phys. Soc. Jpn. **67**, 3066 (1998).

[129] GNU multiprecision library (GMP) available from `www.gnu.org`.

Danksagungen

English Abstract

The present work applies a numerical method, namely the transfer-matrix density-matrix renormalization group (TMRG), to two seemingly different types of models. In a first part (chapter 1–3) the TMRG is used to investigate the thermodynamics of one-dimensional fermionic models. A second part (chapter 4–6) deals with a novel TMRG method for one-dimensional stochastic models, whose development is an integral part of the thesis. First, the "traditional" TMRG algorithm for quantum systems is outlined in its historical context. Two different variants are presented, following works of Xiang et al. and Sirker and Klümper, respectively. The basic idea of the method is to map the thermodynamics of a one-dimensional quantum model by Trotter-Suzuki decomposition onto a two-dimensional statistical one. The latter is then solved by a transfer-matrix approach combined with the iterative numerical procedure of White's density-matrix renormalization-group (DMRG) algorithm. Thereby precise computations of various thermodynamic properties, such as thermodynamic potentials, susceptibilities, thermal expectation values and correlation functions are possible. As the first part of the thesis deals with fermionic models, we next review some basics about the theory of strongly correlated fermions in one dimension. Thereupon we elucidate the so-called Hirsch model, which recently gained a lot of theoretic interest in respect to high-temperature superconductivity. It extends the well-studied Hubbard model by an off-diagonal bond-charge interaction term. The current state of research is briefly summarized and mainly refers to ground state properties. Showing numerical TMRG results we then investigate and discuss the almost unknown thermodynamics of the Hirsch model. Various phases are identified and characterized in terms of Tomonaga-Luttinger and Luther-Emery liquid properties, in accordance with previous studies of the ground state. As an important result, superconducting singlet-pair correlation lenths are observed to dominate the physics at finite temperatures in a certain spin-gaped phase. Subsequent to our thermodynamic studies, we turn to the second part of the thesis and outline some theoretic basics of stochastic models. Most notably is the important formal analogy of the master equation, that describes the dynamics of the model, to a Schrödinger equation in imaginary time. This analogy is used to construct a "stochastic TMRG" algorithm almost similar to the quantum case, that facilitates the computation of dynamic properties, e.g. the local density of particles. We intensively focus on interesting mathematical properties of the stochastic transfer-matrix. As an astonishing result it is found, that the temporal evolution of the non-equilibrium process is reflected by a certain causal structure of the stochastic TMRG. But even if this new approach seems to be promising at first glance, severe numerical problems limit significantly its practical use. In order to solve these instabilities we propose a completely new variant of the algorithm, which we call stochastic light-cone corner-transfermatrix DMRG (LCTMRG). As suggested by its name, the LCTMRG makes use of the causal structure mentioned above and combines it with the stochastic TMRG algorithm. Applications of the LCTMRG onto various reaction-diffusion models verify highly precise numerical data and a great improve compared to the "old" algorithm by several orders of magnitude. Additionally it is stressed, that the newly proposed analysis tool provides some considerable advantages to common simulation techniques.

Deutsche Kurzzusammenfassung

Die vorliegende Arbeit befasst sich mit der Anwendung einer numerischen Methode, der Transfermatrix-Dichtematrix Renormierungsgruppe, auf zwei auf den ersten Blick unterschiedliche Modellklassen. In einem ersten Teil (Kapitel 1–3) wird die TMRG zur Untersuchung der Thermodynamik eindimensionaler Fermionmodelle genutzt. Ein zweiter Teil (Kapitel 4–6) befasst sich mit einer neuartigen TMRG Methode für eindimensionale stochastische Modelle, deren Entwicklung integraler Bestandteil dieser Arbeit ist. Zunächst wird der „traditionelle" TMRG Algorithmus in historischem Kontext skizziert. Zwei verschiedene Varianten werden vorgestellt, anknüpfend an die Arbeiten von Xiang et al. bzw. Sirker und Klümper. Grundlegende Idee der Methode ist, die Thermodynamik eines eindimensionalen Quantensystems durch Trotter-Suzuki Zerlegung auf ein zweidimensionales statistisches Modell abzubilden. Letzteres wird dann anhand eines Transfermatrix-Zugangs in Kombination mit dem iterativen Verfahren der White'schen Dichtematrix-Renormierungsgruppe (DMRG) numerisch gelöst. So sind hoch genaue Berechnungen verschiedener thermodynamischer Eigenschaften möglich, wie z.B. thermodynamische Potentiale, Suszeptibilitäten, thermische Erwartungswerte und Korrelationsfunktionen. Da sich der erste Teil der Arbeit mit Fermionensystemen befasst, werden zunächst einige Grundlagen zur Theorie stark korrelierter Fermionen in einer Dimension zusammengefasst. Daraufhin erläutern wir das sogenannte Hirsch-Modell, welches gerade in letzter Zeit in Hinblick auf Hochtemperatur-Supraleitung großes theoretisches Interesse erlangt hat. Es erweitert das vielseits bekannte Hubbard-Modell um einen nicht-diagonalen bond-charge Wechselwirkungsterm. Der aktuelle Stand der Forschung ist kurz zusammengefasst und beschränkt sich im wesentlichen auf Grundzustandseigenschaften. Anhand numerischer TMRG Ergebnisse untersuchen und diskutieren wir daraufhin die weitgehend unbekannte Thermodynamik des Hirsch-Modells. Verschiedene Phasen konnten identifiziert und durch Tomonaga-Luttinger und Luther-Emery Flüssigkeitstheorie charakterisiert werden, in Übereinstimmung mit früheren Arbeiten zum Grundzustand. Als ein wichtiges Ergebnis beobachten wir die Dominanz supraleitender Singlett-Paarkorrelationslängen in einer Phase mit Spin-Anregungslücke. Im Anschluss an die thermodynamischen Studien wenden wir uns dem zweiten Teil dieser Arbeit zu und geben einen Überblick über einige theoretischen Grundlagen stochastischer Modelle. Zu nennen ist vor allem die wichtige formale Analogie der Mastergleichung, die die dynamische Entwicklung des Modells beschreibt, zu einer Schrödinger-Gleichung in imaginärer Zeit. Diese Analogie wird genutzt um einen „stochastischen TMRG" Algorithmus ähnlich zu dem für Quantensysteme zu konstruieren, der die Berechnung dynamischer Eigenschaften erlaubt, wie z.B. der lokalen Teilchendichte. Wir beleuchten detailliert die interessante mathematische Struktur der stochastischen Transfermatrix. Als erstaunliches Ergebnis stellt sich heraus, dass sich die zeitabhängige Natur des Nichtgleichgewicht-Prozesses in einer gewissen kausalen Struktur der stochastischen TMRG äußert. Aber obwohl dieser neue Zugang auf den ersten Blick vielversprechend erscheint, schränken schwerwiegende numerische Probleme dessen praktische Nutzbarkeit erheblich ein. Um diese Instabilitäten zu lösen, schlagen wir eine völlig neue Variante des Algorithmus vor, die wir stochastische Lichtkegel CTMRG nennen (LCTMRG). Wie bereits aus der Bezeichnung ersichtlich ist, nutzt die LCTMRG die oben genannte kausale Struktur und kombiniert sie mit dem stochastischen TMRG Algorithmus. Anwendungen der LCTMRG auf verschiedene Reaktions-Diffusions-Prozesse bestätigen hoch präzise numerische Ergebnisse und eine entscheidene Verbesserung des „alten" Algorithmus. Darüber hinaus wird betont, dass die neu vorgeschlagene Analysemethode einige bedeutende Vorteile gegenüber üblichen Simulationsverfahren bietet.

Erklärung

Ich versichere, dass ich die von mir vorgelegte Dissertation selbständig angefertigt, die benutzten Quellen und Hilfsmittel vollständig angegeben und die Stellen der Arbeit – einschließlich Tabellen, Karten und Abbildungen –, die anderen Werken im Wortlaut oder Sinn nach entnommen sind, in jedem Einzelfall als Entlehnung kenntlich gemacht habe; dass diese Dissertation noch keiner anderen Fakultät oder Universität zur Prüfung vorgelegen hat; dass sie – abgesehen von unten angegebenen Teilpublikationen – noch nicht veröffentlicht worden ist, dass ich eine solche Veröffentlichung vor Abschluss des Promotionsverfahrens nicht vornehmen werde. Die Bestimmungen dieser Promotionsordnung sind mir bekannt. Die von mir vorgelegte Dissertation ist von Herrn Prof. Dr. Johannes Zittartz betreut worden.

Teilpublikationen

1. A. Kemper, A. Schadschneider and J. Zittartz, *Transfer-matrix density-matrix renormalisation group for stochastic models: the Domany-Kinzel cellular automaton*, J. Phys. A: Math. Gen. **34**, L279-287 (2001)

2. A. Kemper, A. Gendiar, T. Nishino, A. Schadschneider and J. Zittartz, *Stochastic light-cone CTMRG: a new DMRG approach to stochastic models*, J. Phys. A: Math. Gen. **36**, 29-41 (2003)

3. A. Kemper and A. Schadschneider, *Thermodynamic properties and thermal correlation lengths of an extended Hubbard model with bond-charge interaction*, zur Veröffentlichung akzeptiert bei Phys. Rev. B (2003)

Lebenslauf

Persönliche Daten

Name:	Andreas Kemper
Geburtsdatum/-ort:	11.05.1974 in Neuss
Familienstand:	ledig
Staatsangehörigkeit:	deutsch

Schulbildung

1980 – 1984	kath. Grundschule Pesch
1984 – 1993	Gymnasium Korschenbroich
06/1993	Abitur

Hochschulstudium

10/1993 – 9/1995	Studium der Wirtschaftsinformatik (TU Darmstadt) mit Vordiplom in Wirtschaftsinformatik
10/1995 – 8/1999	Studium der Physik und Mathematik (Universität Köln) mit Zwischenprüfungen in Mathematik und Physik sowie Vordiplom in Physik
11/2000	Physik-Diplom
seit 1/2001	Promotion am Institut für Theoretische Physik der Universität Köln (Lehrstuhl Prof. Dr. J. Zittartz)

Wissenschaftliche Anstellungen

05/1995 – 08/1995	Studentische Hilfskraft bei der Rechnerbetriebsgruppe (RGB) der TU Darmstadt
10/1997 – 12/2000	Studentische Hilfskraft am Mathematischen Institut bzw. Institut für Theoretische Physik der Universität Köln
01/2001 – 05/2001	Wissenschaftliche Hilfskraft am Institut für Theoretische Physik der Universität Köln
seit 06/2001	Wissenschaftlicher Mitarbeiter am Institut für Theoretische Physik der Universität Köln